

DISSERTATION IN ASTRONOMY

SUBMITTED TO THE
COMBINED FACULTIES OF THE NATURAL SCIENCES AND MATHEMATICS
OF THE RUPERTO-CAROLA-UNIVERSITY OF HEIDELBERG, GERMANY,
FOR THE DEGREE OF
DOCTOR OF NATURAL SCIENCES

PRESENTED BY

M.Sc. MARIA JULIA KAPALA
BORN IN ŁÓDŹ, POLAND

ORAL EXAMINATION: JULY 9TH, 2015

A HERSCHEL SPACE OBSERVATORY
VIEW OF THE ANDROMEDA GALAXY

REFEREES: PROF. DR. HANS-WALTER RIX
DR. SIMON GLOVER

ABSTRACT

In this thesis we study the energy balance that sets the structure of the interstellar medium (ISM) phases, which in turn control the processes of star-formation (SF). Understanding the energy balance of the ISM is an essential step towards understanding the processes which shape evolution of galaxies across the cosmic time, and lead to the diversity of galaxy properties in the Universe. This work focuses on M 31, an ideal laboratory to study the ISM due to its proximity, external perspective, and as it is a representative of the large, star-forming, metal-rich galaxies where most of the SF in the local Universe occurs. We present the Survey of Lines in M 31 (SLIM) with contributing new Integral Field Spectroscopic *Herschel* [C II] and Calar Alto H α data, which allow us to study the dominant neutral gas coolant – [C II] on ~ 50 pc scales. We combine archival *ISO* [C II] measurements in the bulge of M 31 with ancillary data to identify potential heating sources responsible for gas heating in the absence of young stars. For the first time in extragalactic studies, we directly constrain the ISRF intensity and spectral shape, based on PHAT modelling of the spectral energy distributions (SEDs) and extinction of the individual stars in M 31 from the PHAT.

We find that a significant amount (~ 20 – 90%) of the [C II] emission comes from outside SF regions. We find that the [C II] – SFR correlation holds even at the small scales (~ 50 pc), although the relation typically has a flatter slope than found at larger (\sim kpc) scales, where [C II] traces the SFR approximately linearly. The photoelectric (PE) heating mechanism seems as the largest contributor to gas heating (where FUV flux is generated by evolved stellar populations), however photoionization and cosmic rays heating mechanisms are likely to be responsible for the observed [C II] “excess” in the bulge. We also find that the attenuated UV energy relative to the total attenuated energy correlates well with the [C II]/TIR ratio, suggesting that it is the soft photon heating of dust that is driving the variation in the [C II]/TIR ratio across this disk. We propose that a better method to approximate the PE heating efficiency (than [C II]/TIR) is an estimate of the energy absorbed by dust in the PE heating wavelength range (UV_{att}), that together with the [C II] emission allows us to determine the “true” PE efficiency $[CII]/UV_{att}$. Our preliminary results suggest that the UV_{att} is generated predominantly by B0–B3 type stars ($\sim 60\%$), and only approximately 30% is coming from O-stars. This means that in M 31, SFR tracers such as UV & [C II] might be dominated by heating generated by stars ~ 10 Myr old, not only recent SF, which would lead to the overestimate of SFRs.

ZUSAMMENFASSUNG

Das Ziel dieser Arbeit ist die Untersuchung des Energiegleichgewichtes, welches die Phasen des interstellaren Mediums (ISM) festlegt und damit die Sternentstehung in der Galaxie kontrolliert. Das Studienobjekt dieser Arbeit ist die Spiralgalaxie M 31. Diese Galaxie wurde ausgewählt, da sie die nächste Galaxie zur Milchstraße ist, die wir von außen beobachten können und die ein typischer Vertreter der Klasse von massereichen Galaxien mit hoher Metallizität ist, in denen die meisten Sterne in unserem lokalem Universum entstehen. In unserem Linienkatalog “Survey of Lines in M 31” (SLIM) präsentieren wir neue Integral-Field-Spektroskopiedaten von *Herschel* [C II] sowie Calar Alto $H\alpha$ Beobachtungen. Durch diese Daten wird es möglich den hauptverantwortlichen Stoff für die Kühlung des ISMs, [C II], auf Skalen von ~ 50 pc zu untersuchen. Außerdem kombinieren wir bereits existierende *ISO* [C II] Messungen im Zentrum (Bulge) von M 31 sowie zusätzliche weitere Beobachtungen um mögliche Heizquellen zu identifizieren, die das Gas auch ohne das Vorhandensein junger Sterne heizen können. Zum ersten mal überhaupt wird in dieser Arbeit die ISRF-Intensität und deren spektrale Form mittels PHAT-Modellierung der spektralen Energieverteilung (SED) und Absorption der Strahlung von einzelnen Sternen innerhalb von M 31 untersucht. Wir stellen fest, dass ein signifikanter Teil der [C II]-Strahlung ($\sim 20\text{--}90\%$) ihren Ursprung außerhalb der Sternentstehungsgebiete hat. Ein weiteres Resultat ist, dass die Korrelation zwischen der [C II]-Emission und der Sternentstehungsrate selbst bei kleinen Skalen von ~ 50 pc ihre Gültigkeit nicht verliert. Diese Korrelation ist allerdings typischerweise weniger steil als auf kpc-Skalen, bei denen man eine lineare Korrelation beobachtet. Der photoelektrische Heizprozess scheint den größten Anteil beim Heizen des Gases zu haben. Die dafür notwendige ferne UV-Strahlung wird von der Population der älteren Sterne bereitgestellt, welche sich bereits von der Hauptreihe wegentwickelt haben. Der Überschuss in der [C II]-Emission, der im Zentrum (Bulge) von M 31 beobachtet wird, wird allerdings höchstwahrscheinlich durch Photoionisation und der Absorption von kosmischer Strahlung hervorgerufen. Darüberhinaus ermittelten wir, dass die Abschwächung der UV-Strahlung gegenüber der totalen Energieabschwächung mit dem [C II]/TIR-Verhältnis korreliert. Dies könnte darauf hinweisen, dass das Heizen von Staub durch weiche Photonen für die Variation des [C II]/TIR-Verhältnisses innerhalb der Scheibe verantwortlich ist. Wir schlagen eine bessere Methode zur Bestimmung der photoelektrischen Heizeffizienz als die Benutzung des [C II]/TIR-Verhältnisses vor: Eine Abschätzung der Energie der Strahlung, die vom Staub in den Wellenlängen relevant für den photoelektrische Heizprozess absorbiert wird (UV_{att}), kombiniert mit der [C II]-Emission erlaubt es uns die wahre photoelektrischen Heizeffizienz $[CII]/UV_{att}$ zu bestimmen. Unsere vorläufigen Ergebnisse scheinen darauf hinzuweisen, dass die UV_{att} -Strahlung vorzugsweise von Sternen des Spektraltyps B0–B3 erzeugt wird und nur ungefähr 30% von O-Sternen stammt. Schlussendlich bedeutet dies, dass in M 31 typische Indikatoren für Sternentstehung, so wie UV & [C II], durch das Heizen durch Sterne in einem Alter von ~ 10 Millionen Jahren dominiert werden und nicht nur durch eine kürzlich zuvor aufgetretene Phase der Sternentstehung. Eine Vernachlässigung des ersten Prozesses würde daher zu einer Überschätzung der Sternentstehungsrate führen.

ACKNOWLEDGEMENTS

There are no words to describe how thankful I am to Karin Sandstrom and Brent Groves for believing in me and for their continuous support throughout the almost 4-years of my PhD, here at the MPIA. Even after moving to new positions in the remote locations of Tucson and Canberra, they kept providing me with great scientific and moral support. I am deeply grateful to Fabian Walter and Morgan Fouesneau for their wise and kind mentoring after Karin's and Brent's departure. My thanks also go to Hans-Walter Rix for being there when I most needed his advice and scientific input. I am also grateful for an amazing trip to the Grand Canyon we had together with his wife Mary-Beth and with Yancy Shirley. I am much obliged to my thesis committee members Hans-Walter Rix and Simon Glover for reading and evaluating this thesis on short notice. At the Institute, I enjoyed sharing an office during both bright and dark times with Aiara Lobo-Gomes and Sara Rezaeikhoshbakhat. Finally, there are number of collaborators and people who contributed to the successful completion of this thesis: Eva Schinnerrer, Julianne Dalcanton, Karl Gordon, Kathryn Kreckel, Kevin Croxall, Jürgen Stutzki, Suzanne Madden, Alberto Bolatto, Alexia Lewis, Dan Weisz, Cliff Johnson, Sharon Meidt, Adam Leroy, JD Smith, Xander Tielens, Frank Israel, Jorge Pineda, Paul Goldsmith and David Hogg.

On a private note, I am grateful to my partner Michał Łyczek for his understanding, unwavering support and for following me wherever my work takes me. I cannot thank enough my parents for their love and encouragement that made me who I am and enabled me to be where I am.

CONTENTS

1	INTRODUCTION	1
1.1	THE MULTIPHASE ISM	3
1.1.1	MOLECULAR PHASE	3
1.1.2	ATOMIC PHASE	4
1.1.3	IONIZED PHASE	5
1.2	DUST HEATING AND COOLING	5
1.2.1	DUST COMPOSITION AND SIZE DISTRIBUTION	6
1.2.2	DUST ABSORPTION AND SCATTERING	7
1.2.3	DUST EMISSION	7
1.2.4	PHOTOELECTRIC EFFECT	8
1.3	GAS COOLING	9
1.3.1	[C II] 158 μM COOLING	10
1.3.2	[C II] EMISSION AS A SFR TRACER	10
1.3.3	FIR LINE “DEFICIT”	14
1.4	STELLAR HEATING OF THE ISM	15
1.4.1	INTERSTELLAR RADIATION FIELD IN THEORY	15

1.4.2	ISRF IN OBSERVATIONS	16
1.5	OUTLINE	18
2	THE SURVEY OF LINES IN M 31 (SLIM): INVESTIGATING THE ORIGINS OF [C II] EMISSION	21
2.1	INTRODUCTION	21
2.2	DATA	25
2.2.1	<i>Herschel</i> PACS SPECTROSCOPY	26
2.2.2	PPAK IFS	28
2.2.3	<i>Spitzer & Herschel</i> PHOTOMETRY	31
2.2.4	FURTHER PROCESSING	32
2.2.5	DERIVED QUANTITIES	32
2.3	RESULTS	34
2.3.1	[C II] FROM SF REGIONS	34
2.3.1.1	DELINEATING SF REGIONS	34
2.3.1.2	FRACTION OF [C II] AND OTHER TRACERS FROM SF REGIONS	36
2.3.2	THE CORRELATION BETWEEN [C II] AND Σ_{SFR}	38
2.3.2.1	THE CORRELATION BETWEEN [C II] AND Σ_{SFR} ON 50 PC SCALES	39
2.3.2.2	[C II] VS Σ_{SFR} ON ~ 700 PC SCALES	39
2.3.3	FAR-IR LINE DEFICIT	42
2.3.3.1	FAR-IR LINE DEFICIT ON ~ 50 PC SCALES	43
2.3.3.2	FAR-IR LINE DEFICIT ON ~ 700 PC SCALES	45
2.4	DISCUSSION	47
2.4.1	[C II] ON ~ 50 PC SCALES	47
2.4.2	[C II] ON ~ 700 PC	49
2.5	CONCLUSIONS	51
3	NON-SF HEATING RELATED [C II] EMISSION IN THE BULGE OF M 31	53

3.1	INTRODUCTION	53
3.2	DATA & TECHNIQUE	55
3.2.1	ANCILLARY MULTIWAVELENGTH DATA	57
3.2.1.1	GALEX & SDSS	57
3.2.2	METALLICITY	58
3.2.3	PROCESSING	58
3.2.3.1	MAGPHYS SED FITTING TECHNIQUE	59
3.2.3.2	ATTENUATED STELLAR EMISSION	59
3.3	[C II] EMISSION IN THE BULGE AND DISK OF M 31	60
3.4	TOTAL ENERGY BUDGET IN THE BULGE	63
3.4.1	GAS COOLING	63
3.4.2	PHOTOELECTRIC HEATING	63
3.4.3	PHOTOIONIZATION HEATING	64
3.4.4	SHOCKS/TURBULENCE AND X-RAY HEATING	65
3.4.5	COSMIC RAYS HEATING	66
3.4.6	ENERGY BALANCE IN THE BULGE OF M 31 SUMMARY	66
3.5	ENERGY BALANCE IN THE BULGE VS DISK	67
3.6	DISCUSSION AND CONCLUSIONS	69
3.A	A CAVEAT ABOUT TIR PRESCRIPTIONS/APPROXIMATIONS IN A BULGE	72
3.B	MAGPHYS SED MODELING ACROSS M 31	73
4	STELLAR POPULATIONS RESPONSIBLE FOR HEATING THE ISM IN M 31	79
4.1	INTRODUCTION	79
4.2	METHODOLOGY	81
4.3	THE SPATIALLY RESOLVED DATA	83
4.3.1	PHAT SURVEY	84
4.3.1.1	PHAT PHOTOMETRY & KNOWN <i>HST</i> ISSUES	85

4.3.2	BEAST SED FITTING OF INDIVIDUAL STARS	86
4.4	THE SPATIALLY UNRESOLVED DATA	86
4.4.1	CLUSTERS AND CITIZEN SCIENCE	87
4.4.2	SFH CATALOGS	88
4.4.3	INTEGRATED PHOTOMETRY	89
4.4.3.1	GALEX	89
4.4.3.2	SDSS	89
4.4.3.3	SPITZER	89
4.4.3.4	HERSCHEL PACS AND SPIRE	90
4.4.3.5	IR DATA PRODUCTS – DUST SED FITTING	91
4.5	ANALYSIS & RESULTS	91
4.5.1	THE REGION SELECTION AND IMAGE PROCESSING	91
4.5.2	BEAST_v0 CATALOGS – MEASURING UV_{att}	93
4.5.3	STELLAR POPULATIONS CONTRIBUTING TO THE UV ISRF	93
4.5.4	COMPLETENESS AND OTHER ISSUES	94
4.5.4.1	ISSUES WITH THE EARLY VERSION OF BEAST	97
4.5.5	EXTINCTION FROM STARS VERSUS DUST COLUMN	99
4.5.6	ISSUES WITH MEASURING ISRF ON DIFFERENT SPATIAL SCALES	100
4.5.7	COMPARISON OF UV_{att} AND TOTAL DUST EMISSION	100
4.6	OUTLOOK AND IMPROVEMENTS USING BEAST_v1	101
4.7	CONCLUSIONS	102
4.A	PHOTOMETRIC SYSTEMS	102
5	SUMMARY	107
5.1	OUTLOOK	109
5.1.1	SOFIA FIFI-LS OBSERVATIONS IN THE BULGE	110
5.1.2	UPGRADED BEAST STELLAR CATALOGS	111

5.1.2.1	APPLICATION OF OUR METHODOLOGY IN LOW-METALLICITY ENVIRONMENTS OF THE MAGELLANIC CLOUDS	111
5.1.3	LONG-TERM PERSPECTIVES	112
	LIST OF FIGURES	115
	LIST OF TABLES	119
	BIBLIOGRAPHY	121

CHAPTER 1

INTRODUCTION

The energy balance of the interstellar medium (ISM) is the balance between the heating and cooling processes, that sets the structure of the ISM phases, which in turn control the processes of star-formation (SF). The feedback from the SF influences the structure of the ISM phases, and consequently affects the efficiency of SF. Therefore, understanding the energy balance of the ISM is an essential step towards understanding the processes which shape evolution of galaxies across the cosmic time, and lead to the diversity of galaxy properties in the Universe.

Observationally characterizing the energy balance requires an assessment of both gas heating and cooling. Heating is mainly powered by young stars, whose UV radiation ionizes gas and ejects photoelectrons from dust grains. Cooling is controlled by dust emission, recombination lines in ionized regions, and far-IR line emission from neutral gas. Empirically, multi-wavelength studies such as those that will be presented in this thesis can track the major contributors to each of the mechanisms, their spatial and spectral distributions.

The gas in the ISM exists in multiple phases. Generally, the ISM is divided into three states; molecular, atomic and ionized. Each element or molecule has a unique ionization and dissociation energy, but we describe a volume of interstellar gas based on the ionization state of the most abundant element: hydrogen. In the Milky Way (MW) about 60% of interstellar hydrogen is atomic, $\sim 20\%$ ionized and $\sim 20\%$ molecular (Draine 2011).

The structure of the ISM phases is controlled by heating and cooling. The more heating is inserted into the ISM, the warmer and more diffuse it becomes. Input energy can also dissociate molecular gas and ionize atomic gas. If the cooling starts to dominate, the inverse processes occur more often, resulting in cooler, denser and more neutral ISM.

The basic ISM states (molecular, atomic and ionized) are further divided into characteristic phases based on temperature and density (see Table 1.1). The division of gas into phases appears to reflect different stages of the cycle of energy and mass in galaxies, and studying them helps to understand underlying physical processes (i.e. see Figure 1.1).

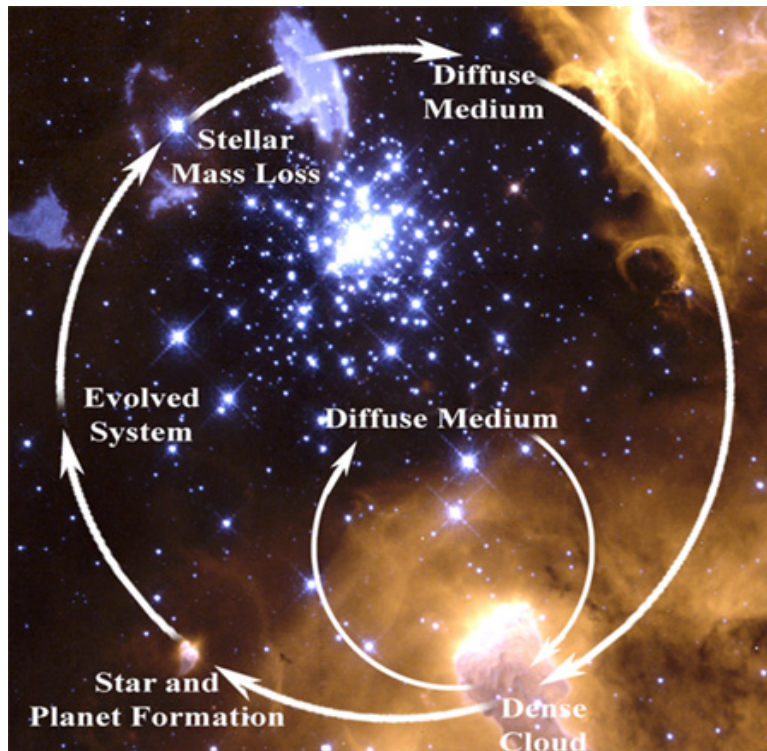


FIGURE 1.1: *HST* image has been modified by NASA to illustrate the cycle of energy and matter in the ISM. Stars form and produce heavier elements by nuclear fusion. Evolving stars heat and enrich the surrounding ISM, while ISM cools and condenses from the diffuse medium, and the cycle start over. [Figure adapted from NASA.]

We can outline a simplified version of the cycle of material in the ISM as the following:

- formation of stars from the dense molecular clouds,
- stellar radiation and mechanical (wind) feedback on the natal clouds, causing gas heating, dissociation, ionization and suppressing of the ongoing star-formation,
- stellar energy and mass loss continue during the stellar evolution (i.e. finished with Supernovae explosions),
- diffuse medium cools and condenses (recombines to atoms and molecules), and forms dense molecular clouds.

In this thesis, we study the energy balance of the ISM. To trace the ISM phases as described above requires a multiwavelength dataset. We do this in the Andromeda galaxy (NGC 224, M 31) as it has the necessary multiwavelength coverage (to trace the ISM phases as described above), proximity (to allow high spatial resolution), external perspective (to avoid line-of-sight confusion present in any photometric or not resolved spectroscopic observations of the Galaxy), and it is a representative of the large, star-forming,

TABLE 1.1: *Phases of the interstellar gas*^a

Phase	n_{H} [cm^{-3}]	T [K]	f_{V} ^b
Hot Ionized Medium (HIM)	0.003	10^6	~ 0.5
H II regions (coronal)	$1-10^5$	10^4	~ 0.1
Warm Ionized Medium (WIM)	0.1	8000	~ 0.25
Warm Neutral Medium (WNM)	0.5	8000	~ 0.3
Cold Neutral Medium (CNM)	50	80	~ 0.01
Diffuse Molecular	100	50	~ 0.001
Dense Molecular	10^3-10^6	$50-10^3$	$\sim 10^{-4}$

^a table based on Tielens (2005); Draine (2011)

^b volume filling factor

metal-rich galaxies where most of the star formation in the local Universe occurs (Karim et al. 2011). The data set we have assembled spans from FUV to sub-millimeter wavelengths, includes imaging (GALEX, Hubble Space Telescope (HST), *Spitzer Space Telescope*, *Herschel Space Observatory*) and spectroscopy (Calar Alto PMAS/PPAK and *Herschel PACS*). This unique and broad wavelength coverage lets us trace the dominant heating and cooling processes in a variety of ISM phases. We study the origins of [C II] 158 μm emission – the brightest far infrared (FIR) cooling line – and the utility of [C II] emission as star-formation rate (SFR) tracer. We analyze the effects of environment on the [C II] emission, by investigating its emission arising from the bulge of M31 in the absence of young stars, and attempt to assess the contributions from various heating mechanisms/sources. Finally, we estimate energy contribution of various stellar populations to the ISM heating.

In this Chapter we describe the ISM phases (Section 1.1) and give an overview of key ISM energetic processes relevant to this thesis: dust cooling (Section 1.2), gas cooling via [C II] emission line (Section 1.3.1), stellar heating (Section 1.4), and the current understanding of the associated physical processes.

1.1 THE MULTIPHASE ISM

1.1.1 MOLECULAR PHASE

Cold molecular hydrogen itself is essentially unobservable, as the hydrogen molecule is symmetric, therefore does not have a dipole moment. There are no radiative transitions between ortho- H_2 and para- H_2 molecule states (spins of H nuclei parallel and antiparallel, respectively), and all ro-vibrational transitions within the electronic ground state have very low spontaneous emission coefficients. There are mechanisms through which H_2 can be excited, e.g. FUV radiative pumping into molecule's electronically excited states (high vibrational levels), causing optical and infrared fluorescent emission (radia-

tive cascade), or inelastic collisions in high density and temperature gas (such as found in shocks). As a result, the only cases where one can trace H_2 directly are in very warm conditions near UV bright stars or in shocks. The majority of H_2 is in dense, cold clouds where the H_2 molecule is not sufficiently excited to emit.

The CO molecule is one of the most abundant molecules in the ISM after hydrogen, and has strong dipole moment that leads to line emission that can be excited at low temperatures. For these reasons CO is one of the dominant coolants of molecular gas, and is the typical tracer of the total molecular mass. To convert between observed CO line intensities and the molecular gas mass, a conversion factor called X_{CO} is used. The conversion factor between the line flux of the lowest transition, CO(1-0), and the molecular gas column is $X_{\text{CO}} = 2 \times 10^{20} \text{ cm}^{-2} (\text{K km s}^{-1})^{-1}$ with $\pm 30\%$ uncertainty (in the MW; Bolatto et al. 2013). The MW X_{CO} does not apply in all conditions, however. Because H_2 can self-shield against the radiation that will dissociate it, CO is not abundant enough and relies upon dust to shield against the dissociating radiation. Thus in low dust environments, H_2 may exist without CO, the so-called ‘‘CO-dark- H_2 ’’ gas, meaning assuming a constant X_{CO} value will lead to an underestimation of the total molecular gas mass (Wolfire et al. 2010; Glover & Clark 2012; Smith et al. 2014).

Most of the mass of molecular gas is in giant molecular clouds (GMCs), confined mostly in the galactic plane. The boundaries of GMCs are debatable, but at $A_V \sim 3 \text{ H}_2$ photodissociation can be reduced by 3–5 orders of magnitude (lecture by S. Glover). Observations yield typical 10–80 pc sizes of clouds with median masses $\sim 3.5 \times 10^4 M_\odot$ in M 31 (thesis of A. Schruba). Diffuse molecular gas has larger scale heights than gas bound in GMCs (~ 200 pc in M 51; Pety et al. 2013).

1.1.2 ATOMIC PHASE

Fortunately, atomic gas can be much more easily traced than H_2 via the 21 cm hyperfine emission line that one can observe at radio wavelengths. This is a forbidden transition that occurs when relative spins between proton and electron flip from parallel to antiparallel. The 21 cm transition of H I can be excited collisions or the so-called Wouthuysen-Field effect (Hirata 2006).

Atomic gas is more diffuse than molecular gas (see Table 1.1), it extends to larger galactocentric radii (2–4 times the optical radius; Bigiel & Blitz 2012) and larger scale heights (an average full-width half-maximum $z_{\text{FWHM}} \sim 230$ pc) than the thin and compact molecular disk ($z_{\text{FWHM}} \sim 110$ pc; in the inner Galaxy, assuming a Gaussian emissivity distribution vertical to the plane; Langer et al. 2014a). Interestingly, Langer et al. (2014a) measured $[\text{C II}] z_{\text{FWHM}} \sim 172$ pc, which is intermediate between molecular and atomic, and suggest that $[\text{C II}]$ emission might trace both atomic and molecular gas.

There have been many studies on gas distributions in galaxies. Central holes in the H I distribution of galaxies are commonly observed, while molecular gas is typically much

more concentrated in the central regions (restricted to the optical disk) and trace SFR better (Leroy et al. 2012, 2013). Molecular clouds appear in the high density H I gas, especially in spiral arms and filaments, which is a consequence of the H I transition to H₂ that occurs above a typical column density of $\sim 10 M_{\odot} \text{pc}^{-2}$.

1.1.3 IONIZED PHASE

Warm ionized gas (see Table 1.1 for details) can be traced by optical and UV absorption lines against background sources, radio free-free emission, and through H α recombination line emission. The first method has a limited applicability to certain lines-of-sight. The latter method is more widely applicable. Generally, WIM is concentrated around the most massive stars (O-stars), or in a diffuse ionized phase associated mostly with the diffuse atomic gas. The heating source of this phase far away from H II regions is unclear, but it possibly come from “leaky” H II regions or from ionization powered by sources that other than massive/young stars that happens in the diffuse ISM. In the former case though, it would require from ionizing photons not only escape, but travel over distances as large as hundreds of parsecs without being absorbed by ubiquitous H I. In MW most of the H α luminosity arises from H II regions, while almost all of the ionized gas mass reside in a diffuse component ($\sim 10^9 M_{\odot}$). The WIM has a large scale height of ~ 1 kpc. The WIM has been detected in early-type galaxies, but its heating sources has been heavily disputed. Yan & Blanton (2013) ruled out AGN and shocks as dominant ionization mechanism, and suggest hot evolved stars as the favorite candidates, as they find that ionizing sources follow the stellar density profile.

Hot ionized medium can be traced by UV absorption lines (e.g. C IV, N V, O VI), which has similar limitations due to bright background source requirement. This hot coronal gas emits continuum (i.e. bremsstrahlung) and line (i.e. collisional excitation) radiation in X-ray and hard UV wavelength range. Supernovae explosions and shocks driven by stellar winds from massive stars are responsible for heating this gas phase. HIM fills most of the halo volume, up to ~ 3 kpc. It has been suggested/proposed that this hot gas is blown off-the-plane via superbubbles (i.e. created by stellar feedback, winds), but when it cools, travels down back to the galactic plane.

1.2 DUST HEATING AND COOLING

Although dust mass makes a tiny fraction $\sim 1\%$ of the ISM mass of a MW-like galaxy, it absorbs and reemits $\sim 50\%$ of the starlight in a typical galaxy (Dale et al. 2007). It is also apparent in the fraction of energy in the Universe emitted in infrared (Cosmic infrared background radiation; Chary & Elbaz 2001). It therefore plays a key role in the energy balance of the ISM.

Dust is another component of the ISM which is thought to be distributed throughout the ionized, atomic, and molecular phases. Dust is thought to be well mixed with gas, although the dust-to-gas ratio varies between and across galaxies. The dust-to-gas ratio is proportional to the gas-phase metallicity, therefore can be a very useful diagnostic tool (with more details in the following Section).

Although dust absorbs and scatters radiation (mostly in UV and optical), it is more than an obstacle that we have to correct for when observing stars, galaxies etc., it is an important ISM component, which also plays a major role in galaxy evolution. Firstly, it efficiently blocks UV radiation, allowing molecular clouds to form and survive. Secondly, dust serves as a catalyst for H_2 formation on dust grain surfaces. Thirdly, dust plays a major role in the heating of the diffuse ISM through the photoelectric effect, therefore understanding dust distribution and dependence on environment is crucial i.e. for understanding the gas heating efficiency.

Although the following Chapters do not focus primarily on dust, it plays an important role in each of them, so we discuss its properties in more detail below.

1.2.1 DUST COMPOSITION AND SIZE DISTRIBUTION

The composition of the dust is thought to be a mixture of mostly silicates, graphites, amorphous carbon, hydrocarbons, metallic iron, oxides of silicon, magnesium and iron. It is difficult to identify precisely the materials and their fractional contributions to dust grains, because the dust absorption is mostly a continuum, and the existing spectral features are hard to identify (they are broad, and the spectral data compiled in the laboratories for comparison, while growing fast, are still incomplete).

Alternatively, one can infer elemental dust composition from the underabundant elements in the gas phase (i.e. assuming their abundances are similar to the solar photosphere). From the spectroscopic absorption line observations, it has been shown that C, Mg, Si and Fe elements are depleted in the gas phase. Depletion of C is estimated to be about 40%, while of the other heavier elements 90% or more (Kimura et al. 2003; Jenkins 2009). The “missing” amounts from the gas are presumably incorporated in the solid form, dust.

The dust-to-gas ratio is generally observed to be proportional to the gas-phase metallicity, because grains are made mostly out of carbon atoms (except ubiquitous hydrogen atoms), and C is a heavier element than H and He. If the depletion factors are the same as the MW (see above), one gets $M_d/M_H \approx 0.0091 \times Z/Z_\odot$ (Draine et al. 2014).

From observations of the dependence of absorption and scattering (i.e. extinction) on wavelength, one can learn about the dust grain size and shape distribution. The isotropic starlight that has been scattered is polarized, suggesting that at least some dust grains are nonspherical and aligned (i.e. in along the magnetic field lines). The size distribution is

broad, ranging from a $\sim 0.01 \mu\text{m}$ to $\sim 0.2 \mu\text{m}$. The boundary between the smallest dust grains and the large polycyclic aromatic hydrocarbon (PAH) molecules is vague, but it is probably somewhere in the $10^3 - 10^4$ atom range, thus the lower grain size boundary is $\sim 3.5 \text{ \AA}$. The grain size distribution is often approximated by a power-law $dn/da \propto a^{-3.5}$ (as a first order approximation under the assumption of spherical grains; Mathis et al. 1977).

1.2.2 DUST ABSORPTION AND SCATTERING

Extinction caused by dust is the sum of absorption and scattering processes. Extinction is a function of wavelength, and generally it decreases with increasing wavelength (see averaged extinction curves with and without the characteristic bump at 2175 \AA in Figure 1.2). Both absorption and scattering efficiencies are grain size dependent.

It is convenient to consider relative extinction using the formula

$$\frac{A_\lambda}{A_V} = \frac{1}{R_V} \frac{E(\lambda - V)}{E(B - V)} \quad (1.1)$$

which is parameterized by only one parameter

$$R_V = \frac{A_V}{E(B - V)} \quad (1.2)$$

where A_λ is the extinction at λ , $E(B - V) = A_B - A_V$ is the color excess (attenuated stars appear redder). The average reddening constant in the Milky Way has been determined by Schultz & Wiemer (1975), to be $R_V = 3.14 \pm 0.10$.

1.2.3 DUST EMISSION

The energy that is absorbed by dust in the UV and optical, as described in the previous Section, contributes to both heating the grain and ejecting electrons via the photoelectric effect. Dust emits thermal radiation between $\sim 5 - 600 \mu\text{m}$. At wavelengths longer than $\sim 50 \mu\text{m}$ dust emission can be approximated as thermal equilibrium emission (in the disks of MW and M 31 the best fit temperature is $\sim 17 \text{ K}$), while below $\sim 50 \mu\text{m}$ it is a combination of thermal emission of hot dust, and vibrational emission MIR bands from PAHs (3.3, 6.2, 7.7, 8.6, 11.3, $12.7 \mu\text{m}$) and emission from stochastically heated small dust grains.

The peak of the dust emission, indicating average dust temperature, will shift towards the shorter wavelengths when exposed to more intense radiation fields. If we use the Draine (2011) steady state grain temperature model (thermal dust grains equilibrium), and assume a constant emissivity slope $\beta = 2$ typically used for starlight heating, the

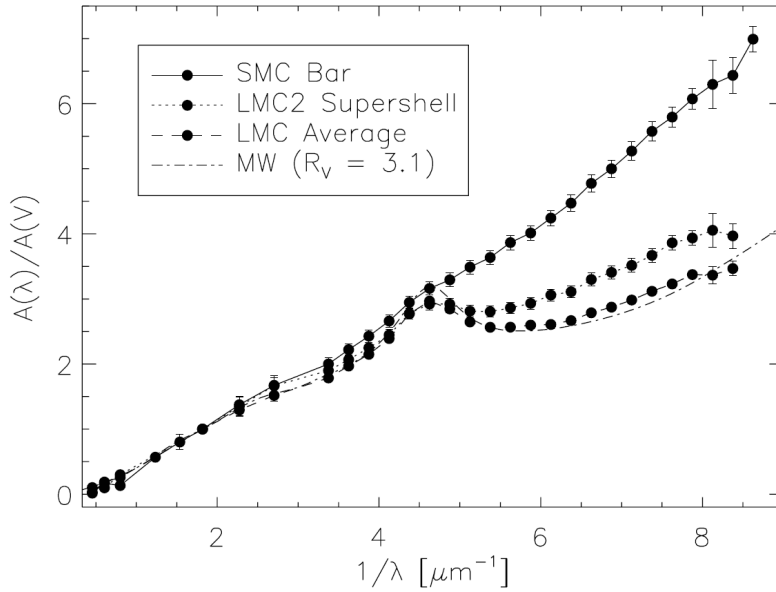


FIGURE 1.2: Average extinction curves of the SMC, LMC (Gordon et al. 2003) and MW (Cardelli et al. 1989). [Figure adapted from Gordon et al. (2003)]

dust temperature (T_d) relation to the heating stellar radiation field density (U_*) can be simplified to

$$T_d \propto U_*^{1/6}. \quad (1.3)$$

Observationally, from *Herschel* and *Spitzer* photometry and spectroscopy we can measure overall dust parameters (temperature, surface density and total emission). The total infrared emission (TIR) can be estimated by fitting a modified black body to dust emission, and integrating it in range 8–1000 μm (for details see Section 4.4.3.5).

1.2.4 PHOTOELECTRIC EFFECT

Not all of the energy absorbed by dust goes to grain heating, some fraction of the UV energy goes into ejecting electrons. The photoelectric (PE) effect is an interaction between the incident photon with energy exceeding the work W and the Coulomb potential ϕ required to eject an electron from the dust grain. ϕ is larger, i.e. when a dust grain has already ejected a photoelectron.

The probability that absorption of a photon of energy $h\nu$ will result in a photoelectron is called the “photoelectric yield” Y_{PE} . The photoelectric yield is a function of the incident photon of energy, the composition and size of the grain, and the charge of the grain before the event (see fig. 1.3). This means that the photoelectric heating efficiency might change. For example, a given photon flux from young star that illuminates a population

of bigger dust grains, will result in less energy transferred to the gas. This PE efficiency plays a key role in the determination of how much energy from stars is able to heat the gas, and is one of the main points examined in this thesis.

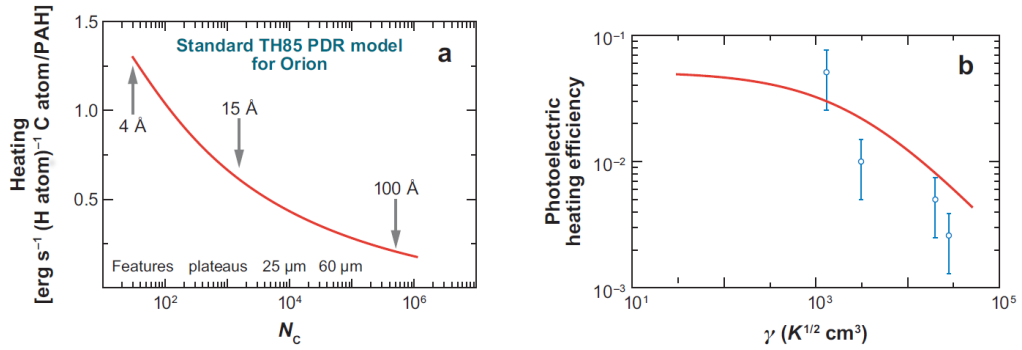


FIGURE 1.3: The efficiency of PE heating as a function of grain size (left panel) and charge (right panel). Left panel: Note that typically around half of the heating arises from polycyclic aromatic hydrocarbons (PAHs), while the other half from very small grains ($15 \text{ \AA} < a < 100 \text{ \AA}$). Large grains contribution to the heating is negligible. Right panel: The PE efficiency as a function of the charging parameter, $\gamma = G_0 T^{1/2} / n_e$. The charge of species increases to the right. The measured heating efficiency are shown by blue points for the diffuse ISM sight lines ζ Oph and ξ Per, and the PDRs NGC 2023 and the Orion Bar. [Figure adapted from Tielens (2008)]

1.3 GAS COOLING

Gas cooling occurs when atoms or molecules produce line emission that escapes the region (i.e. is not immediately re-absorbed by the gas). Typically, hydrogen recombination lines dominate cooling in the ionized phase, [C II] and [O I] lines in the neutral phase, and CO rotational transition lines in the molecular phase.

Collisional excitation of ions, atoms and molecules is important because one of their way to de-excite is the radiative decay, which results in gas cooling. For example [C II] and [O I] lines dominate cooling of atomic gas (Hollenbach & Tielens 1999). The other aspect is that we can learn about the physical conditions of the gas (density, temperature, radiation field) from the observations of the emission or absorption lines which allow us to determine the level populations. Even lines that are not dominant coolants still provide useful information about the gas properties, like abundances (i.e. [N III]/[O III]), densities (i.e. [N II] [O III], [S III] line pairs), gas pressure (i.e. [O I] pairs), UV hardness and intensity ([N II]/[N III], [S III]/[O III] pairs).

1.3.1 [C II] 158 μM COOLING

[C II] 158 μm is the forbidden line emission of ionized carbon, between its only two fine structure levels in the ground electronic state $^2P_{3/2} \rightarrow ^2P_{1/2}$ (see Figure 1.4). The spontaneous radiative decay rate from the excited state is $2.3 \times 10^{-6} \text{ s}^{-1}$ (Goldsmith et al. 2012, and references therein). The [C II] 158 μm emission line is one of the most important coolants of the ISM, one of the brightest emission lines in galaxies and is often used to estimate star-formation rates. Ionized carbon is widespread in the ISM, due to its high abundance relative to hydrogen (1.4×10^{-4} , making it the fourth most abundant element), and ionization potential lower than hydrogen (11.2 eV).

The fine-structure transition of [C II] can be collisionally excited via encounters with hydrogen molecules, atoms and electrons. The equivalent temperature of the excited level is $T = E_{ul}/k = 91.25 \text{ K}$ above the ground state. Although the transition is excited over a wide range of temperatures $\sim 100\text{--}10^4 \text{ K}$, and densities ($n_H \sim 1\text{--}10^4 \text{ cm}^{-3}$), see Goldsmith et al. (2012) for review, its excitation rate is fairly insensitive to temperature (especially between 100 K and 5000 K), while it is sensitive to density (almost linearly between $0.1\text{--}10^3 \text{ cm}^{-3}$) (see Fig. 1.5; Draine 2011).

The critical density for hydrogen atoms as a collision partner is $n_{crit}(H) \sim 10^3 \text{ cm}^{-3}$, and for electrons it is $n_{crit}(e^-) \sim 7\text{--}40 \text{ cm}^{-3}$, therefore the collisional deexcitation can be neglected for the WNM and CNM conditions (see Table 1.1). Due to much higher critical density $n_{crit}(H) \sim 5 \times 10^5 \text{ cm}^{-3}$ and excitation temperature $T_{exc} = 228 \text{ K}$ of [O I] 63 μm than [C II], for densities ($n_H \sim 10^3 - 10^6 \text{ cm}^{-3}$) and temperatures (resulting from illumination by $10^3 - 10^6$ more intense than ambient radiation fields), [O I] 63 μm line becomes the dominant coolant in extreme PDRs (more efficient than C+ line; Tielens & Hollenbach 1985).

Its strength and observability make [C II] detections possible even at high redshifts (Carilli & Walter 2013), i.e. [C II] has been measured at $z = 6.42$ (Walter et al. 2009). As a result, [C II] 158 line might allow us to constrain SF through redshift on a common scale, if its reliability as a SF indicator can be verified, which has fundamental consequences on our knowledge of stars and thus galaxy formation and evolution.

1.3.2 [C II] EMISSION AS A SFR TRACER

The physical motivation for using [C II] emission as a SFR tracer relies mostly on the assumptions of simple energy balance. If [C II] arises predominantly from photodissociation regions (PDRs), and these are heated by young massive stars and most of the cooling of the PDRs is via [C II], then [C II] should track SFR.

PDRs are adjacent regions to the H II regions (see Figure 1.6 for a simple model of a PDR's 1D layered structure). Young, massive stars create regions of ionized hydrogen,

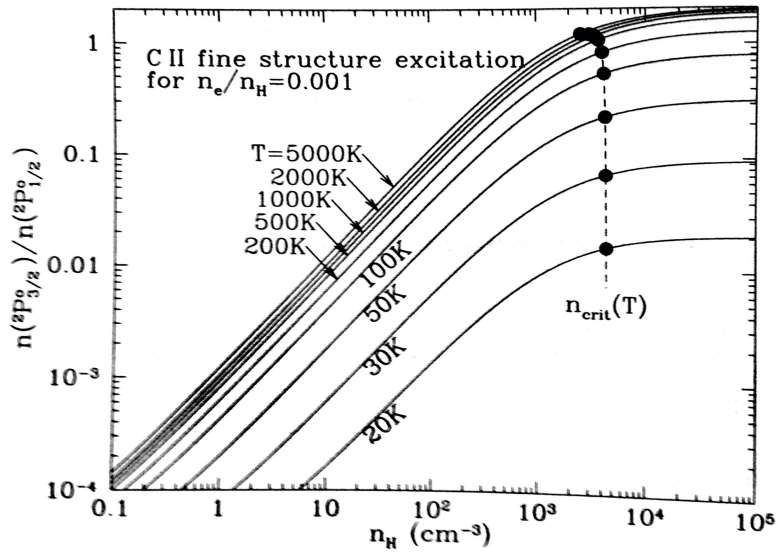


FIGURE 1.5: Excitation of the $^2P_{3/2}$ fine structure level of $[C II]$. The background radiation is assumed to be negligible at $158 \mu\text{m}$ (relative number of photons $\sim 10^{-5}$, hence, if a considered region is optically thin in the $158 \mu\text{m}$ line, one can neglect stimulated emission). It is clear that the excitation is fairly insensitive to temperature (especially between 100 K and 5000 K), while it is sensitive to density (almost linearly between $0.1\text{--}10^3 \text{cm}^{-3}$). [Figure adapted from (Draine 2011)]

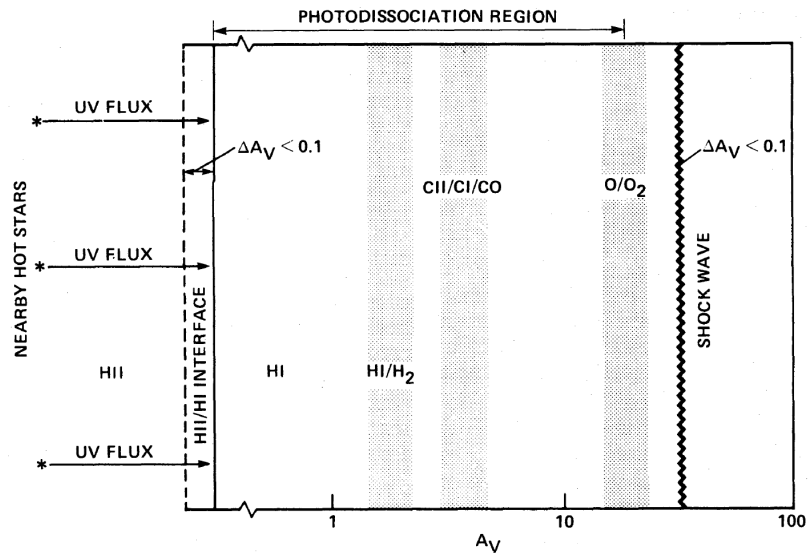


FIGURE 1.6: A scheme of a photodissociation region. The PDR is irradiated from the left side by a strong FUV photon flux. PDR is in a predominantly neutral phase, but it also includes molecular layers. [Figure adapted from Tielens (2005)]

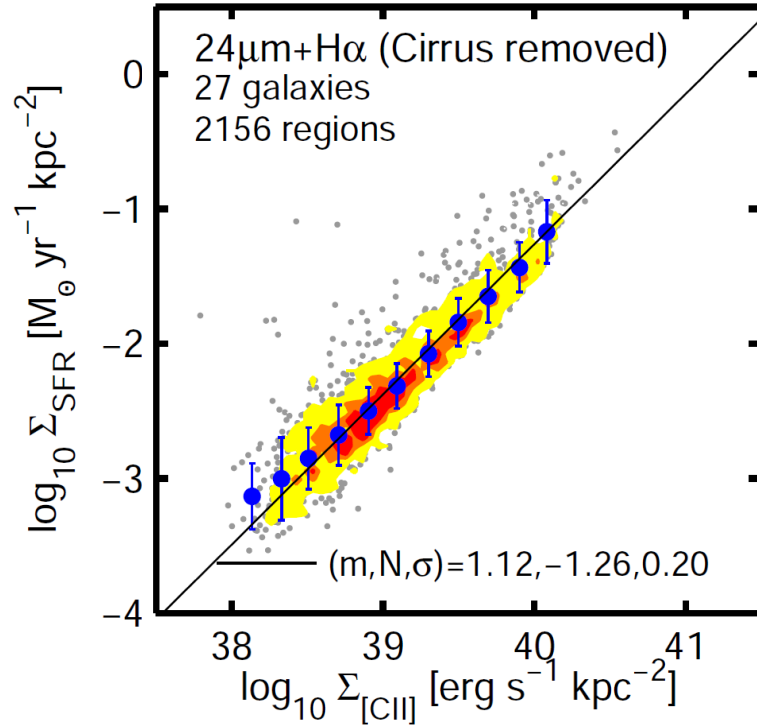


FIGURE 1.7: *SFR to [C II] surface densities relation in the spatially resolved sample of KINGFISH galaxies. Gray points indicate regions at 12'' resolution, while contours show number density plot. The best fit is plotted as black line, and its corresponding parameters slope (m), y-axis value at $x = 40$ (N) and $1\text{-}\sigma$ standard deviation in dex (σ) are given in the bottom. “Cirrus” emission means that $24\ \mu\text{m}$ images has been corrected for non-SF related contribution following a procedure from Leroy et al. (2012). [Figure adapted from Herrera-Camus et al. (2015)]*

($z \gtrsim 1$). On the other hand, once we have the data, by using the IR regime we avoid the problem of extinction.

Understanding the origins of [C II] emission is crucial in order to properly interpret the observations, especially on $\gtrsim \text{kpc}$ scales, where one integrate over many SF regions and phases. To disentangle the contributions of different phases to the [C II] emission, one can aim for (1) high spectral resolution observations enabling to fit multiple line profiles, thus spectrally separate these components (e.g. what has been done by the GOT C+ survey in the MW; Pineda et al. 2013), or for (2) high spatial resolution observations enabling to identify borders between these phases, this spatially separate these components. In this work, we use the latter approach.

1.3.3 FIR LINE “DEFICIT”

One contributing factor to the uncertainty connecting the [C II] line to star formation is that the FUV radiation from massive stars heats the gas indirectly, via photoelectrons ejected from dust grains (see Sec. 1.2.4).

The ratio of the [C II] line flux to the FIR emission is thought to be a tracer of this photoelectric yield, measuring the total energy absorbed by dust (via the FIR) versus that injected into the gas (via [C II]). Interestingly this ratio has been found to decrease with warmer dust colors, thought to be indicative of warmer dust temperatures (see Figure 1.8 from Helou et al. 2001). This FIR-line “deficit” may be caused by an increasingly positively charged dust grains with increased dust temperature (Malhotra et al. 2001; Croxall et al. 2012), or a reduction in the relative number of polycyclic aromatic hydrocarbons (PAHs) (Helou et al. 2001), or an increased ionization parameter (Graciá-Carpio et al. 2011), all reduce the photoelectric efficiency and can be associated with warmer dust colors.

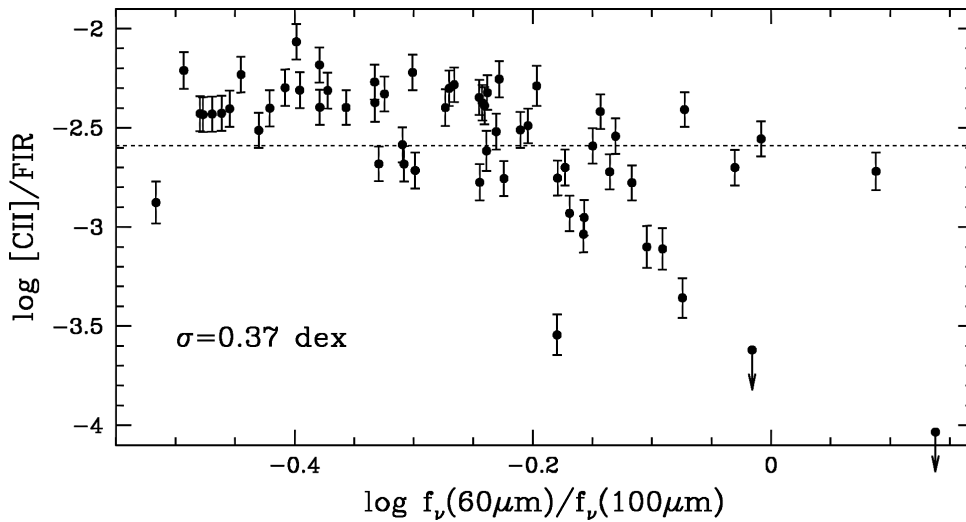


FIGURE 1.8: The ratio [C II]/FIR declines with dust color IRAS 60/100 μm , based on the ISO FIR lines observations of ~ 30 normal galaxies (Malhotra et al. 2001; Helou et al. 2001). FIR estimate has been computed according to Helou et al. (1988) formula, which uses IRAS 60 and 100 μm bands. Mean ratio is indicated by the dotted line with the given 1σ scatter around it. [Figure adapted from Helou et al. (2001)]

As the FIR is also indicative of SFRs (see e.g. Kennicutt & Evans 2012), the appearance of this FIR-line deficit might mean a non-linear scaling of the [C II] with the SFR (i.e. leading to underestimating SFRs in environments like ultra-luminous infrared and starburst galaxies, or even less extreme). We aim to disentangle which effects (stellar and/or dust properties) cause variations in the [C II]/TIR ratio across M 31.

1.4 STELLAR HEATING OF THE ISM

Generally, the ISM can be heated locally by luminous massive stars, or by a diffuse interstellar radiation field. The relative contribution of these two different components to gas and dust heating plays an important role in interpreting potential SFR tracers. In an idealized scenario, a newly formed star is buried inside an axis-symmetric/isotropic molecular cloud. Photons arising from O or B star will ionize their surroundings until all ionizing photons are absorbed, forming a Strömgren sphere. The real picture is more complicated, as the geometry is less isotropic and more complex, allowing some photons to escape the vicinity of the star, and being absorbed or scattered farther away, contributing to the more diffuse starlight. In the second case, farther away from the stellar clusters (OB associations), less energetic diffuse interstellar radiation field is made from the light of many stars.

The interstellar radiation field (ISRF) plays an extremely important role in setting the ISM phase structure (e.g. chemical state depends on photoionization and photodissociation rates), thermal state of the gas (depends on heating via photoionization and photoelectric effect from dust grains), and thermal state of the dust (depends on the absorption of the stellar photons by grains). In strong radiation fields, radiation pressure can also have a dynamical effect on the ISM – by accelerating dust and gas.

1.4.1 INTERSTELLAR RADIATION FIELD IN THEORY

The intensity and spectral shape of the interstellar radiation field depends on a combination of factors, including the initial mass function (IMF), star formation history (SFH) and stellar UV luminosity (dependent on stellar age and metallicity). In order to study the interstellar radiation field (ISRF), we need to review our current knowledge about the key factors that shape it.

One of the most important factors is the initial mass function, which is an empirical law telling us (statistically) about the number distribution of initial masses of newly formed stars, i.e. in a star cluster. Following Scalo (1998) the slope of the IMF power-law can be written as

$$\Gamma = \frac{d \log F(\log m)}{d \log m} \quad (1.4)$$

The ‘universal’ slope of the high-mass IMF is still debated, but typically used values are $\Gamma = 1.35$ (Salpeter 1955) or $\Gamma = 1.3$ (Kroupa 2001). Recent work by the PHAT collaboration Weisz et al. (in prep.), studied the high-mass IMF in M 31 in a systematic way, based on the largest sample of 85 resolved young stellar clusters (4–25 Myr), and measured $\Gamma = 1.46$ with a small intrinsic dispersion 0.1, for stars $\gtrsim 2M_{\odot}$.

From the form of the IMF we know that statistically there are fewer massive stars formed than low mass stars (equivalently, massive stars are formed sparsely). Now, we need to

consider the consequences of drawing a star from the IMF of an initial mass M_{ini} . The birth mass is the primary factor determining the evolution and the lifetime of the star, i.e. an O-star has a short life of $\sim 10^7$ yr comparing to B-star $\sim 10^8$ yr. The other important consequence is the stellar spectrum, i.e. the more massive star is, the harder and more luminous the spectrum. This matters because it sets the amount of photons with capabilities to ionize (> 13.6 eV), photoeject electrons from dust grains that can heat the gas (6–13.6 eV), and heat dust (< 13.6 eV), which is extremely important in setting up the structure of ISM phases. Another important factor that influence the overall shape of the ISRF is metallicity. Metal-poor stars have an intrinsically harder spectra, due to the relatively weaker metal absorption features (Leitherer et al. 2001).

Finally, we are interested in detail how spatial variation of ISRF is dependent upon local conditions, i.e. density of the ISM sets the mean free path of photons (ionizing, dissociating, etc.). Due to cluster dissolution/migration of the stars, current spatial distribution of stars that we measure is likely different from when they were formed, therefore the SFH on small scales might be have larger uncertainties.

1.4.2 ISRF IN OBSERVATIONS

Galactic studies Until recently, the ISRF could be directly determined only locally, in the Solar neighborhood (see Figure 1.9). The ISRF was observed across a wide range

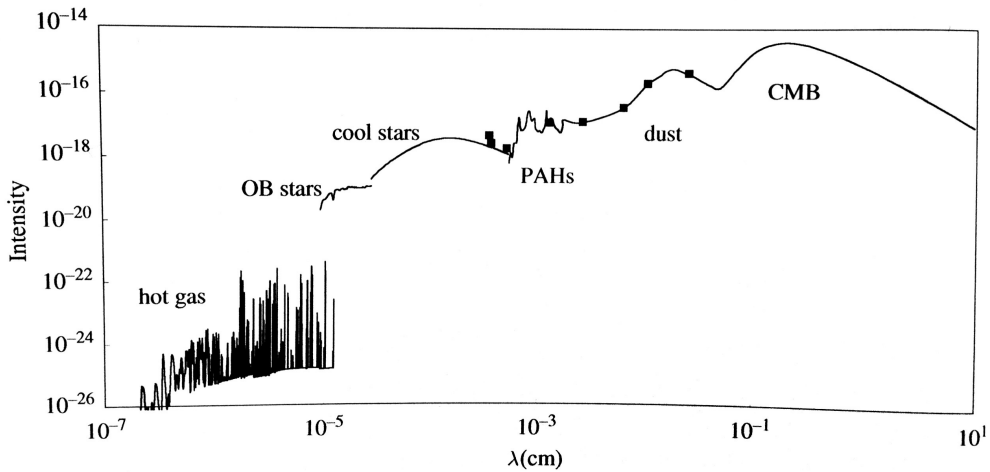


FIGURE 1.9: *Spectral energy distribution (SED) of the interstellar radiation field in the Solar neighborhood. From the shortest wavelengths emission from various sources is indicated: the hot gas, young massive stars, old stars, PAH, dust and cosmic microwave background (CMB). Note, the mean intensity is in units of $\text{ergs}^{-1}\text{cm}^{-2}\text{Hz}^{-1}$, therefore it is not straight forward for the reader to read from this plot the total energy in each term. [Figure adapted from Tielens (2005)]*

of wavelengths, and six dominant components were be identified: X-ray emission from

hot plasma (gas at $\sim 10^5$ – 10^8 K), FUV through optical and near-IR starlight from young and old stars, reemitted by dust mid- to far-infrared emission from absorbed starlight, cosmic microwave background (CMB) emission, synchrotron radiation from relativistic electrons in radio, and free-free emission and recombination continuum² (extends from very low frequencies, radio, up to the frequencies comparable to thermal energy kT , which can be very high considering plasma at the temperature $\sim 10^4$ K).

In the literature, we find several approaches to the topic of the ISRF. One approach is to build a direct model of the ISRF by summing up spectra of the known stars and OB associations and accounting for the effects of dust (distribution, absorption, scattering). It requires the inclusion of as many observables as possible, i.e. stellar catalogs, stellar luminosities. Previously, it was possible only in the solar neighborhood. Habing (1968) derived the average interstellar FUV radiation density G_0 ($6 - 13.6eV$) = 5.29×10^{-14} erg cm⁻³. For a case with large extinction and large albedo, he calculated that $\sim 70\%$ of the average radiation density originates in stars within 200 pc. He found also that at 1000 Å O-stars contribute 35%, B0-B3 – 60% and B4-B9 – 5% to the ISRF. Note, that a possible incompleteness of the stellar catalog of stars of earlier types than B9 was ignored.

In another approach, Mathis et al. (1983) take into account the observed integrated stellar spectrum in the solar vicinity, and fit four components of stars of various temperatures (approximated by black bodies). They build a model assuming dust opacity law matching the observations, and they find $\sim 25\%$ of the total stellar emission in the Galaxy to be absorbed by dust grains and reemitted in the far infrared (FIR). Their ISRF estimate in the solar vicinity is 1.14 of G_0 .

Finally, Parravano et al. (2003) modeled the time dependence of the ISFR by generating random realizations of the solar neighborhood, adopting the distribution of birthrates of OB associations in the MW from McKee & Williams (1997), and assumed general properties (IMF, UV luminosities and main sequence (MS) stars lifetimes, SFRs, etc.), with assumed dust distribution, to model time dependence of the ISRF. From this modelling, they found a time-average ISRF density of 1.6 G_0 in the Solar neighborhood. From the observations they inferred that less than 10% of the total UV field arises from diffuse scattered light, while from the modelling they determined a mean value $\sim 18\%$. Half of the FUV radiation is produced by stars more massive than $18 M_\odot$, but half of escaping from H II regions radiation arises from stars more massive than $13 M_\odot$ (due to correlation of massive stars and dense ISM). In the H_2 band (photodissociation radiation; 912–1100 Å), 85% of total emission is produced by stars with masses greater than $9 M_\odot$. Only associations closer than 500 pc contribute significantly to the energy density at a given point. Half of the radiation comes from sources closer than ~ 85 pc.

Extragalactic studies In more distant galaxies indirect methods are often applied. Inferring ISRF from IR dust emission is one established technique. At a basic level, this uses the energy balance of dust grains to infer the intensity of the radiation field – the

²recombination emission is a free-bound transition from a free electron state to a bound energy level with emission of photon

temperature of the grains is related to the radiation field strength when the grains are in equilibrium (see equation in Section 1.3). The only drawback is that dust can be heated by any UV-optical photons, therefore model returns the average starlight intensity, and it is impossible to retrieve the exact shape of the stellar spectrum nor to know which stellar populations contributed to dust heating.

Many papers have used the dust emission to infer radiation field strength in M 31, most recently Draine et al. (2014). Those authors modeled infrared photometry from *Spitzer* and *Herschel* pixel-by-pixel at ~ 100 pc resolution in M 31. The outcome of the modelling are maps of starlight heating intensity, dust surface density, dust-to-gas ratio and fraction of the dust mass that is in PAHs.

With the advent of the high spatial photometry from the *Hubble* Space Telescope, the ISRF can also be directly measured in extragalactic studies, as it has been done in the solar neighborhood – by adding the contributions of individual stars. The Panchromatic Hubble Andromeda Treasury survey (PHAT; Dalcanton et al. 2012), has obtained HST near-UV to near-IR photometry of around billion stars across $\sim 1/3$ of M 31, enabling a direct determination of the ISRF in our nearby neighbor, as described in Chapter 4 of this thesis.

The very broad picture of the ISRF is that young, massive stars produce majority of FUV photons, A-type stars dominate in the optical wavelengths, while old stars have significant input between far-red (in visual) and NIR. We aim to precisely infer the fractional contributions of energy to the ISM in the defined energy bins (i.e. FUV) from selected stellar populations (i.e. O-stars, B-stars, A-stars, etc.). Details of this work can be found in Chapter 4.

1.5 OUTLINE

In this thesis we examine in detail the physical processes of heating input through the ISRF, absorption and energy transfer through dust, and cooling of the ISM through the emission of [C II] in the Andromeda galaxy. We do this to provide insight into the energy balance of the ISM in galaxies like those that should dominate the SFR density in the local Universe.

The main questions about the ISM energy balance that remain unanswered are: What are the origins of the [C II] emission line? Can [C II] be used as a SFR tracer? In which cases and on what scales? How well is total infrared emission (TIR) tracing SFR? Which stellar populations are heating the ISM? Is there a radial trend? How far from SF regions FUV photons are propagating into the ISM before getting absorbed/scattered? We will address them throughout this thesis.

In Chapter 2 we investigate the origins of [C II] emission – the dominant cooling line of the neutral ISM. We examine high spatial resolution observations of [C II] in the disk

of M 31, with the Survey of Lines in M 31 (SLIM). We present observations of five $\sim 700 \times 700$ pc ($3' \times 3'$) Fields mapping the [C II] emission, H α emission, combined with ancillary infrared (IR) data. The core of the analysis is that we spatially separate star-forming regions from diffuse gas and dust emission on ~ 50 pc scales, to learn about the concentration of the ISM tracers. We study [C II] correlation with SFR, and [C II]/TIR deficit on both small ~ 50 pc and integrated over whole Fields (~ 700 pc) scales.

In Chapter 3 we investigate the [C II] emission arising from the bulge of M 31, where no ongoing star-formation can be found to power gas heating. The dust heating in the bulge of M 31 is dominated by old stellar populations (Groves et al. 2012; Draine et al. 2014). No OB stars have been detected in this region (Brown et al. 1998; Rosenfield et al. 2012) and there is not enough dust obscuration to hide young stars (Melchior et al. 2000). These few Gyr old stars are responsible for heating dust up to ~ 35 K with predominantly optical/near-IR photons, while the mean dust temperature in the disk is only ~ 18 K. Yet, Mochizuki (2000) detected [C II] emission line using ISO in several low resolution pointings (FWHM $\sim 68''$, ~ 260 pc), across and beyond the bulge along M 31's major axis. Although we observe UV emission with Galex (Thilker et al. 2005), it requires the photoelectric heating efficiency above 1% to explain [C II] emission. We investigate other potential sources of ISM heating, and attempt to understand what is powering the observed [C II] emission in the bulge by estimating energy reservoirs/capabilities of these sources. We compare [C II] emission in the bulge to the star-forming regions in the disk, and we discuss the implications of this study for our understanding of energy balance and for [C II] as a SFR tracer (particularly for resolved studies of galaxies), and for integrated measurements.

In Chapter 4 we describe a method to use resolved stellar photometry from the PHAT survey to measure the ISRF across M 31. The final sample consists of about 10^8 spectral energy distributions (SEDs) of individual stars down to $\sim A_0$. By fitting these SEDs we can disentangle the effects of reddening and the intrinsic stellar properties. Currently presented results in Chapter 4 are based on the pilot version of the output from the preliminary probabilistic SED fitting technique. In the near future, we plan to apply this technique to the more advanced Bayesian Extinction And Stellar Tool (BEAST; Gordon et al. in prep.) catalogs for the full PHAT survey. With the technique we describe we can directly study contributions of various stellar populations to the ISM heating. Additionally, we exploit the ancillary data already introduced above by comparing them to the directly inferred SFRs from PHAT, to verify popular SFR tracers like [C II] or H α (combined with $24 \mu\text{m}$ emission; Calzetti et al. 2007).

CHAPTER 2

THE SURVEY OF LINES IN M 31 (SLIM): INVESTIGATING THE ORIGINS OF [C II] EMISSION

2.1 INTRODUCTION¹

[C II] 158 μm is one of the strongest emission lines observed in star-forming galaxies and is the dominant coolant of the neutral interstellar medium (Luhman et al. 1998). Its strength is due to the relatively high abundance of singly-ionized carbon in the interstellar medium (ISM) and the wide range of physical conditions (densities and temperatures) in which the fine-structure transition can be collisionally excited (for a review, see Goldsmith et al. 2012). Due to its strength and long wavelength, the [C II] line is relatively easy to observe even at high redshifts with sub-mm telescopes, such as ALMA (Carilli & Walter 2013). It can potentially be used to estimate the star formation rate (SFR) and, with additional information from other emission lines, to probe some of the physical conditions of the ISM.

Many recent studies attempted to empirically calibrate the relation between [C II] and SFR, both on global and kpc scales. They all find approximately linear relationships between [C II] and SFR with small scatter (see e.g., de Looze et al. 2011; De Looze et al.

¹This Chapter has been published as Kapala et al. (2015)

2014; Herrera-Camus et al. 2015). The physical basis for this relation relies upon [C II] being the dominant coolant of the neutral ISM heated by the UV photons from young stars, via the photoelectric process on dust grains (Tielens & Hollenbach 1985; Wolfire et al. 1995).

One issue with the interpretation of the [C II]–SFR relation, is that the [C II] 158 μm emission line arises from multiple ISM phases. The ionization potential of carbon (11.26 eV) is less than that of hydrogen (13.6 eV), such that C^+ is also present in the neutral ISM, where the [C II] line is typically excited via collisions with atomic hydrogen. At the other extreme, the ionization potential of C^+ is sufficiently high (24.4 eV) that the ion is also found in the ionized ISM, where collisions with electrons dominate the line excitation. In addition, the C^+ species can also be found in molecular gas before the atom combines to C I and CO (Wolfire et al. 2010). In each phase, the [C II] line has a different sensitivity to the gas density (i.e. different critical densities), and different relation with the heating radiation, and hence SFR.

Not only do the energetics of [C II] vary with ISM phase, but the timescale over which it measures SFR varies as well. In the ionized ISM, heating is by the photoionization of hydrogen caused by the extreme UV photons ($> 13.6 \text{ eV}$) from O-stars, and thus [C II] measures the SFR on timescales shorter than 10 Myrs. In the neutral ISM, the photoelectric effect on dust that dominates the heating requires only far UV photons ($\gtrsim 6 \text{ eV}$). These photons are also emitted by B-stars and thus [C II] measures the SFR on much longer timescales. Therefore the phase of the ISM from which the [C II] line arises from plays a vital role in the relation between the SFR and [C II].

Various studies have addressed the origins of [C II] emission. Croxall et al. (2012) presented a pilot study on NGC 1097 and NGC 4559 – two galaxies from the KINGFISH sample (a *Herschel* Key program of 61 nearby $\lesssim 30 \text{ Mpc}$ galaxies; Kennicutt et al. 2011). They corrected for the [C II] emission from the ionized phase by using the [N II] 205 μm and 122 μm lines that arise only from ionized gas (as the ionization potential of nitrogen is 14.53 eV). They found that the fraction of [C II] emission coming from photodissociation regions (PDRs) in these galaxies ranges from 0.35 up to 0.8 for regions with warm dust, depending on the assumed electron density. Also using the [N II] lines, Cormier et al. (2012) found for the starburst galaxy Haro 11 that $\sim 40\%$ of [C II] emission arises from a diffuse low-ionization gas phase, $\sim 20\%$ from a diffuse neutral phase, and associated the remaining $\sim 40\%$ of emission with PDRs. In their observations of M 51, Parkin et al. (2013) found a similar range of the ionized gas fractions of [C II], with values of 0.8, 0.7, 0.5 and 0.5 (with a typical uncertainty ~ 0.2), for the nucleus, center, arm and interarm regions of the galaxy, respectively, based on the [N II] 122 μm and 205 μm line observations. Thus observational studies to date suggest $\sim 50\%$ of the [C II] line may arise from an ionized gas phase, which agrees with theoretical predictions of 10–50% from Abel (2006).

Even if the line arises purely from the neutral ISM, there are further complications in relating [C II] intensity to SFR. First, depending on the density and temperature of the gas, cooling via other emission lines can become more efficient than via [C II] and dominate

overall gas cooling (e.g. [O I] 63 μm ; Tielens & Hollenbach 1985). Second, the [C II] line may suffer from optical depth effects in dense gas (Graf et al. 2012). Finally, and most importantly, the efficiency with which UV photons heat the gas by the photoelectric heating effect can vary. The variations might occur due to changes in the dust properties, resulting in variable gas heating for a given UV field, or due to change in hardness of the spectrum, resulting in varying heating efficiency for a given dust volume. Thus, to properly calibrate the relation between [C II] and SFR, the origins of the [C II] line in galaxies must be understood.

Given the observed close relation of the [C II] line with the UV radiation field, it was also expected that the line and far-IR continuum emission should be related. However, in several galaxies a deficit of the line in relation to the FIR was observed towards high FIR luminosities (Malhotra et al. 2001; Helou et al. 2001). This observed FIR line deficit is thought to be associated with a decrease in the efficiency of the photoelectric heating of the gas in FIR luminous objects, caused by changes in the dust grain properties (see Luhman et al. 2003, for a detailed description). Based on over 240 luminous infrared galaxies (LIRGs), Díaz-Santos et al. (2013) found that the [C II]/FIR ratio decreased with increasing dust temperature. They suggest that this implies that the [C II] 158 μm luminosity is not a good indicator of the SFR, as it does not scale linearly with the warm dust emission most likely associated with the youngest stars. Graciá-Carpio et al. (2011) showed that not only [C II], but also other far-IR lines (e.g. [O I] 63 and 145 μm , [O III] 88 μm , [N II] 122 μm , from both neutral and ionized phases) exhibit deficits relative to the FIR emission for 44 local starbursts, Seyfert and LIRGs.

Several theories have been proposed to explain the observed FIR line deficit, for example charged grains reducing the photoelectric effect (Malhotra et al. 2001; Croxall et al. 2012), or a reduction in the relative number of polycyclic aromatic hydrocarbons (PAHs) reducing the photoelectric efficiency (Helou et al. 2001), or ionization parameter (Graciá-Carpio et al. 2011). Yet, our understanding of the underlying causes is still incomplete. Even after including both correction for diffuse cool neutral and ionized contributions to line emissions and TIR, PDR models used by Croxall et al. (2012) could not reproduce the observed line deficits in the two studied galaxies. Graciá-Carpio et al. (2011) discuss the importance of the ionization parameter (higher starlight heating rate U can increase FIR and dust temperature relative to emission of lines), but it cannot alone explain the deficit of all observed lines relative to IR continuum. Croxall et al. (2012) argue that dusty H II regions (elevated dust levels in the ionized gas) are not responsible for line deficits, neither is increased gas density.

In contrast to the standard FIR line deficit, Israel et al. (1996) studied bright H II complexes in LMC and found [C II]/FIR to be typically around 1%, considerably higher than found in Galaxy and in most galactic nuclei (i.e. $\sim 0.1 - 1\%$; Stacey et al. 1991, and references therein). Israel et al. (1996) explain these higher [C II]/FIR values as the result of the lower metallicity and lower dust-to-gas ratio in the LMC relative to Galactic regions. Nevertheless, when Rubin et al. (2009) revisited LMC with [C II] observations by Mochizuki et al. (1994) and FIR by Surveying the Agents of a Galaxy's Evolution (SAGE; Meixner et al. 2006; Bernard et al. 2008), they found a flattening of [C II] as a

function of FIR at the FIR high brightness end, a similar trend observed by Stacey et al. (1991).

One obvious route for understanding the multi-phase origins of [C II] is to observe the emission at high spatial resolution to resolve the different phases. This has been the goal of many surveys observing [C II] within the Milky Way, such as COBE FIRAS (Wright et al. 1991; Bennett et al. 1994), FILM (Makiuti et al. 2002) and BICE (Nakagawa et al. 1998). However, these Galactic surveys had to deal with line-of-sight (LOS) confusion along the Galactic disk, making comparisons with stars and other gas tracers difficult. The recent GOT C+ survey (Langer et al. 2010; Pineda et al. 2013; Langer et al. 2014b) with Herschel-HIFI was able to limit this confusion using their high velocity resolution observations. By comparing their resolved [C II] data with similarly spectrally resolved CO and HI data they were able, to compare scale heights measured by [C II], atomic and molecular gas, associate [C II] emission to the spiral arms between 4 and 11 kpc, and estimate CO-dark-H₂ fraction of the total molecular gas. Yet, while their study is extremely powerful with [C II] measured in ~ 500 sight-lines in the Galactic plane, the large angular scale of the Milky Way meant that it is impossible to fully map [C II].

Conversely, in more distant galaxies, multiple ISM phases cannot be separated spatially. Early [C II] observations of nearby galaxies were typically galaxy averages, comparable to what is now being done with high redshift galaxies (Stacey et al. 1991; Malhotra et al. 2001; Walter et al. 2009; Stacey et al. 2010; Graciá-Carpio et al. 2011). Recent nearby galaxy studies are only now reaching kiloparsec resolution (Croxall et al. 2012; Díaz-Santos et al. 2013; Parkin et al. 2013; Herrera-Camus et al. 2015).

The Local Group represents an ideal compromise between high spatial resolution to study the correlation of [C II] with various ISM phases, and the simple LOS and galaxy-scale coverage necessary to address these questions. However, most of the Local Group galaxies are low metallicity objects (dwarf galaxies: Israel et al. 1996; Kim & Reach 2002; Rubin et al. 2009; Israel & Maloney 2011; Leboutteiller et al. 2012), or low-mass (M 33, HerM33es project, Kramer et al. 2010; Braine et al. 2012), which have significantly different ISM characteristics to massive galaxies in which most of the star formation in the Universe occurs at present.

The Andromeda galaxy (M 31) provides an ideal target to explore the origins of [C II] as the only massive, star-forming L_{\star} spiral galaxy in the Local Group. Therefore, as part of a project to understand the heating and cooling of the ISM, we have carried out a *Herschel Space Observatory*² far-IR and ground-based optical integral field emission line survey of M 31 (SLIM; the Survey of lines in M 31). Previous studies of [C II] in M 31 with the *Infrared Space Observatory* targeted the bulge (Mochizuki 2000) and a spiral arm on the minor axis (Rodriguez-Fernandez et al. 2006), respectively with far lower effective spatial resolution.

The proximity of M 31 (~ 780 kpc, Stanek & Garnavich 1998) combined with the *Her-*

²Herschel is an ESA space observatory with science instruments provided by European-led Principal Investigator consortia and with important participation from NASA.

schel resolution of $11''$ at $158\ \mu\text{m}$ (our limiting resolution), enables the study of ISM tracers at sub-kpc scales ($\sim 50\text{ pc}$), allowing us to spatially separate star forming from diffuse regions. The large amount of available ancillary data, and the simplicity provided by an external perspective, make M 31 a unique target for understanding [C II] emission. Our survey targeted several different star forming regions across the disk of M 31, enabling a study of the relative variation of [C II] emission (and heating and cooling of the ISM in general) over a wide scope of physical conditions such as stellar surface densities, SFRs, and metallicities. The only caveat is that due to high inclination of M 31 (70° ; Dalcanton et al. 2012), our data also suffer from some LOS confusion. Nevertheless, our analysis is valid within the known limitations, that [C II] emission line: 1) does not spatially resolve individual H II regions, nor PDRs, 2) is not spectrally resolved ($\sim 200\text{ km/s}$.)

This Chapter is organized as follows: the [C II] and ancillary data acquisition is described in Section 2.2, along with further processing details. In Section 2.3.1, we present the spatial decomposition of several ISM and SFR tracers. In Section 2.3.2 we test the calibration of [C II] to SFR relation at high spatial resolution, and we compare to existing studies on different spatial scales. In Section 2.3.3, we investigate the FIR line deficit and its relation to the ability of [C II] to track SFR. Finally, we discuss our results in Section 2.4, and present our conclusions in Section 2.5.

2.2 DATA

M 31 is the most massive external galaxy in the Local Group. It is a highly inclined (i.e., 70° ; Dalcanton et al. 2012, and references therein) spiral galaxy classified as SA(s)b (see Tab. 2.1) and presents ring-like structure. Due to its proximity ($\sim 780\text{ kpc}$; Stanek & Garnavich 1998), it is possible to reach a high spatial resolution with *Herschel* ($\sim 50\text{ pc}$ at $160\ \mu\text{m}$).

TABLE 2.1: *M 31 information*

Nucleus position ^a (J2000)	$00^{\text{h}}42^{\text{m}}44.^{\text{s}}35$ $+41^\circ 16' 08''.60$
Inclination ^b	70°
Position angle ^b	43.2°
Distance ^c	$780 \pm 40\text{ kpc}$
Morphological type ^a	SA(s)b
SFR ^d	$0.4\text{ M}_\odot/\text{yr}$

^a Based on NED data and references therein

^b Dalcanton et al. (2012)

^c Stanek & Garnavich (1998)

^d Barmby et al. (2006)

The measured SFR in M 31 is low, $\sim 0.4\text{ M}_\odot\text{ yr}^{-1}$, over the last 100 Myr (Barmby et al. 2006), and is concentrated mostly in the spiral arms and rings. In addition, a large diffuse

fraction of H α emission is also observed (Walterbos & Braun 1994; Azimlu et al. 2011).

We carried out a far-IR and optical survey of interstellar emission lines in M 31 (SLIM; the Survey of lines in M 31; PI K. Sandstrom) to study the cooling emission from a variety of ISM phases. The survey consists of five 3'×3' (~700×700 pc) Fields with Herschel PACS spectroscopy and optical integral field spectroscopy. This line survey is complemented with infrared photometry from *Herschel* and *Spitzer*. We describe the data we used in our present analysis in the following subsections.

2.2.1 *Herschel* PACS SPECTROSCOPY

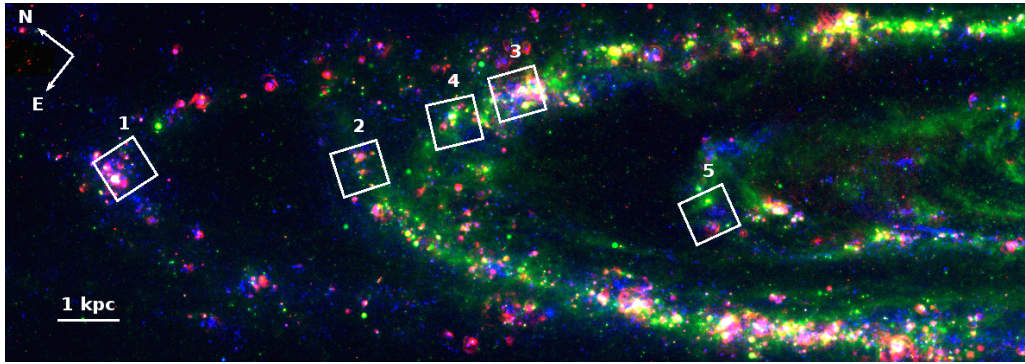


FIGURE 2.1: Position and orientation of the five Fields targeted in this study overlaid on a RGB image (blue - *Galex* FUV, green - *MIPS* 24 μm and red - H α), region numbers are labeled and the orientation is shown in the upper left. A scale bar indicates 1 kpc (4.4').

TABLE 2.2: Coordinates of Field centers

F	R.A. (J2000)	Dec. (J2000)	P.A. [$^{\circ}$]	Observation ^a ID
1	00 ^h 46 ^m 29. ^s 17	+42 $^{\circ}$ 11'30".89	70.7	1342236285
2	00 ^h 45 ^m 34. ^s 79	+41 $^{\circ}$ 58'28".54	55.7	1342238390
3	00 ^h 44 ^m 36. ^s 49	+41 $^{\circ}$ 52'54".21	55.0	1342238391
4	00 ^h 44 ^m 59. ^s 26	+41 $^{\circ}$ 55'10".47	51.0	1342238726
5	00 ^h 44 ^m 28. ^s 76	+41 $^{\circ}$ 36'58".91	63.0	1342237597

^a [C II] & [O I] observations acquired between 28th Feb and 1st Mar, 2012

Observations of the [C II] 158 μm , [O I] 63 μm , and [N II] 122 μm spectral lines were carried out using the unchopped mapping mode on the Photodetector Array Camera and Spectrometer (PACS; Poglitsch et al. 2010) on board of the ESA *Herschel* Space Observatory (Pilbratt et al. 2010) for a total of 47.1 hours of observing time (OT1_ksandstr_1; PI K. Sandstrom). Due to the large angular extent of M 31, galaxy emission fell within all available chopper-throws. Therefore we used the unchopped mode with an off position defined to be well outside of the body of M 31, and visited 3 times during each

AOR. The [C II] 158 μm and [O I] 63 μm lines were mapped in five Fields of 3' by 3' (700 pc \times 700 pc) using rastering in the instrument reference frame with 37''.5 and 23''.5 steps. We choose 3' by 3' Field sizes: (1) to cover the scale over which energy from star-forming regions should be deposited in the ISM and (2) to match the approximate size of a resolution element in the KINGFISH [C II] maps at the sample's average distance of 12 Mpc.

The five Fields probe different physical conditions along M31's major axis, sampling different H α , FUV, and 24 μm surface brightnesses and atomic to molecular gas ratios, while still focusing on regions of active star-formation. The Fields are shown in Figure 2.1 and are tabulated in Table 2.2. All Fields lie on the NE major axis of the galaxy as this side is covered by the Pan-chromatic Hubble Andromeda Treasury program (PHAT; Dalcanton et al. 2012), providing a large, high-resolution, UV to NIR ancillary dataset. We label these Fields F1 (outermost) through F5 (innermost), though we note that this order is not entirely radial as F3 is at a slightly smaller galactocentric radius than F4. F1 covers a star-forming region in the outer spiral arm at ~ 16 kpc, while Fields F2 to F4 fall in the star forming ring at ~ 10 kpc, and F5 covers a region in the inner arm at ~ 7 kpc, from the center of the galaxy, respectively.

The [N II] 122 μm line was observed only in six smaller maps of 1' \times 1' that targeted the brightest H II regions in the [C II] Fields (2 in F1, 1 in F2, 2 in F3 and 1 in F4). Unfortunately, the [N II] line was found to be very weak and was detected only in very few spaxels.

Similarly, though the [O I] line was significantly detected in several regions in all Fields, it was found to be weaker than [C II] in all reliably detected regions, with typical values of [O I]/[C II] ~ 0.46 . We find these reliable detections only in the brightest regions (SF). We expect [O I]/[C II] to be even less in the diffuse regions (see Figure 9.2 in Tielens 2005). In the following, we focus the analysis mostly on the [C II] 158 μm line and leave a discussion of the [O I] and [N II] lines for a future paper (Kapala et al. 2015 in prep).

The [C II] data was reduced using the *Herschel* Interactive Processing Environment (HIPE) version 8.0 (Ott 2010). Reductions applied the standard spectral response functions, flat field corrections, and flagged instrument artifacts and bad pixels (see Poglitsch et al. 2010). The dark current, determined from each individual observation, was subtracted during processing because it was not removed via chopping. Transient removal was performed using the surrounding continuum, as described in Croxall et al. (2012). In-flight flux calibrations were applied to the data. After drizzling in the HIPE pipeline, the [C II] 158 μm (FWHM $\sim 11''.0$) line was integrated in velocity to produce maps with 2''.6 pixels. For the analysis, we rebinned the maps to have approximately half-beam spaced pixel size (5''.2). The final integrated intensity maps of the [C II] 158 μm emission line for each Field are shown in the right side in Figures 2.2 and 2.3.

The details of the observations; coordinates, AOR numbers, are listed in Table 2.2. The mean 1- σ [C II] surface brightness sensitivity of the line integrated intensity in all pixels in the overlapping regions of the [C II] and H α Fields is 1.46×10^{38} erg s $^{-1}$ kpc $^{-2}$ with

standard deviation $5.51 \times 10^{37} \text{ erg s}^{-1} \text{ kpc}^{-2}$. Note that individual points might have values below that average limit. That is because for an application of the significance cuts in Section 2.3, we use each pixel's $1\text{-}\sigma$ noise measured from its spectrum, which accounts for the goodness of the line fit and PACS scanning flaws, not only instrumental sensitivity limit. The absolute [C II] flux calibration uncertainty is $\sim 30\%$ ³. We visually inspected the spectral cubes in low S/N regions and find that the quoted uncertainties on the line flux are reasonable.

2.2.2 PPAK IFS

We obtained optical integral field spectroscopy (IFS) covering the same five Fields as the PACS spectral maps (PI K. Sandstrom), over nine nights in September 2011 using the Calar Alto 3.5m telescope with the PMAS instrument in PPAK mode with the V300 grating (Roth et al. 2005; Kelz et al. 2006). This setup provides 331 science fibers, each $2''.68$ in diameter, that sample a spectral range from $3700\text{--}7000 \text{ \AA}$ with $\sim 200 \text{ km s}^{-1}$ instrumental resolution and hexagonally tile a $\sim 1'$ field of view. Our observation and reduction procedures follow very closely those outlined in Kreckel et al. (2013), and we summarize here only the key steps and variations from that description.

Each of the five Fields were mosaicked with 10 PPAK pointings. To completely recover the flux and fill in gaps between the fibers, each pointing was observed in three dither positions. We reduced these nearly 50,000 spectra using the p3d software package (Sandin et al. 2010). All frames are bias subtracted, flat-field corrected and wavelength calibrated using standard calibration observations. Frames are cleaned of cosmic rays using the L. A Cosmic technique (van Dokkum 2001) as adapted within p3d. Spectra are extracted using a modified optimal extraction method that simultaneously fits all line profiles with a Gaussian function (Horne 1986). Relative flux calibration is applied using one of two standard stars observed during the night, where we choose the star that appears most centered within a single fiber. As M 31 is quite extended on the sky, separate sky pointings were obtained and a best fit linear combination from the set of sky pointings observed that night are used to optimally subtract the sky emission from the science spectra.

Seeing was sub-fiber ($<3''$) and astrometry for each mosaic position has been applied through comparison by eye of features in our $H\alpha$ maps with Local Group Galaxies Survey $H\alpha$ images (Azimlu et al. 2011). From comparison of stellar sources within the PPAK data and SDSS (Aihara et al. 2011) broadband images we estimate our astrometry is accurate to within $1''$, sufficient for comparison with the lower resolution PACS images. All observations were taken at airmass below 2, with nearly all below 1.5, so we neglect the effects of differential atmospheric refraction. Conditions were not consistently photometric, so we have re-calibrated the flux scaling of each dither position and scaled it to the continuum subtracted Local Group Galaxies Survey $H\alpha$ images (Azimlu

³http://herschel.esac.esa.int/twiki/pub/Public/PacsCalibrationWeb/PacsSpectroscopyPerformanceAndCalibration_v2.4.pdf

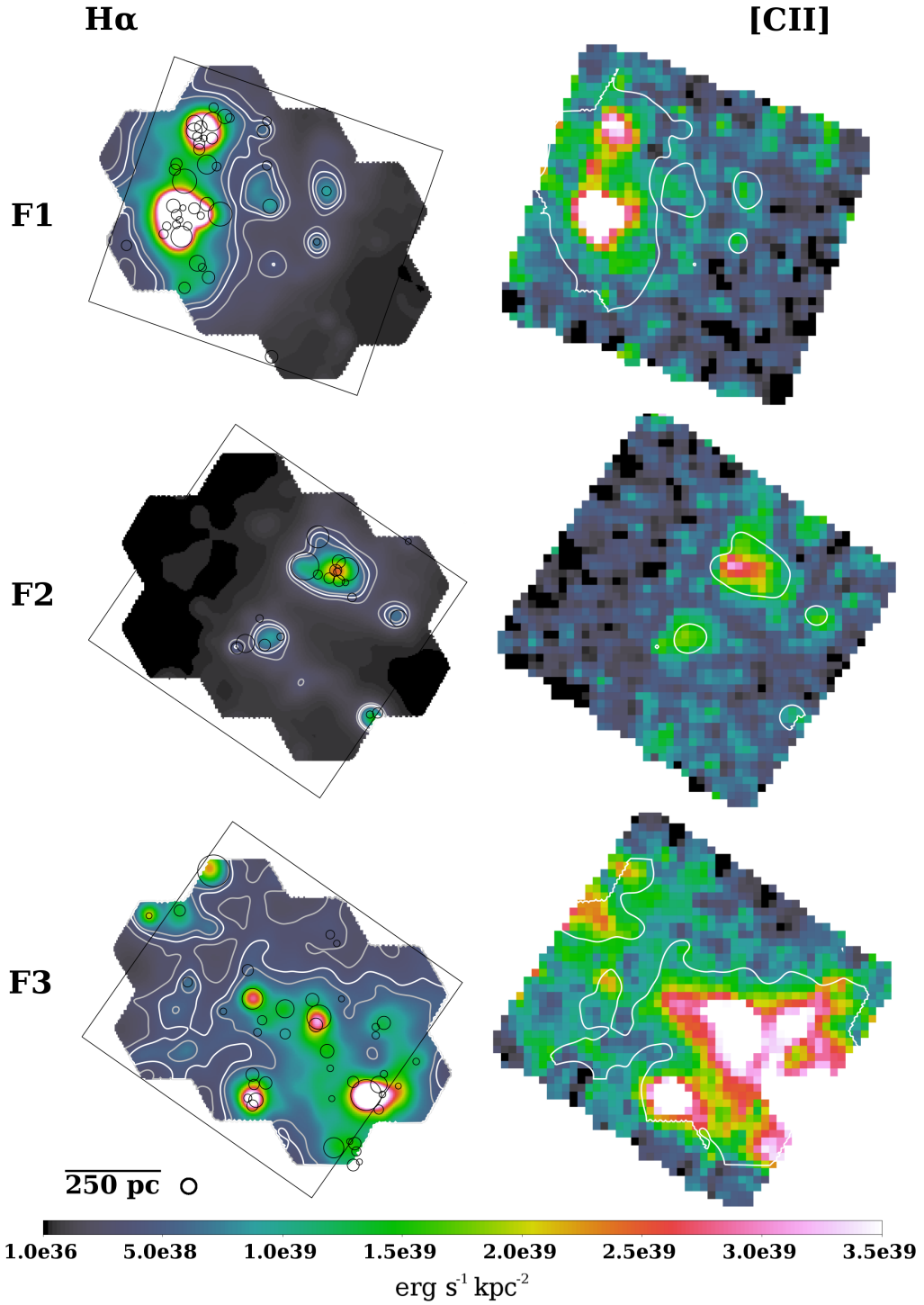


FIGURE 2.2: **Left column:** $H\alpha$ emission from SF regions in Fields 1 to 3, convolved to match $[C II]$ resolution. Black circles indicate the $H II$ regions defined in the Azimlu et al. (2011) catalog, with the radius of the circles set to the FWHM of the $H II$ regions. White contour level indicates chosen level L_0 that delineates SF regions, two gray ones are $L_0 \pm 30\% L_0$. Black boxes show $[C II]$ pointings. The $[C II]$ beam size ($11.0''$) and scale bar ($66.1''$) are indicated in the bottom left corner. **Right column:** Herschel PACS $[C II]$ $158 \mu\text{m}$ maps of Fields 1 to 3 with L_0 $H\alpha$ contour overlaid. All maps have a common linear color scale given at the bottom of the Figure. Note that only pixels present in both $[C II]$ and $H\alpha$ maps are used in our analysis.

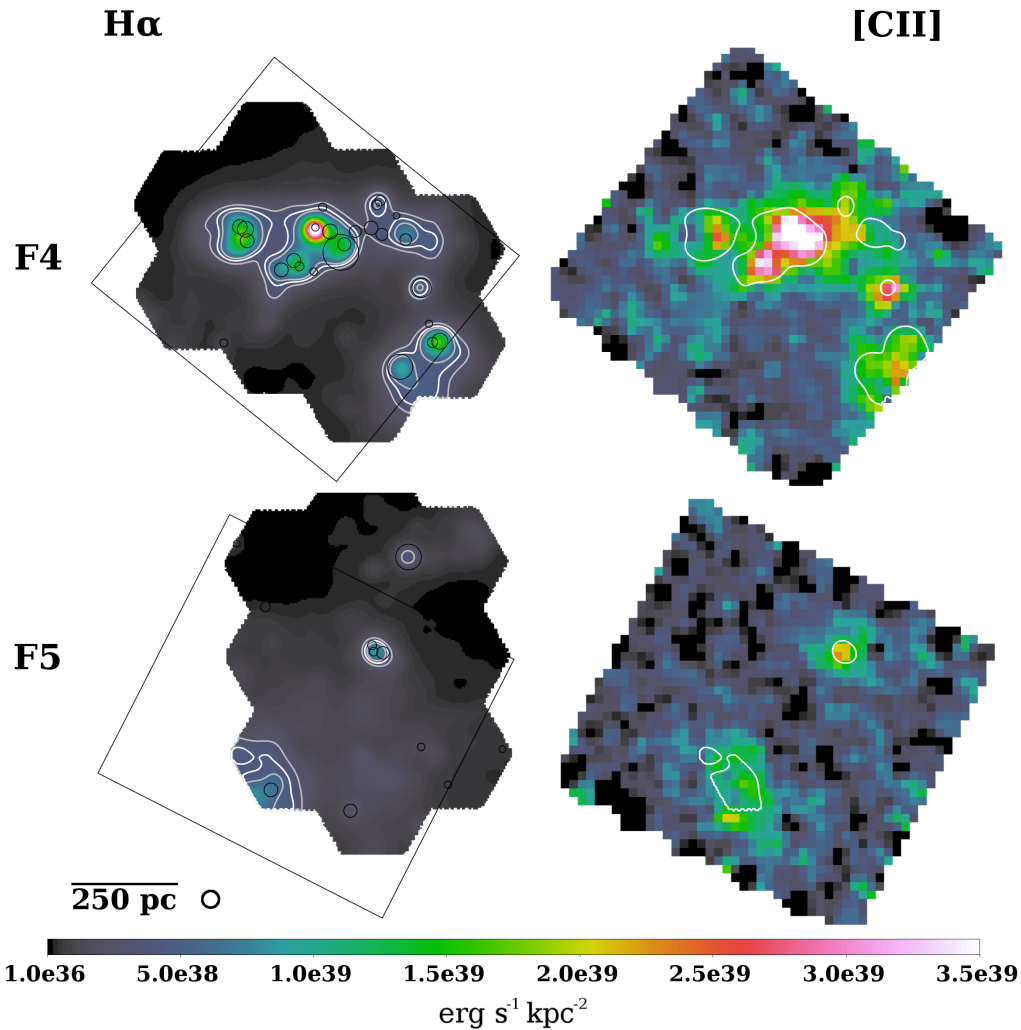


FIGURE 2.3: Same as Figure 2.2 for Fields 4 and 5.

et al. 2011). We expect our relative flux calibration to be accurate to within 5%, however, we allow for a larger systematic uncertainty of 20%.

The H α line was measured in each spectrum using the GANDALF package (Sarzi et al. 2006), which employs penalized pixel fitting (pPXF; Cappellari & Emsellem 2004) to simultaneously fit both stellar continuum templates and gaussian emission line profiles. This allows us to deblend the contribution of [N II] from the H α emission line, as well as to correct for underlying stellar absorption. We use here simple stellar population (SSP) template spectra from the Tremonti et al. (2004) library of Bruzual & Charlot (2003) templates for a range of 10 ages (5 Myr - 11 Gyr) and two metallicities (1/5 and 1 solar), though using stellar templates selected from the MILES library (Falc3n-Barroso et al. 2011) does not significantly change our measured line fluxes. These H α line fluxes are interpolated onto a regular grid using Delaunay linear triangulation, re-

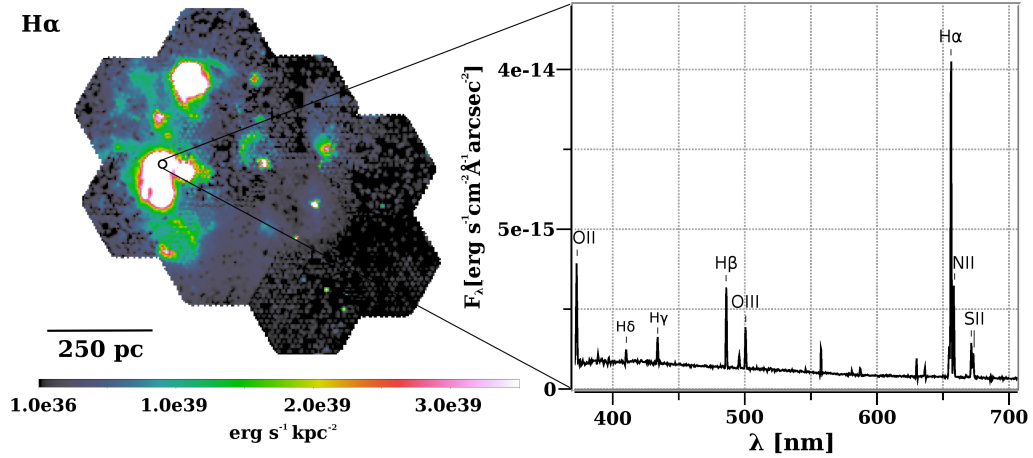


FIGURE 2.4: PPAK IFS data in Field 1. Left panel - $H\alpha$ map at the native resolution, right panel - spectrum in the pixel marked as black circle ($RA(J2000) = 00^h46^m34.^s52$, $Dec.(J2000) = +42^\circ11'43''.82$).

sulting in images with $\sim 2''.5$ resolution that reach 3σ $H\alpha$ surface brightness sensitivities of $2 \times 10^{-16} \text{ erg s}^{-1} \text{ cm}^{-2} \text{ arcsec}^{-2}$. As in the case of $[C\text{II}]$ data, one of the product of the reduction pipeline is noise map. The $H\alpha$ noise depends not only on the line strength, but also on the observing conditions. Due to atmospheric variations, we compare the values between the individual pointings. This approach returns median noise $3.60 \times 10^{37} \text{ erg s}^{-1} \text{ kpc}^{-2}$ and standard deviation $3.15 \times 10^{37} \text{ erg s}^{-1} \text{ kpc}^{-2}$. Figure 2.4 shows the map for Field 1, as well as an extracted spectrum.

2.2.3 Spitzer & Herschel PHOTOMETRY

We make use of the data from several infrared surveys of M31 using *Herschel* and *Spitzer*. M31 was observed with the Multiband Imaging Photometer (MIPS; Rieke et al. 2004) on board of the *Spitzer* Space Telescope (Werner et al. 2004) by Gordon et al. (2006) and the InfraRed Array Camera (IRAC; Fazio et al. 2004) by Barmby et al. (2006). In addition, M31 was observed by the *Herschel* Space Observatory (PI O. Krause) using the PACS and SPIRE instruments (Griffin et al. 2010, Spectral and Photometric Imaging Receiver). For details of the PACS and SPIRE observations and processing see Groves et al. (2012) or Draine et al. (2014).

PACS images in all photometric bands (70, 100 and $160 \mu\text{m}$) were obtained in slow parallel mode, with a final image size of $\sim 3^\circ \times 1^\circ$ aligned with the position angle of M31's major axis. This covers M31's full disk including the 16 kpc ring. All images were reduced to level one using HIPE v6.0, and then SCANAMORPHOS v12.0 (Roussel 2012) was used to produce the final product.

The FWHM is $5''.6$ for $70\ \mu\text{m}$, $6''.8$ for PACS $100\ \mu\text{m}$ and $11''.4$ for PACS $160\ \mu\text{m}$. Beam sizes are taken from PACS Observer's Manual⁴ for $20''\text{s}^{-1}$ scans. $1''$ pixel size was used for all PACS bands.

For the Spitzer bands we considered, the IRAC $8\ \mu\text{m}$ has a FWHM= $2''.0$ and the MIPS $24\ \mu\text{m}$ has a FWHM= $6''.5$.

To remove the foreground emission from the Milky Way and any other foregrounds or backgrounds, we measured the median surface brightness in regions on the edges of the map, away from the main body of M 31. These values showed no clear gradient, so a uniform background was subtracted from each image. The determined backgrounds were: $2.40\ \text{MJy sr}^{-1}$ ($8\ \mu\text{m}$), $-0.0043\ \text{MJy sr}^{-1}$ ($24\ \mu\text{m}$), $3.17\ \text{MJy sr}^{-1}$ ($70\ \mu\text{m}$), $3.23\ \text{MJy sr}^{-1}$ ($100\ \mu\text{m}$) and $2.29\ \text{MJy sr}^{-1}$ ($160\ \mu\text{m}$).

2.2.4 FURTHER PROCESSING

All maps were convolved to match the PACS $160\ \mu\text{m}$ resolution of $11''.0$, using the Astropy Collaboration et al. (2013) package `convolve_fft` and kernels from Aniano et al. (2011) for each specific filter: IRAC $8\ \mu\text{m}$, MIPS $24\ \mu\text{m}$, PACS $70\ \mu\text{m}$, PACS $100\ \mu\text{m}$, and PACS $160\ \mu\text{m}$. The latter kernel was also used for the [C II] map. For the $\text{H}\alpha$ images we assumed an intrinsic Gaussian PSF with a FWHM of $2''.5$ (see Kreckel et al. 2013), and used the corresponding convolution kernel. The convolved maps were all resampled to match the [C II] pixel size of $5''.2$ using the `Montage` (Jacob et al. 2010) Python wrapper⁵. For any direct comparison, the units of the images were converted to $\text{erg s}^{-1}\ \text{cm}^{-2}\ \text{sr}^{-1}$ or $\text{erg s}^{-1}\ \text{kpc}^{-2}$.

2.2.5 DERIVED QUANTITIES

We use the Calzetti et al. (2007) formula to calculate SFR surface density from a linear combination of $\text{H}\alpha$ and $24\ \mu\text{m}$ emission, which includes a correction for absorbed emission that is important when young stars are embedded in their natal clouds. At the physical resolution we reached in this work, we begin to resolve out the H II regions and diffuse gas, such that any SFR calibration based on linear combination of star-forming tracers no longer strictly holds (Leroy et al. 2012; Simones et al. 2014). Furthermore, SFR measurements at $50\ \text{pc}$ scales are problematic using indirect tracers like $\text{H}\alpha$ and dust emission for many reasons, including sampling of the stellar population (others include drift of stars between pixels, star formation history, and others outlined in Kennicutt & Evans 2012). For the purposes of our work, we are primarily interested in the relative spatial distribution of these SFR tracers and not an accurate measurement of the $50\ \text{pc}$ scale SFR.

⁴http://herschel.esac.esa.int/Docs/PACS/html/pacs_om.html

⁵<http://www.astropy.org/montage-wrapper>

$$\Sigma_{\text{SFR}} [\text{M}_{\odot}\text{yr}^{-1}\text{kpc}^{-2}] = (634 I_{\text{H}\alpha} + 19.65 I_{24\mu\text{m}}) [\text{erg s}^{-1}\text{cm}^{-2}\text{sr}^{-1}] \quad (2.1)$$

This calibration assumes a constant SFR for 100 Myr, solar metallicity, and the stellar population models and Kroupa initial mass function (IMF) from Starburst99 (2005 update; Leitherer et al. 1999). In reality, the SFR in M 31 has not been constant over the last 100 Myr, with the star formation histories based on Hubble stellar photometry showing significant variation in this timescale, and across the disk in M 31 (?). Nevertheless, as $\text{H}\alpha$ is the dominant contributor to the SFR shown for most of the points in Figure 2.7, therefore the effect of the variation in the star formation history to this calibration is limited. The average SFR surface densities, listed in Table 2.3, range between $2 - 7 \times 10^{-3} \text{ M}_{\odot} \text{ yr}^{-1} \text{ kpc}^{-2}$, the estimated median uncertainty is $4.2 \times 10^{-4} \text{ M}_{\odot} \text{ yr}^{-1} \text{ kpc}^{-2}$ with the standard deviation $3.3 \times 10^{-4} \text{ M}_{\odot} \text{ yr}^{-1} \text{ kpc}^{-2}$.

TABLE 2.3: *The average [C II] emission, Σ_{SFR} and metallicity of the Fields*

Field	R ^a [kpc]	R [°]	[C II] _{TOT} ^b	Σ_{SFR} ^c	[O/H] ^d
1	16.03	1.177	8.26	4.740	0.774
2	12.28	0.902	5.81	1.735	0.943
3	11.31	0.831	17.01	7.136	0.993
4	11.45	0.841	7.93	2.916	0.985
5	6.86	0.504	4.17	1.944	1.361

^a Galactocentric radius

^b Average Field [C II] surf. brightness in [$10^{38} \text{ erg s}^{-1}\text{kpc}^{-2}$]

^c Average Field SFR surface density in [$10^{-3} \text{ M}_{\odot}\text{yr}^{-1}\text{kpc}^{-2}$]

^d Metallicity relative to solar with $\log(\text{O}/\text{H})_{\odot} = -3.31$

The average gas phase metallicity for each Field is calculated from Equation 7 from Draine et al. (2014) and listed below, using the deprojected radial distance of the Field center. The Draine et al. (2014) formula is equivalent to the “direct T_e -based method” to derive metallicity gradient measured by Zurita & Bresolin (2012) in range of radii where both have measurements. Zurita & Bresolin (2012) use auroral optical line’ ratios in H II regions (for $12 + \log(\text{O}/\text{H})_{\odot} = 8.69$), while Draine et al. (2014) use the dust-to-gas ratio as a metallicity proxy:

$$\frac{(\text{O}/\text{H})}{(\text{O}/\text{H})_{\odot}} \approx \begin{cases} 1.8 \exp(-R/19\text{kpc}) & \text{for } R < 8\text{kpc} \\ 3.08 \exp(-R/8.4\text{kpc}) & \text{for } 8 < R < 18\text{kpc}. \end{cases} \quad (2.2)$$

The metallicity ranges from 0.8 to 1.4 Z_{\odot} , and the individual results per Field are listed in Table 2.3.

We calculate the total infrared emission (TIR) using a linear combination of IRAC 8 and 24 μm , PACS 70 and 160 μm (all in units of $\text{erg s}^{-1}\text{cm}^{-2}\text{sr}^{-1}$), as described in Draine & Li (2007):

$$\text{TIR} = 0.95(\nu I_{\nu})_8 + 1.15(\nu I_{\nu})_{24} + (\nu I_{\nu})_{70} + (\nu I_{\nu})_{160}, \quad (2.3)$$

where the worst-case error in estimating TIR is $\sim 30\%$, and dominated by noise and calibration uncertainties of its components. This TIR calibration is identical to what was assumed by Croxall et al. (2012), whose results we compare in Section 2.3.3.2.

2.3 RESULTS

2.3.1 [C II] FROM SF REGIONS

As discussed above, the [C II] emission comes from multiple phases of the ISM, which includes H II regions and their bordering PDRs, as well as the diffuse ISM (cold neutral medium – CNM, warm neutral medium – WNM, and warm ionized medium – WIM). Our [C II] maps have a resolution of ~ 50 pc. Individual H II regions in our Fields have typical sizes of ~ 20 – 30 pc in diameter (Azimlu et al. 2011) and PDRs give an additional ~ 0.3 – 3 pc layer, assuming carbon is ionized up to $A_V \sim 5$ (Tielens 2005) into the PDR for a typical density $n_H \sim 10^3 - 10^4 \text{ cm}^{-3}$. Therefore, H II regions and PDRs are blended together at our working resolution. Hereafter, we refer to these “blended” H II regions and PDRs as star-forming (SF) regions. Although we cannot separate H II regions and PDRs in this study, we can investigate the fraction of [C II] arising from the diffuse ISM versus SF regions. In the following Section, we describe how we delineate SF regions using our H α maps.

2.3.1.1 DELINEATING SF REGIONS

H II regions in M 31 can be identified and resolved (Azimlu et al. 2011) using H α emission. Because of the much lower resolution of the [C II] map, multiple H II regions might reside in a single pixel. Therefore, we use the H II region catalogs as a guide to define contours in H α emission, at a resolution matched to the [C II] maps, that enclose most of the massive star formation. H α emission was previously used to distinguish between H II regions and diffuse media for distinguishing the origin of [C II] in LMC by both Kim & Reach (2002) (following work of Kennicutt & Hodge 1986) with H α contour $5.09 \times 10^{39} \text{ erg s}^{-1} \text{ kpc}^{-2}$, and by Rubin et al. (2009) with $1.20 \times 10^{39} \text{ erg s}^{-1} \text{ kpc}^{-2}$.

H α emission from H II regions in M 31 is relatively modest, compared to other Local Group galaxies. Azimlu et al. (2011) report a total H α luminosity coming from H II regions in M 31 $\sim 1.77 \times 10^{40} \text{ erg s}^{-1}$, which is comparable to the luminosity of the 30 Doradus complex in the LMC alone $\sim 1.5 \times 10^{40} \text{ erg s}^{-1}$ (Kennicutt 1984). On average, Azimlu et al. (2011) deduced a $\sim 63\%$ diffuse ionized gas contribution from spatially separating H II regions from the surrounding emission. Walterbos & Braun (1994) used [S II]/H α ratios to identify diffuse ionized gas and obtained a $\sim 40\%$ contribution.

To start, we convolve our PPAK H α maps to the [C II] resolution. Then, we use the H II

region catalog from the Local Group Survey (LGS; Azimlu et al. 2011) to identify the location and half-light radii of the H II regions. We use the LGS catalog rather than our PPAK maps because of the 2 times higher spatial resolution of their imaging, which allows for better identification of H II regions. Nevertheless, for the remaining analysis, we use our PPAK H α maps rather than the narrowband imaging from LGS for the following reasons: (1) [N II] 6548 and 6583 Å are blended with H α in the narrow band imaging (see Figure 2.4) and variations in the H α /[N II] ratio make correcting for blending difficult and (2) removal of stellar continuum is significantly easier from the PPAK data compared to the narrowband imaging.

We then define a surface brightness threshold in the convolved H α map above which the majority of the H II regions identified by Azimlu et al. (2011) are enclosed. We display the contour at the selected surface brightness threshold, $L_0 = 4.19 \times 10^{38} \text{ erg s}^{-1} \text{ kpc}^{-2}$, in Figures 2.2 and 2.3. Our H α threshold is lower than the values used by Kennicutt & Hodge (1986); Kim & Reach (2002) and Rubin et al. (2009), as we wished to definitively encompass both the H II regions and their associated PDRS in our “SF regions”. Table 2.4 lists the fraction of H II regions enclosed by this contour, along with the areal fraction enclosed, for each Field. In Field 5 several very faint H II regions lie outside the contour, but these regions make a negligible contribution to the overall H α emission. Finally, we use this contour and calculate the fractions of the pixel area within the boundary. “Diffuse” regions are defined as lying outside the H α contour.

TABLE 2.4: Ratios of fraction of emission of the ISM tracers coming from SF regions over total emission per field, for a H α contour $L_0 = 4.19 \times 10^{38} \text{ erg s}^{-1} \text{ kpc}^{-2}$ defining SF region

Field	$\frac{H\alpha_{SF}}{H\alpha_{TOT}}$ [%]	$\frac{[CII]_{SF}}{[CII]_{TOT}}$ [%]	$\frac{M24_{SF}^a}{M24_{TOT}}$ [%]	$\frac{TIR_{SF}}{TIR_{TOT}}$ [%]	$\frac{A_{SF}^b}{A_{TOT}}$ [%]	$\frac{N_{HII}(SF)^c}{N_{TOT}(F)}$
1	82.57	63.04	70.31	34.72	64.41	40/41
2	44.52	20.15	14.40	7.04	13.18	17/20
3	82.35	80.49	79.63	60.02	77.53	39/41
4	56.23	30.97	26.40	13.47	23.07	20/25
5	21.90	12.72	7.85	4.33	6.67	4/11

^a MIPS 24 μm

^b SF region areal fraction of Field

^c The number of H II regions enclosed by SF regions to the total number of H II regions in the Field

We apply the above procedure to calculate the fraction of our tracers (H α , [C II], 24 μm TIR) spatially associated with SF regions. To estimate the uncertainties on this fraction, we moved the contour level by $\pm 30\%$ of the chosen H α surface brightness and recalculate the fractions. We find that $\pm 30\%$ defines a reasonable range of potential contours surrounding the H II regions as can be seen in Figure 2.2. The uncertainty in defining the contour is the dominant component of the total uncertainty on the diffuse fractions since calibration uncertainties divide out and the S/N is high.

We note that the majority of the following analysis compares the relative concentration

of $H\alpha$, [C II], $24\ \mu\text{m}$ and TIR emission in SF regions, rather than focusing on the absolute value of the fraction. For this reason, our results are not sensitive to the exact definition of the contour level, as it mostly represents a fiducial level for comparing the extent of the various SFR tracers. We note that the absolute values of the fractions are sensitive as well to the size of the maps, as diffuse emission might extend beyond the limits of the maps. However, this issue do not detract from our results, because our Field sizes are representative of individual resolution elements in nearby galaxy surveys, therefore can be directly compared.

2.3.1.2 FRACTION OF [C II] AND OTHER TRACERS FROM SF REGIONS

To determine the emission fraction from “SF regions”, $I_{\text{SF}}/I_{\text{TOT}}$, we integrated the emission from each tracer within the contours and divided from the total emission in the map. The total emission only considered the area that had coverage in all relevant maps. In Figure 2.5, we plot these estimates as a function of galactocentric radius.

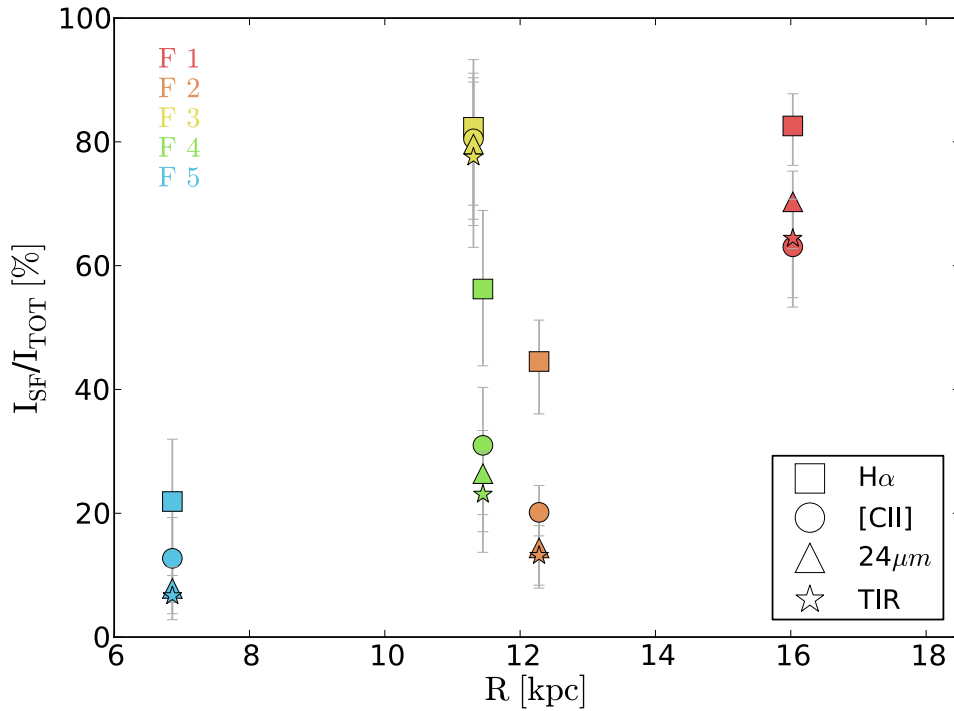


FIGURE 2.5: Emission of $H\alpha$, [C II], $24\ \mu\text{m}$ and TIR from the SF region vs. the total emission in a given Field as a function of galactocentric radius. Error bars translate uncertainties in the $H\alpha$ contour level used to define “SF regions” (see Section 2.3.1.1). Note, that if a 30% higher $H\alpha$ level is picked, points of all tracers for a given Field will systematically shift down to the value indicated by a respective error bar.

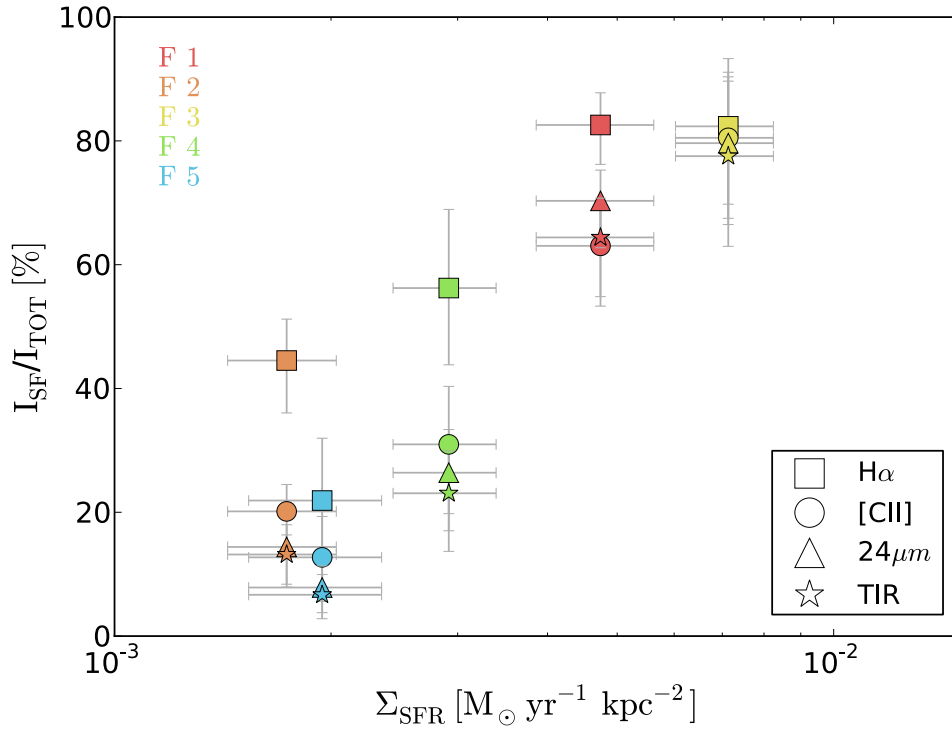


FIGURE 2.6: Same emission fraction as in Figure 2.5, but instead of radial distance, fractions are plotted as a function of star formation rate surface density.

The fractions arising from SF regions varies systematically with the choice of tracer. $\text{H}\alpha$ always has the highest fraction of its emission arising from SF regions, as one might expect due to the regions' definition. The fractions of $\text{H}\alpha$ from SF regions range between ~ 20 – 80% . Previous studies have identified a large component of diffuse $\text{H}\alpha$ emission from M31 ($\sim 63\%$, Azimlu et al. 2011) and we recover a similar value in Field 4. On average our $\text{H}\alpha$ diffuse fraction is lower than 63% , as our Fields are biased to high SFR surface densities by selection.

In general, TIR and $24 \mu\text{m}$ have similar fractions of their emission coming from SF regions, as shown in Figure 2.5. In most of the cases, they also have the lowest SF region fractions compared to the other tracers. The fraction of [C II] from SF regions is intermediate between that of the IR tracers (TIR and $24 \mu\text{m}$) and $\text{H}\alpha$, except in F1. In all of the cases [C II] is closer to the IR than the $\text{H}\alpha$, aside from in F3 where all tracers give approximately the same fractions. It is somewhat surprising that the $24 \mu\text{m}$ emission behaves similarly to TIR, since we expect it to trace warm dust dominantly heated by young stars whereas TIR traces all dust emission. We discuss this finding further in Section 2.4.

In Figure 2.5, we explore the radial trends of the fractions of $\text{H}\alpha$, [C II], TIR and $24 \mu\text{m}$

that arise from SF regions. Given that there are strong radial trends in metallicity, radiation field strength and stellar mass surface density in M 31 we naively expect some trends, however no such radial trends are apparent. Fields 2, 3 and 4 lie at a similar galactocentric radius in the 10 kpc ring, yet they span almost the whole range of SF fraction values. Given this, it is likely that local conditions are dominating the fractional contribution of SF in our Fields. The SFR and ISM surface densities in M 31 do not show radial trends, but rather are dominated by the spiral arm structure and the 10 kpc ring (Draine et al. 2014).

In Figure (2.6), we find a much clearer trend of increasing fraction of $H\alpha$, [C II], $24\ \mu\text{m}$ and TIR from SF regions with increasing Σ_{SFR} , with Fields 2, 3 and 4 following this trend. This demonstrates the dominance of the local conditions to the SF fractions, with the weak trend of SF fractions with radius in Figure 2.5 most likely driven by a combination of SFR, opacity and metallicity.

Even with these trends it is clear that there is always a substantial diffuse component to the [C II] emission in M 31, with even the Field with the highest Σ_{SFR} fraction, Field 3, showing a 20% contribution to [C II] from the diffuse phase.

Based on Figures 2.5 and 2.6, the main result is that [C II] emission is more extended than $H\alpha$, but less extended than TIR and $24\ \mu\text{m}$. We find that the large fractions of diffuse emission arising from outside the SF regions are anti-correlated with Σ_{SFR} . We will discuss possible explanations in Section 2.4, including gas heating generated by a diffuse radiation field and/or leaked photons from SF regions.

2.3.2 THE CORRELATION BETWEEN [C II] AND Σ_{SFR}

Due to its strength and accessibility at high redshifts with new sub-mm telescopes (e.g. ALMA), the correlation between [C II] and SFR has recently been explored in nearby galaxies (within 200 Mpc, e.g. De Looze et al. 2014; Herrera-Camus et al. 2015), to provide a calibration for this line. These studies have found a tight correlation of [C II] surface brightness and Σ_{SFR} on kpc scales. However, from the previous Section it is clear that even at these scales this will include contributions of diffuse emission to both the [C II] line and the Σ_{SFR} measurement.

Using the high spatial resolution available in M 31, we can investigate the correlation both on $\sim 50\ \text{pc}$ scales (our working resolution) and on $\sim 700\ \text{pc}$ scales (i.e. averaged over one full Field, matching the typical resolution of the KINGFISH galaxies in Herrera-Camus et al. 2015). On 50 pc scales we can separate SF regions from diffuse emission as previously described in Section 2.3.1.2. By degrading our resolution to match nearby galaxy studies, we can investigate how the SF and diffuse components participate in creating the observed correlation between [C II] and Σ_{SFR} .

2.3.2.1 THE CORRELATION BETWEEN $[C II]$ AND Σ_{SFR} ON 50 PC SCALES

We first investigate the correlation between $[C II]$ and SFR for individual pixels in each of our Fields. The results are presented in Figure 2.7. Each pixel has a physical scale of ~ 20 pc, meaning that we are slightly oversampling our physical resolution of ~ 50 pc. All pixels have 3σ significance in both the $[C II]$ and Σ_{SFR} measurements. Note that at these physical scales, Σ_{SFR} is not truly indicative of the underlying star formation rate. Rather it represents the average $H\alpha$ + mid-IR flux in each pixel, which could arise from both stellar populations intrinsic to the pixel and photons leaked from stellar populations in nearby regions (Calzetti et al. 2007).

A clear correlation between $[C II]$ and Σ_{SFR} is already visible in each of our Fields, with this supported by the Pearson’s correlation coefficients presented in Table 2.5. To quantify this relation, we use orthogonal distance regression, which allows us to fit a linear function to data points (in logarithmic space) simultaneously accounting for both the x and y errors. Our fits show sublinear to linear relations of $[C II]$ to Σ_{SFR} , with the most linear slope found for F3 which has the highest $\langle \Sigma_{SFR} \rangle$. Details of the fits for all Fields are summarized in Table 2.5, and the best fit linear relation for each Field is overplotted (blue solid line) in Figure 2.7. We have also included in each Field the fit determined by Herrera-Camus et al. (2015) for their integrated sample (dashed red line).

From Figure 2.7 we see that F1 and F2 have the flattest slopes, with both Fields showing an excess of $[C II]$ for the lowest Σ_{SFR} . Note however that at $[C II] \sim 1.76 \times 10^{38} \text{ erg s}^{-1} \text{ kpc}^{-2}$ we hit the 1σ sensitivity limit, and thus this excess may be due to a larger dispersion of $[C II]$ around Σ_{SFR} , rather than a excess due to diffuse $[C II]$ emission. Fields 3, 4 and 5 are consistent with the Herrera-Camus et al. (2015) trend, though F5 probes only a relatively small range in Σ_{SFR} .

The errors of the Herrera-Camus et al. (2015) slope and intercept of the fit, where SFR is based on $H\alpha$ and $24 \mu\text{m}$, are $\beta_{HC} = 0.8970 \pm 0.0078$, $\gamma_{HC} = 41.133 \pm 0.015$ (priv. com.). Our slopes are significantly flatter at a greater than $2\text{-}\sigma$ level, except F3 which is significantly steeper.

In general, the flatter slopes are consistent with the results in the previous Section, as these slopes indicate a greater $[C II]$ fraction at low Σ_{SFR} (and hence low $H\alpha$ surface brightnesses and more “diffuse” regions). However, the flat slopes indicate that, while there is still a correlation between $[C II]$ and Σ_{SFR} , the contribution of diffuse emission means that the calibration determined by De Looze et al. (2014) and Herrera-Camus et al. (2015) do not hold on these scales.

2.3.2.2 $[C II]$ VS Σ_{SFR} ON ~ 700 PC SCALES

To match the physical scales probed in the galaxy sample of Herrera-Camus et al. (2015), we average our data in each Field to obtain the $[C II]$ surface brightness and SFR surface

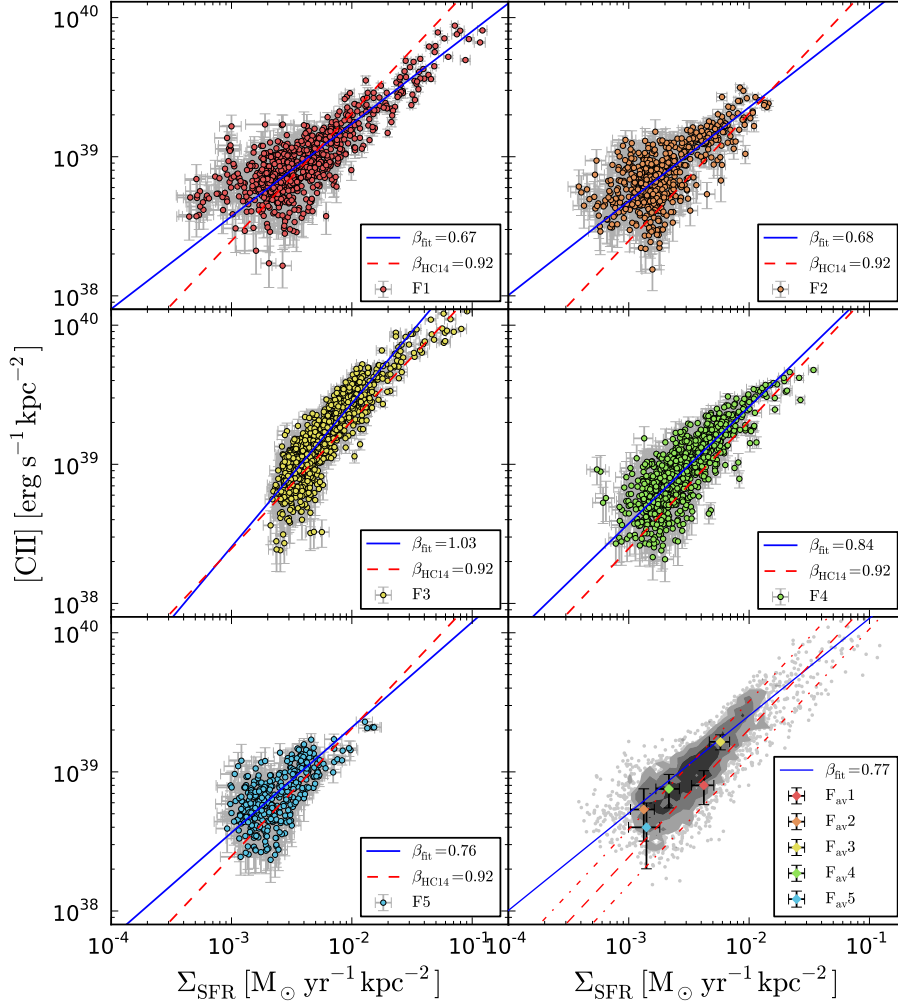


FIGURE 2.7: $[CII]$ and SFR surface densities for individual $5.2''$ pixels (~ 20 pc physical scale) in all Fields. Only pixels with signal/noise per pixel greater than 3 in both measurements are included. Note, that $3\text{-}\sigma$ limit is approximate, because we use noise maps. The solid blue line shows the linear fit (in log space) to the data in each Field. The red dashed line is the relation determined by Herrera-Camus et al. (2015) for the full KINGFISH sample using data of ~ 1 kpc resolution (with $\beta_{HC14} = 0.94$). Lower right panel: This Figure reveals the $[CII]$ and SFR surface density relation from all Fields together (gray density plot and gray dots), as well as the relation averaged over whole Fields (diamonds, ~ 700 pc scales). Note that number density plot, with gray levels 5-10, 10-20, 20-41 per bin size 0.05 dex, does not represent uncertainties. The blue line is the best fit to the individual pixels from all Fields together. The red dashed-dotted lines are 1 sigma scatter around Herrera-Camus et al. (2015)'s fit.

TABLE 2.5: *The average [C II] emission, Σ_{SFR} and metallicity of the Fields*

$$\log_{10}(\Sigma_{[\text{CII}]}) = \beta \log_{10}(\Sigma_{\text{SFR}}) + \gamma$$

Field	Pearson's correlation coefficient r^{a}	β	γ	σ^{b}
1	0.80	0.67 ± 0.010	40.57 ± 0.019	0.17
2	0.68	0.68 ± 0.015	40.71 ± 0.037	0.17
3	0.89	1.03 ± 0.014	41.50 ± 0.031	0.13
4	0.80	0.84 ± 0.016	41.09 ± 0.037	0.15
5	0.64	0.76 ± 0.033	40.83 ± 0.084	0.16
F _{all}	0.82	0.77 ± 0.009	40.84 ± 0.023	0.18

^a $r = 1$ value of the Pearson's correlation coefficient indicates perfect correlation, on the contrary $r = 0$ means no correlation. We found p-values extremely low, demonstrating that the correlation coefficients are significant. We found the highest p-value for F5 ($\sim 10^{-41}$).

^b the dispersion of data points around the fit

density at ~ 700 pc scales. We also attempt to match the removal of the cirrus contribution to SFR as done in Herrera-Camus et al. (2015). The cirrus is the “diffuse” contribution to the total $24 \mu\text{m}$ emission caused by the heating of the dust by the interstellar radiation field arising from older stellar populations not associated with the recent star formation. This cirrus leads to an overestimation of the Σ_{SFR} . Leroy et al. (2012) determined the fraction of cirrus in nearby galaxies on kpc scales, using both physical modeling of the IR spectral energy distribution to determine the local radiation field and maps of the HI to determine the diffuse gas fraction. They found that the cirrus fraction decreases with increasing Σ_{SFR} , and is small above $10^{-2} \text{ M}_{\odot} \text{ yr}^{-1} \text{ kpc}^{-2}$. However, below this value, they found the contribution of the cirrus to $24 \mu\text{m}$ flux could be significant, albeit with a large scatter. As all of points are below this limit, we subtract a constant fraction of $24 \mu\text{m}$ emission, $f_{\text{cir}} = 0.4$, which is the average f_{cir} in the range of Σ_{SFR} that we probe determined by Leroy et al. (2012)⁶. The value we use is higher than the median $f_{\text{cir}} = 0.17$ used by Herrera-Camus et al. (2015), however they probe higher Σ_{SFR} values on average, and we wish to assume a conservative correction here. Our value of f_{cir} is consistent with the high “non-SF” region contribution to the $24 \mu\text{m}$ we find in Figure 2.6. Removal of the cirrus makes the greatest difference to fields with low Σ_{SFR} (Fields 2, 4, and 5; $\sim 26\%$), and smaller differences to the higher Σ_{SFR} fields ($\sim 15\%$ for Fields 1 and 3). Nevertheless, we find that the details of the cirrus removal do not have a large impact on our results described below.

⁶ We do not to remove the cirrus on our smaller 50 pc observations, as we are beginning to resolve out the “diffuse” emission of $24 \mu\text{m}$ on these scales. The cirrus correction of Leroy et al. (2012) was derived on scales of ~ 1 kpc, and cannot be simply applied to these smaller scales. In any case, due to our $3\text{-}\sigma$ cut, H α is the dominant contributor to the SFR we measure for most of the pixels on these scales, such that correcting for the cirrus does not make a significant difference

In the lower right panel of Figure 2.7, we show the average value for each Field overlaid on the grayscale density plot for the individual pixels from all Fields combined. We repeat the orthogonal distance regression on the pixels from all Fields and have overplotted the fit (solid blue line), with the fit results also presented in Table 2.5. While the fit to all pixels shows a similar flat slope to the individual Fields ($\beta_{\text{all}} = 0.79$)⁷, we find that once averaged to ~ 700 pc scales, the data are consistent with the Herrera-Camus et al. (2015) relation within uncertainties. Therefore, while the [C II] vs SFR relation is flatter at small physical scales (~ 50 pc) due to the separation of diffuse [C II] emitting regions from the star forming regions, on kpc scales this diffuse emission is correlated sufficiently with star formation to provide the observed linear relation.

2.3.3 FAR-IR LINE DEFICIT

Another factor that affects the relation between [C II] emission and SFR is the efficiency of converting absorbed photons from the star forming region to [C II] emission. Depending on whether the gas is ionized or neutral, this efficiency will differ as a result of different heating processes (gas photoionization versus PE effect on dust grains). In our regions overall, we estimate the fraction of [C II] coming from ionized gas to be small. One region in Field 5 may have a larger than usual contribution from ionized gas, and is discussed in Section 2.3.3.1.

To get a rough estimate on the ionized [C II] contribution we first make use of several locally significant [N II] $\lambda 122\mu\text{m}$ measurements in Fields 1 and 3. The line is detected only in the brightest regions, with local $\log \Sigma_{\text{SFR}} > -1.5$. For these bright SF regions, we can estimate the ionized contribution to the total emission, $[\text{C II}]_{\text{ion}}/[\text{C II}]$, by following the prescription in Croxall et al. (2012), particularly their Figure 11. As the [C II]/[N II] ratio is density dependent and we have no constraint on the density, we assume a low density gas of $n_e \sim 2 \text{ cm}^{-3}$, resulting in a high value of $[\text{C II}]_{\text{ion}}/[\text{N II}] = 6$. Even with this assumption that provides us with an upper limit on the $[\text{C II}]_{\text{ion}}/[\text{C II}]$ ratio and probing the highest SF regions, we still find the ionized contribution to [C II] to be less than 50%, with $[\text{C II}]_{\text{ion}}/[\text{C II}] = 28\%$ and 40% in the SF regions of Field 1 and Field 3, respectively.

To further support the low $[\text{C II}]_{\text{ion}}/[\text{C II}]$ fraction, we estimate the contribution for the Fields as whole by using $\text{H}\alpha$ as a proxy. Groves & Allen (2010) models predict $[\text{C II}]_{\text{ion}}/\text{H}\alpha \sim 0.05 - 0.1$ in H II regions, assuming relative efficiency of ionized gas cooling by [C II] and $\text{H}\alpha$ lines. We measure everywhere the ratios of the surface brightness $[\text{C II}]/\text{H}\alpha > 0.5$. Thus, we infer from the models $[\text{C II}]_{\text{ion}}/[\text{C II}] \sim 20\%$ (for $[\text{C II}]_{\text{ion}}/\text{H}\alpha = 10\%$). However, we caution that our $\text{H}\alpha$ values were not corrected for extinction, and therefore we might slightly underestimate $[\text{C II}]_{\text{ion}}$ contribution. Nevertheless, we expect 10-50% of the [C II] could be from ionized gas, emphasizing that the majority of the [C II] arises from neutral gas.

⁷ Note, that the fit (blue line) does not go through the densest part of the number density plot, because the latter does not represent the uncertainties of the points, while the ODR fitting method takes them into account.

Therefore in M31 most of the neutral gas cooling occurs through the [C II] emission line, due to the weak [O I] detection and low [C II]_{ion} fraction. Given this, and that the neutral gas is predominantly heated by the photoelectric effect on dust grains, the ratio of [C II] to the total IR emission (TIR, tracing total dust absorption) should trace the photoelectric (PE) heating efficiency.

As described in the Introduction, [C II]/TIR has been found to vary globally with galaxy properties such as the total IR luminosity. In particular, a decreasing trend of [C II]/TIR versus $\nu I_{\nu}(70\mu\text{m})/\nu I_{\nu}(100\mu\text{m})$ (a proxy for the dust temperature), has been observed. Based on the study of global measurements of 60 normal galaxies, [C II]/TIR was found to decrease at high dust color values (i.e. warm dust temperatures; Malhotra et al. 2001), but it first was referred to as the FIR-line deficit for [C II]/TIR falling below 10^{-3} at high dust color values by Helou et al. (2001)⁸. Generally, [C II]/TIR was found to be approximately constant (with some scatter) at low dust temperatures, but sharply decreasing in galaxies with warmer dust colors ($\nu I_{\nu}(70\mu\text{m})/\nu I_{\nu}(100\mu\text{m}) \gtrsim 0.95$, Croxall et al. 2012). One of the most commonly given explanations for this deficit is grain charging, where warmer dust is more highly charged, increasing its PE threshold and thus decreasing the average energy returned to the gas per photon absorbed. Most of the studies of the deficit have concentrated on the [C II] line, because it is typically the brightest, but other lines have also been investigated, and show a similar deficit (e.g. [O I], [O III], [N II]; Graciá-Carpio et al. 2011).

In our Fields, we already have hints that the [C II]/TIR ratio and thus PE efficiency is changing between our SF regions and more diffuse regions, with Figures 2.5 and 2.6 revealing that the TIR fraction from the diffuse gas is greater than that of [C II] in all fields. Thus, [C II]/TIR seems actually higher in SF regions, somewhat contrary to the results in previous works for galaxies as a whole. However, we can also explore [C II]/TIR versus dust colors using our higher resolution at ~ 50 pc scales.

2.3.3.1 FAR-IR LINE DEFICIT ON ~ 50 PC SCALES

In Figure 2.8, we show the [C II]/TIR surface brightness ratio versus the $\nu I_{\nu}(70\mu\text{m})/\nu I_{\nu}(100\mu\text{m})$ ratio for individual pixels in Fields 1 to 5. Each pixel measures a region of ~ 20 pc, which slightly oversample our physical resolution of ~ 50 pc. Only pixels with a signal-to-noise greater than 3 in all quantities are plotted, with the $70\mu\text{m}$ flux being generally the most limiting quantity at these scales. In Figure 2.8, all points are color coded by their [C II] surface brightness as a proxy for diffuseness, where bluer pixels represent the more diffuse regions. Note that due to the limit of the $70\mu\text{m}$ flux, we do not probe the most diffuse regions explored in Section 2.3.1, as one can infer from the lower limit of the colorbar in the top right panel of Figure 2.8.

The [C II]/TIR ratios in all our fields span approximately an order of magnitude, between $\sim 2 \times 10^{-2} - 10^{-3}$, and span $\sim 0.3 - 2$ in dust color $\nu I_{\nu}(70\mu\text{m})/\nu I_{\nu}(100\mu\text{m})$, a very similar

⁸As the FIR-line deficit definition is vague, hereafter, we adopt the one given by Helou et al. (2001)

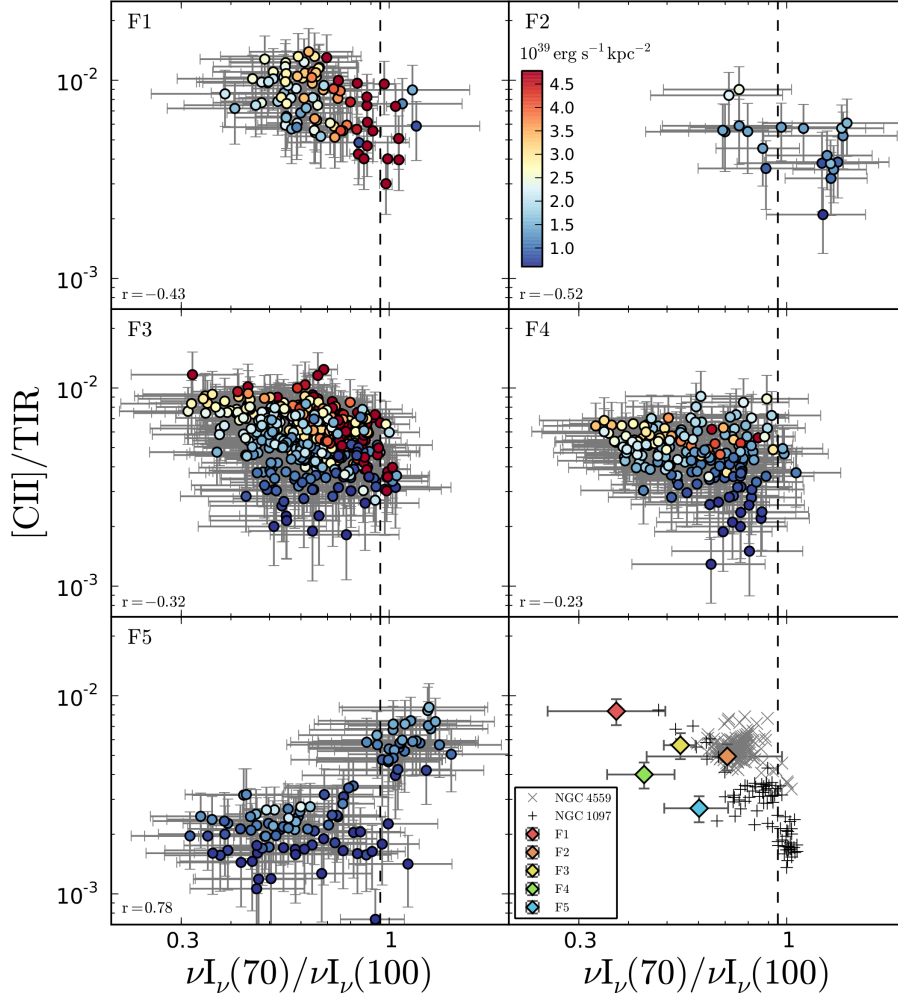


FIGURE 2.8: $[C II]/TIR$ surface brightness ratio (proxy for gas heating efficiency) versus $\nu I_{\nu}(70\mu m)/\nu I_{\nu}(100\mu m)$ (a proxy for dust temperature) for individual $5.2''$ pixels (~ 20 pc physical scale) for each Field (as labelled in top left corners of each panel). Only pixels with S/N above $3\text{-}\sigma$ in all quantities are shown, typically the $70\ \mu m$ flux is the limiting quantity. The pixels are color coded by the $[C II]$ surface brightness (with respect to the scale given in the top right panel). In the lower left of each panel we indicate the Pearson correlation coefficient r is given for each Field. p -values (roughly indicate the probability of an uncorrelated system) are high for F2 and F4, therefore correlation estimates for these Fields are not significant, while for the other Fields are sufficiently low to indicate a significant correlation. Lower right panel shows the same Figure from Croxall et al. (2012) for two galaxies with $\sim kpc$ pixels; NGC 4559 (gray crosses) and NGC 1097 (black '+' signs). The large diamonds show the integrated results for each of our Fields at the same physical scale (~ 700 pc), color coded by the Field number. Note, that the averages on the last panel take all the measurements in each Field, not only the $3\text{-}\sigma$ significant points.

phase space to where the bulk part of Malhotra et al. (2001) measurements for individual galaxies reside. All of our observed $[\text{C II}]/\text{TIR}$ ratios lie above the 10^{-3} value which classically defines the ‘[C II]-deficient’ objects Helou et al. (2001), thus we could state here that there is no [C II] deficit regions across our fields in M 31. The problem is that this classical deficit definition, as vague as it already is, was applied for global measurements, not for ~ 50 pc scales, at which scales it breaks down (manifested as a huge scatter in panels 1–5 in Figure 2.8), due to different scale lengths (spatial distributions) of [C II] and TIR (see Section 2.3.1.2).

However, we do find moderate to weak negative correlations of the $[\text{C II}]/\text{TIR}$ surface brightness ratio with the $\nu I_{\nu}(70\mu\text{m})/\nu I_{\nu}(100\mu\text{m})$ dust color in Fields 1 to 4 from the Pearson’s coefficients’ values ranging from -0.23 to -0.52 (see Figure 2.8). These weak correlations are consistent with the trends measured on global scales in previous studies, with weak negative correlations (Malhotra et al. 2001) or constant $[\text{C II}]/\text{TIR}$ values found across 0.3–1 in dust color (Helou et al. 2001; Graciá-Carpio et al. 2011).

However, contrary to the other fields, we observe a very strong positive relation in Field 5, with Pearson’s coefficient 0.78. This strong correlation is driven by the cluster of high $[\text{C II}]/\text{TIR} \sim 0.006$ points at the IR color of $\nu I_{\nu}(70\mu\text{m})/\nu I_{\nu}(100\mu\text{m}) \sim 1.2$, visible in the bottom left panel of Figure 2.8. All these pixels are located in the star forming region in the south-east in Field 5. This bright region contributes on its own to $\sim 25\text{--}30\%$ of the total [C II] emission in this ~ 700 pc Field. Despite a warm dust color, this region presents very weak IR emission, suggesting a low total dust mass. Given this low dust mass but relatively high [C II] emission, it is likely that this region is dominated by H II gas. Therefore, most of the [C II] emission arises from photoionized gas, and not from neutral gas where the PE effect dominates the gas heating, which leads to the abnormally high $[\text{C II}]/\text{TIR}$ values for these dust colors.

At a given dust color, it is clear that we see a large spread of the $[\text{C II}]/\text{TIR}$ ratio, as great as any trends inferred over our observed IR color range. Interestingly, it is noticeable in all Fields that, at a given dust color, there is an increasing trend of $[\text{C II}]/\text{TIR}$ with [C II] surface brightness. This clearly indicates that factors other than the dust temperature affect the PE efficiency. The details in each Field are sensitive to the geometry of the stars, dust and different phases of the gas. One possibility is that at this resolution, we can see the effects of softer radiation fields in non-SF regions, such that there are sufficient photons to heat the dust to the observed colors, but fewer photons of sufficient energy to eject electrons from the dust grains, leads to a relatively cooler ISM in the diffuse phase.

2.3.3.2 FAR-IR LINE DEFICIT ON ~ 700 PC SCALES

In the lower right panel of Figure 2.8 we plot the results from Croxall et al. (2012) showing the $[\text{C II}]/\text{TIR}$ surface brightness ratio versus the $\nu I_{\nu}(70\mu\text{m})/\nu I_{\nu}(100\mu\text{m})$ ratio on ~ 700 pc scales for two nearby galaxies: NGC 4559 and NGC 1097. We used the same instruments, data reduction and methodology (i.e. TIR prescription) as in Crox-

all et al. (2012) paper, which makes the comparison straight forward. Their resolution element scales are similar to our integrated Fields. The galaxies in their paper represent clear examples of a galaxy without a FIR-line deficit (NGC 4559) and with a deficit (NGC 1097). These galaxies show the same range in both axes as we see with our higher physical resolution, but show a stronger trend of decreasing [C II]/TIR with IR color, with Croxall et al. (2012) clearly demonstrating a lower ratio for these objects with warmer colors. On top of the results for these galaxies, we plot the integrated measurements for each of the Fields matching the ~ 700 pc pixel sizes. This comparison shows that despite observing cooler dust colors in our Fields than those observed in Croxall et al. (2012), we see a similar range in the [C II]/TIR ratio as in both NGC 4559 and NGC 1097. However, it is clear that F1 has a higher than average ratio.

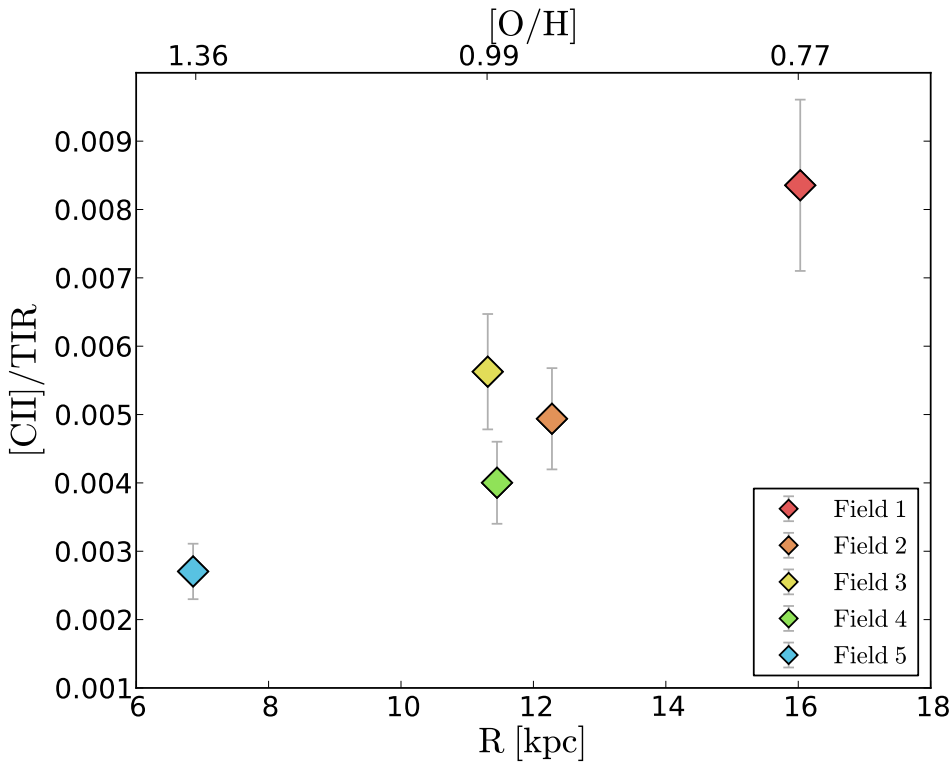


FIGURE 2.9: The integrated [C II]/TIR surface brightness ratio versus the galactic radius (bottom axis) and average gas-phase metallicity (top axis; oxygen abundance as a proxy for metallicity in units relative to solar $(O/H)/(O/H)_{\odot}$) for our 5 Fields. Fields 2 – 4 lie in the same 10 kpc gas rich ring, and have similar [C II]/TIR values.

With only 5 data points, we cannot conclusively identify a trend in the [C II]/TIR ratio with IR color on these scales in M 31. However, on closer examination, there is a trend with radius, shown in Figure 2.9. We observe in Figure 2.9 a strong radial relation with the [C II]/TIR ratio, with a lower value presented in the inner region, similar ratios seen for Fields 2 to 4 which all lie in the same 10 kpc gas rich ring that dominates IR and ISM images of M 31. A similar radial trend of the [C II]/TIR ratio is seen in M 33 (Kramer

et al. 2013). Smith et al. (in prep.) find a similar decreasing relation as a function of the gas-phase metallicity on ~ 1 kpc scales using the much larger sample of KINGFISH galaxies.

However, not only the metallicity varies with radius in M31, but many properties vary across M31 and could possibly affect the [C II]/TIR ratio, such as the stellar density and radiation field strength, as already seen at the higher resolution. We discuss these, and the association with the diffuse and SF regions in the following Section.

2.4 DISCUSSION

As the nearest massive spiral galaxy, M31 is an ideal laboratory to study the ISM on small scales while still being comparable to studies of similar galaxies at larger distances. Making use of this high physical resolution, we have explored the origins of [C II] and the dominant ISM heating processes by comparing the line emission strength and distribution against other tracers of ISM heating, the $H\alpha$ line, and the $24\mu\text{m}$ and TIR continuum.

2.4.1 [C II] ON ~ 50 PC SCALES

At our limiting resolution of $11''$ (~ 50 pc), we clearly see a strong correlation of the [C II] emission with $H\alpha$ through the spatial coincidence of the surface brightness peaks in the maps in Figures 2.2 and 2.3. However, the [C II] emission in the maps appear to be more spatially extended than the $H\alpha$. We quantified this spatially extended [C II] emission by separating each Field into “SF regions” and “diffuse”, based on a $H\alpha$ surface brightness cut that encompassed the majority of H II regions. We find that [C II] is always more spatially extended than $H\alpha$, which arises predominantly from “SF regions”, but less so than the dust emission (traced via the TIR), which had the highest diffuse fraction in all Fields. As our “SF regions” are 100’s of pc in physical size they encompass several H II regions (as seen in Figures 2.2 and 2.3), thus the larger diffuse fractions cannot simply be the result of us resolving out the H II regions and associated photodissociation regions, but indicative of a real diffuse emission.

The association of [C II] with recent star formation is further supported by the significant correlation between the [C II] surface brightness and SFR surface density on ~ 50 pc scales (Figure 2.7). The presence of a diffuse contribution to the [C II] emission is indicated by the sub-linear slopes found for all Fields in the logarithmic relationship.

Thus the resolved [C II] emission in Andromeda reveals that some fraction of the [C II] line originates from gas directly heated by UV photons from star-forming regions, with this fraction dependent upon the local SFR surface density. While this SF region [C II] includes both contribution from the ionized gas in H II regions and the neutral gas in the

directly associated photodissociation regions which are unresolved in our observations, we find that the H II region contribution must be less than 40% across our map based on our few [N II] 122 μ m detections and model-based estimates from the H α maps. The remaining [C II] flux arises from a diffuse phase, not spatially coincident with star-forming regions, that is also associated with a large fraction of the TIR surface brightness.

The heating source for this diffuse phase is not directly obvious. We consider two mechanisms for the heating of this diffuse phase: (1) photon leakage from SF regions, and (2) a distinct diffuse UV radiation field.

In the first mechanism, the diffuse gas and dust are heated primarily by photons that have escaped the immediate vicinity of the young, massive stars that emit them. Such a mechanism has been put forward to explain the diffuse H α emission. As the FUV photons that heat the dust and gas, are less energetic than ionizing photons and have a longer mean free path, will cause the spatial extent of the diffuse [C II] emission to be greater than that of H α . In this scenario, even though we have seen a large diffuse [C II] component, it is still associated with the stars that heat SF regions. This means the use of [C II] as a SFR indicator should still be valid on scales large enough (\sim kpc) to average over these leakage effects. Possible evidence for this mechanism are the overdensity of points below the best-fit line at the bright end of the [C II]-SFR relation in F3, F4 and F5 (Figure 2.7) that could indicate regions where the ionizing photons have been absorbed, but the FUV photons have leaked to adjacent regions.

The second mechanism is where the diffuse UV radiation field arises from sources different to the massive stars powering the SF regions. The most likely source of this diffuse UV field would be B-stars, as in the solar neighborhood (Mathis et al. 1983). B-stars generate sufficient far-UV photons to heat the neutral gas, but negligible amounts of ionizing photons. In addition, they would have a more uniform spatial distribution than O-stars due to their longer lifetimes. If the [C II] is predominantly heated by these stars, it will still measure the SFR, but over longer timescales than H α .

Both of the suggested mechanisms will result in a softer radiation field outside of the SF regions. If the heating photons come purely from recent star-formation, we expect a softening of the radiation field with distance from the SF regions as the harder photons are preferentially absorbed. If the diffuse UV radiation field arises from a different stellar population, a softening of the radiation with distance from the SF regions requires that the mean age of the stellar population increases with distance from the youngest stars. Further evidence for the diffuse heating mechanisms can be seen in Figure 2.8, where, in every Field, for a given dust color (i.e. dust temperature) there is an increasing trend of [C II]/TIR with increasing [C II] surface brightness. This suggests that the brightest [C II] emitting regions (which we have shown to be associated with SF regions) have a higher heating efficiency. One way to produce such a trend is to have softening of the radiation field from SF regions to the more diffuse ISM, reducing the relative energy input to the gas (requiring > 6 eV photons) as compared to the dust heating (which absorbs all photons).

Realistically, it is likely that both mechanisms play a role, with leaked FUV photons from SF regions gradually merging with the radiation field from an underlying diffuse stellar population. Only through the knowledge of the relative distribution of the stellar population in comparison with the observed dust emission could the relative contribution of each mechanism to the [C II] emission across our Fields be disentangled.

2.4.2 [C II] ON ~ 700 PC

It is clear from the previous Section (2.4.1) that at the larger scales of our integrated Fields (~ 700 pc), there will be contributions from diffuse emission to both the [C II] surface brightness and Σ_{SFR} (based on H α and $24 \mu\text{m}$). Based on Figure 2.6, this diffuse fraction contribution will be greater than 50% in some regions, depending upon the local SFR surface density. Nevertheless, when we look at these \sim kpc scales, we find that the integrated Fields are consistent with the [C II]– Σ_{SFR} relation found on similar scales by Herrera-Camus et al. (2015). From this we can infer that this diffuse emission is sufficiently correlated with SFR on these scales that the relation holds, meaning that, for our two suggested mechanisms for the heating of the diffuse gas, on these scales we must capture all leaked photons or that the source of the diffuse radiation field, i.e. B-stars, are co-located with star-formation on \sim kpc scales.

On the other hand, we do find large scale variations of [C II]/TIR with galactocentric radius in M31 (Figure 2.9). If the [C II]/TIR ratio is tracing PE heating efficiency, then it is puzzling how the relationship with SF can stay the same as in Herrera-Camus et al. (2015), when this efficiency appears to vary so dramatically, by a factor of ~ 3 , between Fields 1 and 5. Taken together what this suggests is that there is a constant FUV energy fraction emitted by stars transferred to gas that is then cooled by [C II], but that the TIR must decrease relative to both [C II] and SFR with increasing galactocentric radius.

While a changing ionized gas contribution to the [C II] emission could possibly explain the [C II]/TIR ratio, we have demonstrated that this contribution is less than 50% in even the highest Σ_{SFR} pixels at 50 pc scales, and thus will be much less on the scales of our integrated Fields. Thus this cannot explain the factor of ~ 3 variation.

It is also possible that the fraction of the FUV energy absorbed by dust that goes into the gas can change (an increase in the physical photoelectric heating efficiency) and thus alter the [C II]/TIR ratio. However this also requires some form of “conspiracy” to maintain the [C II]– Σ_{SFR} relation, such as decreasing the FUV absorbed by dust relative to the SFR when the PE efficiency increases. Thus, while we cannot discount this possibility, we believe it to be unlikely. This is further supported by the non-monotonic radial trend in q_{PAH} , the mass fraction of dust in PAHs, as determined by Draine et al. (2014), in particular their Figure 11. A larger mass fraction of PAHs should lead to more efficient heating (Bakes & Tielens 1998), yet the determined trend in q_{PAH} peaks at ~ 11.2 kpc, unlike the monotonic [C II]/TIR ratio.

A more likely physical explanation for the [C II]/TIR decrease towards galaxy center might lie in the fact that dust can be heated by both UV and optical photons, while both H α and [C II] require harder photons (> 13.6 and $\gtrsim 6$ eV, respectively). Thus to reduce the TIR relative to [C II] as a function of radius, the FUV absorbed by dust must increase relative to the lower energy photons (< 6 eV) absorbed by dust. This is possible through changing either the intrinsic heating spectrum or by changing the dust properties.

The hardness of the intrinsic stellar spectrum heating the dust will change with both stellar metallicity and local star formation history (parameterized through the mean stellar age). The gas-phase metallicity, and presumably the stellar metallicity, decreases monotonically with radius, with a factor of 2 change between Field 1 and Field 5 (based on the dust-to-gas ratios work in Draine et al. 2014). To assess the impact of metallicity on spectral hardness, we compare two almost identical $10^6 M_{\odot}$ clusters at the age of 10 Myr, modelled with Starburst99 (Leitherer et al. 1999), with an instantaneous star-formation burst and Kroupa initial mass function, differing only by solar ($Z = 0.02$) and subsolar (LMC, $Z = 0.004$) metallicities. The relative hardness increases by $\sim 15\%$ from the solar to subsolar metallicity cluster, as measured by comparing the change in the FUV ($\nu > 6$ eV) to NUV ratio. While this will contribute to the observed trend in [C II]/TIR, it is not sufficient to explain the factor of 3 change.

The local star formation history can strongly affect the heating spectrum seen by dust. A clear example of this is the work of Groves et al. (2012), who showed that in the bulge of M 31 an old stellar population dominates the heating radiation field, with its extremely soft radiation field meaning that optical light actually dominated the heating of dust. Thus we do expect a hardening of the radiation field with increasing radius in M 31 as we move from older bulge dominated regions to younger disk dominated regions. Evidence for this can be seen in the observed radial FUV-NUV color in M 31 shown in Thilker et al. (2005), where the bluer color with radius may indicate a younger mean stellar age. The SFR, however, does not vary monotonically with radius, peaking in the 10 kpc ring, and this will also affect the hardness of the local radiation field.

Changing the dust properties can also change the [C II]/TIR ratio by changing the relative amount of FUV photons absorbed. One clear way is to change the dust absorption curve, which steepens with decreasing metallicity as seen through comparison of the extinction curves of the Milky Way versus the LMC (Gordon et al. 2003). The steepening from a Milky Way opacity to a LMC opacity, as plausibly expected from a decrease in the metallicity by a factor of 2, will mean relatively more FUV photons will be absorbed, however this increase is relatively small (see Figure 10 in Gordon et al. 2003) and will not contribute a significant amount to the [C II]/TIR increase.

In addition to steepening the opacity curve, decreasing the metallicity will also decrease the dust-to-gas ratio (DGR), which has been found to decrease monotonically with radius in M 31 (Draine et al. 2014). Decreasing the DGR will decrease the overall dust opacity for the same column of gas, increasing the mean free path of optical and UV photons, and decreasing the total amount of photons absorbed (a similar argument was put forward by Israel et al. 1996, for the high ratios observed in the LMC). Lower dust opacity will

increase the average energy absorbed by dust, as preferentially the FUV photons are absorbed and the NUV-optical photons escape (due to the steep power-law nature of the dust opacity), and this decreasing opacity will lead to some part of the radial FUV-NUV color gradient observed in Thilker et al. (2005). Supporting this idea, we find that the $24\ \mu\text{m}/\text{H}\alpha$ ratio (a measure of the SF region extinction) increases with decreasing $[\text{C II}]/\text{TIR}$ ratio, albeit in a non-linear manner. However, the overall dust opacity depends upon the total dust column, and this has been found to peak around the 10 kpc ring in M 31 (Draine et al. 2014), and is the region with the highest expected extinction (Tempel et al. 2010). This non-monotonic trend in total extinction goes against the simple trend seen in Figure 2.9.

A similar explanation was suggested by Israel et al. (1996) for an increase of the $[\text{C II}]$ emission relative to IR that they found with decreasing metallicity in an exploration of the LMC. In the low metallicity environment of the LMC ($Z_{\text{LMC}} = 0.004$), $[\text{C II}]/\text{FIR}$ was found to be ~ 10 times higher than found in Milky Way ($Z_{\odot} = 0.02$; see Israel et al. 1996, and references therein). Their explanation for this was that at the low metallicities, the clumpy nature of the ISM caused deeper penetration of FUV photons into the molecular clouds, for the same A_V , increasing the $[\text{C II}]$ flux for the same absorbed radiation.

Therefore, it is likely that a combination of a radial variation in both the dust opacity and star formation history causes the observed radial trend in the $[\text{C II}]/\text{TIR}$ ratio in M 31. While we favor the change of the radiation field due to mean stellar age as being primarily responsible for the observed radial trend in $[\text{C II}]/\text{TIR}$ due to the observed FUV-NUV and extinction gradients, to correctly disentangle which of the mechanisms dominates in M 31 will require a determination of the spatially resolved star formation history in M 31. This is currently being undertaken by the Pan-chromatic Hubble Andromeda Treasury Survey (PHAT Dalcanton et al. 2012; ?), covering all of our Fields. With the intrinsic heating stellar spectrum being determined from this analysis, we will be able to correctly account for this effect on the $[\text{C II}]/\text{TIR}$ ratio and demonstrate whether this is indeed the dominant mechanism.

For galaxies in the Local Group, we should be able to demonstrate the same effects, by comparing resolved star formation histories and extinction maps against the observed $[\text{C II}]/\text{TIR}$ ratio. This should answer to what extent the observed $[\text{C II}]/\text{TIR}$ trends in galaxies are due to heating effects or true changes in the photoelectric heating efficiency.

2.5 CONCLUSIONS

In this Chapter we present an analysis of $[\text{C II}]$ $158\ \mu\text{m}$ emission in five Fields in M 31. Combined with ancillary $\text{H}\alpha$ and IR emission data, we studied the origins of $[\text{C II}]$, its relation with the SFR and the ISM properties. In particular, we have found:

- Significant amounts of $[\text{C II}]$ line emission are coming from outside the SF regions.

- Even though we measure a large diffuse [C II] fraction, integrated over \sim kpc scales, [C II] still traces the SFR very similarly to what we see in larger samples of more distant galaxies. We explore different mechanisms that could be responsible for this diffuse phase including leakage of photons from H II regions or diffuse UV radiation field generated by B stars. More diffuse [C II] than H α emission is consistent with flatter slopes.
- [C II] and SFR are correlated, but with a shallower slope than seen on \sim kpc scales. This may be a result of the same diffuse [C II] emission.
- All of our observed [C II]/TIR ratios lie above the 10^{-3} value, which classically defines the ‘[C II]-deficient’ objects. Yet this is not surprising as we explore much smaller scales than the global measurements that defined the deficit, and much more quiescent conditions than the centers of ULIRGs in which this deficit is clearly seen. On 700 pc our Fields do show a tentative decreasing trend of [C II]/TIR with $70 \mu\text{m}/100 \mu\text{m}$, however, with only 5 points, considerable scatter and large dust color uncertainties, it is not significant. On the smaller 50 pc scales we do generally see a weak correlation of decreasing [C II]/TIR with warmer dust colors. However, this trend is inverted in F5 and in all fields we see a significant scatter (\sim order of magnitude) at a given dust color, that may be related to the [C II] surface brightness.
- We observe a large scale gradient of [C II]/TIR across the disk of M 31. We explore potential causes for this trend and argue that a combination of effects due to changes in the dust-to-gas ratio, dust extinction curve, star formation history and radiation field are likely responsible.

Using [C II] to trace the massive SFR, one must consider possible contributions to ISM gas heating by older stellar populations that can lead to tracing longer timescales, and/or leaked photons from H II regions. The issue caused by the latter should go away when averaged over larger scales \sim few hundred pc. We will be able to shed some light in a following paper resolving stellar populations and their energy input in M 31 using the PHAT survey (Kapala et al. in prep.).

CHAPTER 3

NON-SF HEATING RELATED [C II] EMISSION IN THE BULGE OF M 31

3.1 INTRODUCTION

[C II] 158 μm is a forbidden fine-structure line arising from singly ionized carbon C^+ (from the $^2P_{3/2} \rightarrow ^2P_{1/2}$ transition). It is one of the brightest emission lines in most galaxies, and the dominant coolant of the neutral interstellar medium (see Section 1.3). Due to its wavelength close to the dust continuum emission peak, it is also highly detectable out to high redshifts (e.g., $z=6.4$ using ALMA; Walter et al. 2009).

One of the driving reasons to examine the [C II] line is its potential to trace star-formation rates (SFRs). The physical motivation is that the heating of neutral gas requires photons with energies 6 – 13.6 eV to be heated via photoelectric (PE) effect on dust grains. Therefore neutral gas cooling via the [C II] emission line should correlate with energetic enough photons produced by massive stars associated with recent star formation (\lesssim few 10^7 yr) that will dominate the production of such photons. Empirically, the relation between [C II] and SFR has been measured to be close to one–one on \sim kpc scales (de Looze et al. 2011; De Looze et al. 2014; Herrera-Camus et al. 2015).

Because [C II] can be observed from nearby out to high redshift, as a potential SFR tracer it may help us understand different phases of galaxy evolution (Carilli & Walter 2013). Unfortunately, there are issues with [C II] as a SFR tracer as the [C II] emission can arise from different interstellar medium phases (as C^+ has a lower ionization potential than hydrogen at 11.2 eV): the cold and warm neutral medium (CNM and WNM, respectively), and the warm ionized medium (WIM). The photoelectric effect (PE) is the dominant heating mechanism in the neutral phase, while in the ionized phase photoionization is

responsible for gas heating. It is crucial to understand how these different interstellar medium (ISM) phases contribute to the total [C II] emission we measure, and the underlying physical processes, such as heating efficiencies. If the heating efficiency changes, it will affect [C II] as a SFR indicator.

The [C II]/TIR is often used as a proxy for PE efficiency (ϵ_{PE}^{dust}), representing the energy that enters the gas relative to the energy absorbed by dust. This led to the so called “[C II] deficit”, which is vaguely defined as the ratio of the [C II] over the total infrared (TIR) emission decreasing as a function of warmer dust color (a proxy for dust temperature; Malhotra et al. 2001), or [C II]/TIR values below 10^{-3} (Helou et al. 2001). The observed and “[C II] deficit” has been explained as reduced PE efficiency due to dust grains charging through the increased required energy potential threshold for subsequent photons to eject another electron (Malhotra et al. 2001; Croxall et al. 2012), or the depletion of polycyclic aromatic hydrocarbons (PAHs; very efficient contributors of photoelectrons) relative to bigger dust grains (Helou et al. 2001), or increased ionization parameter (Graciá-Carpio et al. 2011).

Many recent studies that have pursued the relative contribution of ISM phases to the [C II] emission use galaxies in the local universe (Croxall et al. 2012; Cormier et al. 2015), mainly because of the higher physical resolution. The proximity of the Andromeda galaxy (M 31) allows us to take these studies further, where we can begin to resolve H II complexes with the resolution ~ 50 pc at $158 \mu\text{m}$ with *Herschel* PACS and SOFIA FIFI-LS. Using the Survey of Lines In M 31 (SLIM; PI Sandstrom), Kapala et al. (2015) showed that [C II]-SFR correlates well even on small scales (~ 50 pc). Surprisingly, the [C II]-SFR relation holds independently of the [C II]/TIR ratio which varies dramatically with radius in M 31’s disk. A possible explanation why the [C II]/TIR ratio changes while the [C II]-SFR relation holds in the SLIM fields, is that the relative dust to [C II] emission changes while the gas heating photons above 6 eV produced by young stars and gas cooling via [C II] are correlated. This can be accomplished by (1) change in the hardness of the integrated stellar spectrum, or (2) change in the opacity curve due to varying dust-to-gas ratio (e.g. allowing photons at longer wavelengths to escape preferentially for lower dust-to-gas ratio in the outer parts of the galaxy). We refer to Section 2.4 in the previous chapter for an extensive discussion about these issues. The [C II] $158 \mu\text{m}$ line over total infrared (TIR) emission ratio in other galaxy centers has been found to be in “deficit” relative to their outer regions (Kramer et al. 2013; Smith in prep.; Croxall in prep.).

Most of the studies done on [C II] as a SFR tracer are in star-forming, “main sequence” spiral galaxies and low metallicity dwarf galaxies. One exception is an analysis of the [C II] emission in four early type galaxies (ETGs) presented by Malhotra et al. (2000) and observed with the Infrared Space Observatory (ISO). Malhotra et al. (2000) showed that the [C II] and H α spatial distributions do not coincide and concluded that [C II] comes from the neutral phase of the ISM. Three of these ETGs galaxies have lower $L_{[CII]}/L_{FIR}$ than typically found in the full survey sample (Malhotra et al. 2001), which they explain by softer radiation fields from old stellar populations producing fewer > 6 eV photons relative to the total dust heating photons.

M31 is a unique target because of its prominent bulge that can serve as a laboratory to study resolved ISM in the early type galaxy (ETG)-like environment (the bulge optical color is red, with $B - V \simeq 0.9 - 1.0$, and places the bulge in the ETGs space; Walterbos & Kennicutt 1987). M31 is an early-type spiral galaxy (SA(s)b; NED) with a very moderate SFR $\sim 0.4 M_{\odot} \text{yr}^{-1}$ (Barmby et al. 2006). M31’s evolutionary state might enable us to explore SFR tracers in quenching galaxies (integrated colors and luminosity place M31 in the ‘green valley’ space; Mutch et al. 2011).

All of the applied methods confirm that M31’s bulge is old. From resolved stellar NIR color-magnitude diagrams (CMDs), Olsen et al. (2006) constrain stellar populations to be older than 6 Gyr. From slit spectroscopy observations, simple stellar population and absorption Lick indices profile modelling, Saglia et al. (2010) estimate the bulge stellar age to be above 12 Gyr (excluding few innermost arcseconds). Most recently, based on resolved HST wide-band imaging (Panchromatic Hubble Andromeda Treasury survey; Dalcanton et al. 2012) Rosenfield et al. (2012) found no indication of young stellar populations, instead concluded that any UV emission arises from evolved, post-asymptotic giant branch stars.

We revisit archival ISO [C II] observations (Mochizuki 2000), to study [C II]/TIR and [C II] origins in the bulge of M31. We will use the combined bulge and SLIM data to see how the softer radiation field affects the [C II]/TIR ratio in M31, especially as we know from the work of Groves et al. (2012) that the optical (not FUV) light from old stars dominates the heating of dust in the bulge.

This chapter is organized as follows: in Section 3.2, we describe the data we use, including the archival ISO measurements and ancillary observations, along with the new calculations of TIR. In the following Section 3.3 we point out the surprising aspects of [C II] emission in the bulge. In Section 3.4 we study the total energy budget in the bulge to see what may be powering the observed bright [C II] emission, given the weak or non-existent star formation. In the next Section 3.5 we look at the energy balance in the regions in the disk, and we perform a detailed comparison between the bulge and the disk regions, to see what may cause the excessive [C II]/TIR. Finally, in Section 3.6 we discuss the implications of this study for our understanding of the origins of the [C II] emission line in galaxies and its use as a SFR tracer, in both resolved and integrated studies of galaxies.

3.2 DATA & TECHNIQUE

The key data in this chapter are the archival Infrared Space Observatory (ISO; Kessler et al. 1996) observations of [C II] 158 μm emission line in the bulge of M31 from Mochizuki (2000). All of the 20 pointings were obtained across the bulge ($00^{\text{h}}42^{\text{m}}44.^{\text{s}}35, +41^{\circ}16'08''.60$ (J2000) $\pm 750''$), along the major axis (the position angle is 38° ; see Figure 3.1). The ISO [C II] measurements are given in surface brightness in Table 3.1, the

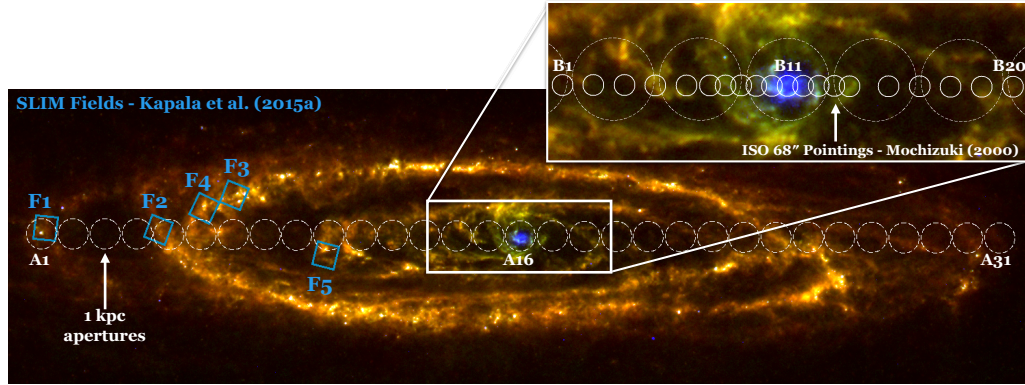


FIGURE 3.1: Three color dust emission image (red - SPIRE 250 μm , green - PACS 160 μm and blue - MIPS 24 μm). The white 1 kpc apertures (dashed circles) indicate where the integrated SED modeling with MAGPHYS along the major axis of M 31 have been performed. The [C II] ISO pointings from Mochizuki (2000) are shown in the zoomed in panel. The SLIM survey fields are overlaid in blue.

positive offsets are in the NE direction. The beam size of Long-Wavelength Spectrometer (LWS; Clegg et al. 1996) at 158 μm is 68''.

To complement the *ISO* data, we also examine the [C II] emission in five $\sim 700 \times 700$ pc fields (Kapala et al. 2015) measured with *Herschel* PACS at the resolution ~ 50 pc, FWHM = 11''.4. For details on data reduction see Kapala et al. (2015) or Section 2.2.1 in this thesis.

We also use *Herschel* and *Spitzer* infrared (IR) photometry. Observations of M 31 were done with the Multiband Imaging Photometer (MIPS; Rieke et al. 2004) on board of the *Spitzer* Space Telescope (Werner et al. 2004) by Gordon et al. (2006) and the InfraRed Array Camera (IRAC; Fazio et al. 2004) by Barmby et al. (2006). At the longer wavelengths, M 31 was observed with the *Herschel* Space Observatory (PI O. Krause) using the PACS and SPIRE instruments (Griffin et al. 2010, Spectral and Photometric Imaging Receiver). *Herschel* observations and processing details can be found in Groves et al. (2012) and Draine et al. (2014).

The *Spitzer* bands of interest are the IRAC 8 μm with a FWHM=2''.0 and the MIPS 24 μm with a FWHM=6''.5. The *Herschel* FWHMs are 5''.6 for PACS 70 μm , 6''.8 for PACS 100 μm , 11''.4 for PACS 160 μm , 17''.6 for SPIRE 250 μm , 24''.9 for SPIRE 350 μm and 36''.3 for SPIRE 500 μm . Beam sizes are taken from *Herschel* Observer's Manuals¹ for 20''s⁻¹ scans. In all PACS bands pixel size is 1'', in SPIRE 250 μm it is 6'', in SPIRE 350 μm it is 10'', and in SPIRE 500 μm it is 14''.

M 31 has also been observed with narrowband H α imaging by Devereux et al. (1994) with Case Western Burrell Schmidt telescope at the Kitt Peak National Observatory.

¹http://herschel.esac.esa.int/Docs/PACS/html/pacs_om.html and
http://herschel.esac.esa.int/Docs/SPIRE/html/spire_om.html

TABLE 3.1: *ISO and Herschel measurements across the bulge of M 31*

Offset ["]	[C II] ^a [10 ³⁸ erg s ⁻¹ kpc ⁻²]	TIR [10 ⁴⁰ erg s ⁻¹ kpc ⁻²]
+725	≤ 3.40	6.34
+625	≤ 3.30	6.53
+525	≤ 2.81	4.58
+425	3.59 ± 0.58	15.42
+325	≤ 5.24	8.08
+250	3.88 ± 0.49	12.61
+200	6.21 ± 0.68	20.82
+150	7.09 ± 0.58	21.78
+100	9.51 ± 0.68	32.05
+50	14.07 ± 1.36	47.39
0	14.17 ± 1.16	39.26
-50	10.68 ± 1.36	29.67
-100	10.48 ± 0.78	28.14
-150	6.89 ± 0.68	20.97
-200	6.79 ± 0.97	18.34
-325	≤ 3.49	2.34
-425	≤ 3.20	3.99
-525	≤ 4.08	6.26
-625	≤ 3.40	9.06
-725	≤ 3.88	7.82

^a Based on Table 1 in Mochizuki (2000), where the uncertainty represents 1 σ , and the upper limit corresponds to a 4 σ level.

The narrowband filter used not only includes H α (λ 6563 Å), but also includes the [N II] (λ 6584 Å) emission line and stellar continuum. Devereux et al. (1994) reduced, subtracted stellar continuum emission and sky from the images.

3.2.1 ANCILLARY MULTIWAVELENGTH DATA

To determine the possible stellar heating of the gas and dust in the ISM, we use *GALEX* UV and *SDSS* optical maps.

3.2.1.1 GALEX & SDSS

The far UV range is covered by *Galaxy Evolution Explorer* (*GALEX*) FUV (1350 – 1750 Å) and NUV (1750 – 2800 Å) bands. Far UV observations of M 31 (Thilker et al. 2005) have been obtained as part of the *GALEX* Nearby Galaxy Survey (NGS; Bianchi

et al. 2003, 2005). Typical 1σ limits are 6.6×10^{19} and 2.8×10^{19} erg s⁻¹ cm⁻² Å⁻¹ for FUV and NUV, respectively (in surface brightness these limits correspond to 28.0 (28.2) AB_{mag} arcsec⁻¹ in FUV (NUV)). The FWHMs is 4.0'' for FUV, and 5.6'' for NUV bands (pixel size of both bands is 1.4''), therefore these bands cannot be used for individual star photometry, but are vital for the integrated photometry of our regions of interest. We subtract constant sky values 0.000929 MJy sr⁻¹ (FUV), and 0.004712 MJy sr⁻¹ (NUV) derived by (Thilker et al. 2005).

The Sloan Digital Sky Survey (SDSS; York et al. 2000) covered entirely the disk of M 31 in a contiguous strip using the 5 *ugriz* filters. As *SDSS* imaging is well-calibrated, and the strip large enough to estimate the sky background, this data is ideal for determining the integrated optical photometry of M 31. Here we use the *ugriz* mosaics of Tempel et al. (2011). Details of the reduction of the *SDSS* images and the important sky removal are described in Tempel et al. (2011) and Tempel et al. (in prep.). The units are nanomaggies per pixel (0.396''), where nanomaggie is a linear unit of flux density equal to 10⁻⁹ maggies. A star of brightness 1 nanomaggie has a magnitude of 22.5 in any band, or a flux density of 3.631 × 10⁻⁶ Jansky. The average point-spread function across the images is 1'', more than sufficient for our integrated photometry.

3.2.2 METALLICITY

There are no direct measurements of the gas phase metallicity in the M 31's bulge. We use the Zurita & Bresolin (2012) estimate of the radial metallicity gradient based on elemental abundances measured in the H II regions in M 31 between 8 kpc and 16 kpc using "direct" methods:

$$\frac{Z}{Z_{\odot}} \approx 1.81 \times \exp(R/19 \text{ kpc}). \quad (3.1)$$

However, we extrapolate the Zurita & Bresolin (2012) relation 3.1 to estimate the gas phase metallicity in the bulge.

3.2.3 PROCESSING

We convolved all of the images to match the ISO [C II] beam size using kernels from Aniano et al. (2011), and resampled using MIPS 160 μm pixel grid.

We estimate total infrared emission (TIR) based on *Herschel* and *Spitzer* photometry. Note that any TIR approximation including the 8 μm band overestimates the real total dust emission in M 31's bulge due to the large contribution of stellar continuum in this waveband (see spectral energy distribution in Figure 3.2 and Appendix 3.A for details on the TIR issues within M 31's bulge). Thus, we use a Galametz et al. (2013) empirical formula for the TIR surface brightness:

$$TIR = 0.767 \times S_{70} + 0.503 \times S_{100} + 0.558 \times S_{160} + 0.814 \times S_{250}, \quad (3.2)$$

where the TIR and *Herschel* surface brightness measurements are in W kpc^{-2} .

3.2.3.1 MAGPHYS SED FITTING TECHNIQUE

To infer about the intrinsic UV/optical spectra of the regions we use the spectral energy distribution (SED) modelling of the integrated photometry by assuming that the energy is conserved.² The SED fitting code **MAGPHYS** (da Cunha et al. 2008) compares the photometric observations of galaxies at any redshift with computed photometry from libraries of stellar population synthesis model spectra and model IR SEDs. The template stellar population spectra (light generated by stars in galaxies) are derived using (Bruzual & Charlot 2003) stellar synthesis code. The stellar libraries provide high resolution spectra from the rest frame UV to IR and include a range of star formation histories, including bursts, assuming a Chabrier (2003) initial mass function (IMF). The final stellar library spectra are attenuated by dust over a range of A_V s assuming a two-component model (Charlot & Fall 2000), which takes into account the effect of the higher attenuation of young ($\lesssim 10^7$ yr) stars in the natal clouds (τ_λ^{BC} , optical depth in birth clouds), in addition to the attenuation of all stars by dust in the ambient ISM (τ_λ^{ISM}).

The library of dust emission spectra is calculated from a four-component model created specifically for **MAGPHYS** by da Cunha et al. (2008). The main contributors to this model are PAHs (emitting spectral features between 3 and 20 μm), stochastically heated very small grains ($a < 0.01 \mu\text{m}$, emitting at mid-IR wavelengths $\lesssim 40 \mu\text{m}$), and two emitting components of cold and warm large grains in thermal equilibrium (emitting at far-IR wavelengths).

The **MAGPHYS** strength lies in the consistent modelling of the stellar and dust emission from FUV to far-IR. The main assumptions made are that the heating is generated only by stars, and that the energy is conserved, meaning that the absorbed energy equals the energy reradiated by dust. The template spectra are “translated” into SEDs in the same filters/passbands as measured in the photometric observations (full model grid). Finally **MAGPHYS** is using a Bayesian approach, and calculates the likelihood distribution of each physical parameter by evaluating how well each SED in the model grid accounts for the observed properties of the galaxy (for details on the assumed priors see da Cunha et al. 2008). We present an example SED fit to the bulge of M 31 in Figure 3.2.

3.2.3.2 ATTENUATED STELLAR EMISSION

We use the intrinsic and reddened stellar spectra fitted with **MAGPHYS** to assess the stellar energy contributions to the ISM heating. The attenuated stellar emission is the difference between the intrinsic (unreddened; blue curve in Figure 3.2) and reddened model

²However, on sub-galactic scales this assumption might not be fulfilled, and will increase uncertainties of the fitting technique/results.

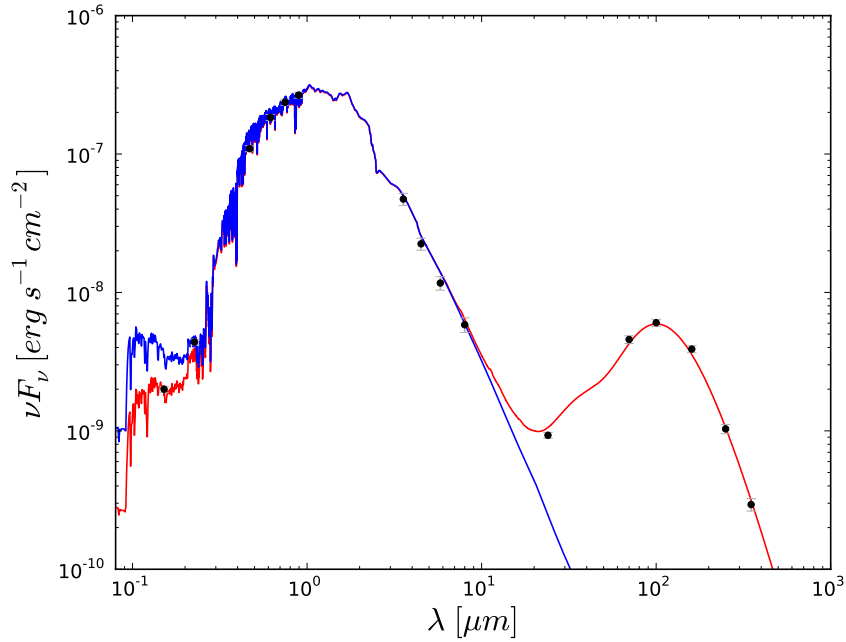


FIGURE 3.2: The SED of the central kiloparsec region of M 31, measured within a circle of 1 kpc (4.405') radius from the center. The photometric measurements used for the fit: GALEX FUV and NUV, SDSS *g*, *r*, *i* and *z*, Spitzer IRAC and MIPS 24 μm , and all Herschel bands except SPIRE 500 μm .

spectrum (red curve in Figure 3.2) that best fit the observed data.

We define two energy bins. The first, between 6 eV and 13.6 eV, captures the energy input from photons capable of ejecting electrons from the dust grain surface (UV_{att} ; indicated as the blue area in the bottom panel in Figure 3.3). The second, between 0.41 eV and 13.6 eV, measures the total stellar energy absorbed and scattered by dust (TOT_{att} ; marked as the hatched area in the bottom panel in Figure 3.3). Their ratio (UV_{att}/TOT_{att}) represents an estimate of the fraction of stellar energy, a part of which can contribute to gas heating compared to the total stellar energy contributed to the ISM heating (approximated by dust emission).

3.3 [C II] EMISSION IN THE BULGE AND DISK OF M 31

From the values in Table 3.1 we see that [C II] emission in the bulge region is surprisingly bright given there is little to no active star formation there. When we compare the average [C II] surface brightness in the bulge to that in the disk as measured in our SLIM fields (Figure 3.4, top panel), we find the emission is comparable to regions with significantly

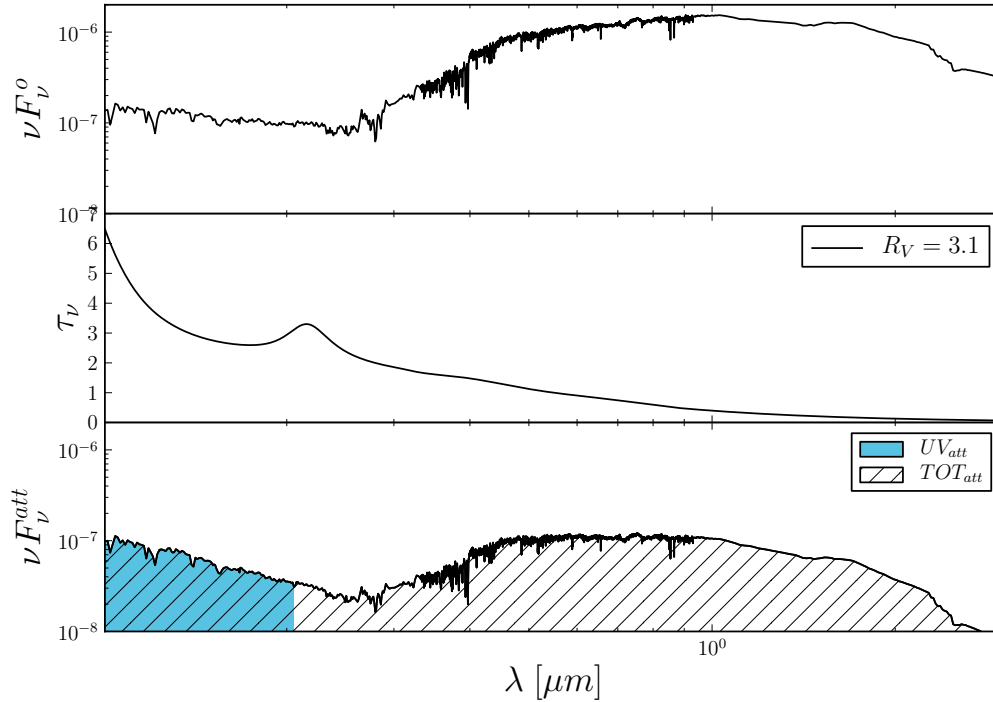


FIGURE 3.3: Top panel presents the intrinsic stellar spectrum of the entire disk ($0.75^\circ \times 3.38^\circ$; 10×46 kpc) of M 31 resulting from the MAGPHYS fit to the photometric measurements: GALEX FUV and NUV, SDSS griz, Spitzer IRAC and MIPS $24 \mu\text{m}$, and all Herschel bands (except SPIRE $500 \mu\text{m}$). The middle panel shows an example extinction curve ($R_V = 3.1$; Cardelli et al. 1989). The bottom panel presents the attenuated energy from MAGPHYS in the $91.2\text{--}206.7$ nm (UV_{att}), and $91.2\text{--}3000$ nm wavelength range. Conceptually, the bottom panel is $\nu F_\nu^{att} = (1 - \exp(-\tau_\nu)) \times \nu F_\nu^o$, however the extinction by dust (τ_ν) in MAGPHYS is defined differently (see Section 3.2.3.1).

more star formation. This significant emission poses the puzzling question: what is powering the [C II] emission in the bulge if it is not star formation? What dominates the energy budget of the diffuse ISM in the bulge?

A clue may be seen in the bottom panel of Figure 3.4, which shows the [C II]/TIR ratio as a function of the gas-phase metallicity (directly related to the galactic radius). Based on our SLIM fields we expect the [C II]/TIR ratio to decline with increasing metallicity. However, given the high metallicity expected in the bulge, the observed [C II]/TIR ratio is in excess. This is additionally surprising given the dust in the bulge is predominantly heated by optical light from old stars, from which photoelectrons cannot be ejected.

The stronger than expected [C II]/TIR suggests that in addition to photoelectric heating, some other mechanism contributes non-negligibly to gas heating in the bulge. This mechanism could also explain the observed anomalous [C II] emission. We consider this

possibility by looking into the total energy budget in the bulge based on the existing multiwavelength observations.

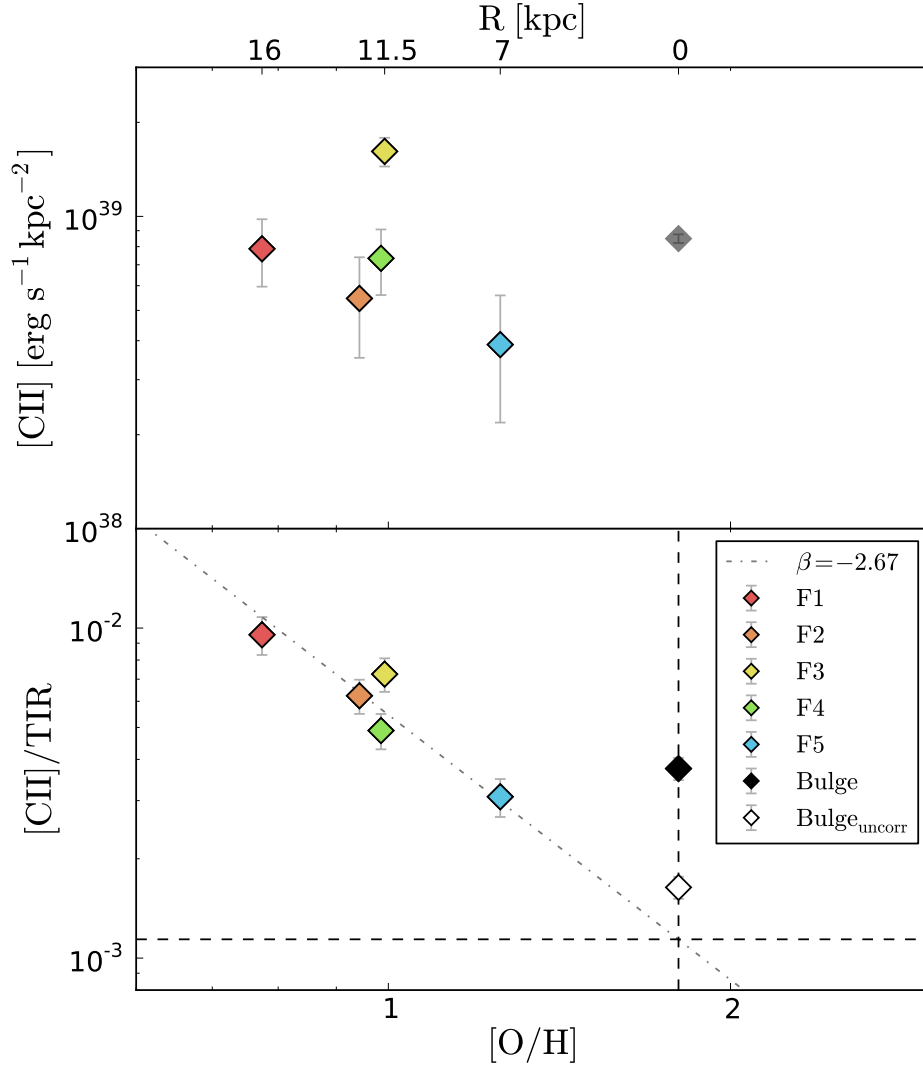


FIGURE 3.4: The average [C II] (top panel) and the average [C II]/TIR surface brightness ratio (an often used proxy for gas heating efficiency) versus Zurita & Bresolin (2012)'s gas phase metallicity (extrapolated value in the bulge; bottom axis) and galactocentric radius (top axis). The legend is common for both panels and it is located in the bottom panel. The colored diamonds show the average SLIM results from Kapala et al. (2015), and the black diamond indicates the average values in the bulge (note that the uncertainty is smaller than the point symbol in the top panel). The white diamond (bottom panel) shows the implications of naively applying a TIR approximation that includes the $8 \mu\text{m}$ filter without correcting for the stellar contribution to this band (contaminated by the stellar emission, see Appendix 3.A).

3.4 TOTAL ENERGY BUDGET IN THE BULGE

To investigate the integrated energy budget in the bulge, we define a 1 kpc radius circle centered at the nucleus ($00^h42^m44.^s35$, $+41^\circ16'08''.60$; J2000)³. Within this circle, we assess the ability of various heat sources to contribute to gas heating (X-rays, shocks, photoelectric heating, photoionization). We note that due to M 31's high inclination (70° ; Dalcanton et al. 2012) we likely overestimate the dust emission in the bulge due to the inclusion of disk emission, and therefore we consider the results as upper limits.

As we established in Section 3.1, the bulge of M 31 is a good case study of the ETG-like environment. The key components that we take into account in the [C II] emitting gas energy balance in the bulge are:

$$L_{gas}([CII]) = L_{X-ray} + L_{FUV} + L_{ion} + L_{mech} + L_{CR}, \quad (3.3)$$

where the gas cooling via [C II] 158 μm emission line, $L_{gas}([CII])$, is balanced by the heating terms: L_{X-ray} —X-rays, L_{FUV} —FUV (stellar emission 6 – 13.6 eV), L_{ion} —photoionizing photons (stellar emission above 13.6 eV), L_{mech} —mechanical (includes shocks and turbulence), L_{CR} —cosmic rays.

Each heating component has a certain amount of energy available, and an associated with this heating mechanism efficiency defined as the fraction of the energy carried by this heating component transferred to the absorber (e.g., gas).

3.4.1 GAS COOLING

The ISO observations of the [C II] line probe gas emission only along the major axis. We estimate that the average [C II] surface brightness in the inner 1 kpc is $\sim 9.2 \times 10^{38} \text{erg s}^{-1} \text{kpc}^{-2}$ giving an integrated [C II] luminosity of $2.9 \times 10^{39} \text{erg s}^{-1}$ assuming that the emission in the bulge is azimuthally symmetric.

3.4.2 PHOTOELECTRIC HEATING

In order to estimate the FUV photons reservoir, we use the SED fitting code `MAGPHYS` (da Cunha et al. 2008) to the stellar and dust emission integrated photometry in the *GALEX*, *SDSS*, *Spitzer* and *Herschel* filters. Note again, that UV_{att} (defined in Section 3.2.3.2) is likely overestimated due to projection effects.

UV_{att} give us an approximation of the energy input from stars to the ISM in the 6 – 13.6 eV (PE) energy range (see Figure 3.3). In the bulge we determine an average

³Based on NED data and references therein.

$UV_{att} = 1.02 \times 10^{41} \text{erg s}^{-1} \text{kpc}^{-2}$ ($L(UV_{att}) = 3.20 \times 10^{41} \text{erg s}^{-1}$). We define an approximation of the photoelectric heating efficiency as:

$$\epsilon_{PE}^{UV} = \frac{[CII]}{UV_{att}}, \quad (3.4)$$

the ratio of gas heating (approximated by the [C II] emission as the dominant gas coolant) to the absorbed FUV (approximated by the UV_{att} – an estimate of total energy available for heating in the PE energy range). The ϵ_{PE}^{UV} is close to the photoelectric heating efficiency the ratio of gas heating to the grain FUV absorption defined by Tielens (2005) although we need to approximate total gas heating by [C II] emission, and UV_{att} is averaged over grain size and charge distributions. Tielens (2008) theoretically estimates photoelectric heating efficiency as proportional to the grain ionization rate over the recombination rate, and finds theoretical values $\epsilon_{PE}^{th} \sim 0.1 - 4\%$ (see the right panel in Figure 1.3).

There is another often used approximation of the PE heating efficiency defined as the ratio of gas heating (via photoelectrons) to total dust heating (via ultraviolet and optical photons), $\epsilon_{PE}^{dust} = [CII]/TIR$, for details see Mochizuki (2004). It is based on observable properties, the neutral gas cooling can be measured by FIR lines as it is dominated by [C II] 158 μm (in low density regions; e.g. Wolfire et al. 2003) and [O I] 63 μm (in high density regime; e.g. Kaufman et al. 1999) emission lines, while dust cooling can be measured by integrating its continuum emission. However, note that this approximation is further from the theoretical definition as it is insensitive to the ratio of the dust heating via soft photons (transferring energy only to dust) compared to gas heating via PE photons (transferring energy only to both dust and gas).

Finally, we apply typical PE heating efficiency values $\epsilon_{PE}^{th} = 0.1 - 4\%$, and estimate the [C II] emission generated by PE heating, $[CII]_{PE} = 3.20 \times 10^{38} - 1.28 \times 10^{40} \text{erg s}^{-1}$. This means that [C II] emission can be generated via PE effect, but only at high efficiencies of $\epsilon_{PE}^{UV} \gtrsim 1\%$.

3.4.3 PHOTOIONIZATION HEATING

Due to the high optical depth of EUV ($> 13.6 \text{eV}$) photons, only rarely can we directly measure the ionizing photon luminosity. Rather, we use hydrogen recombination line emission, such as $H\alpha$, that directly traces the ionizing photons absorbed by the ISM. There is no spectroscopic $H\alpha$ data available in the bulge of M 31, therefore we use narrowband $H\alpha$ imaging from Devereux et al. (1994).

In order to correct these narrowband $H\alpha$ images for the [N II] contribution, we use Ciardullo et al. (1988) spectroscopic observations from the Palomar 5 m telescope that resolve these two lines. The ratio of [N II] to $H\alpha$ lines was measured along the major axis within the inner 1' and found to have an average value of $[NII]/H\alpha = 1.85$. We use this average value to remove contaminant [N II] emission from the narrowband observations. Due to

the lack of spectroscopic measurements outside of the $1'$ galactocentric radius, we apply the same value to correct for [N II] contribution within $4.4'$, understanding that it is likely to overestimate the [N II] contribution, as the [N II]/ $H\alpha$ tends to decrease outwards (Ciardullo et al. 1988). Therefore, the corrected for [N II] contamination $H\alpha$ flux is should be treated only as a lower limit of $H\alpha$ emission in the bulge. From measurements by Ciardullo et al. (1988) in optical ($A_B \lesssim 0.3$), by Melchior et al. (2000) in radio (low molecular gas estimates), by Groves et al. (2012) and Draine et al. (2014) in infrared (low dust mass estimates) we infer that the extinction in the bulge is negligible. Using the same 1 kpc circular aperture as before we integrated the total corrected $H\alpha$ image finding an average $H\alpha$ surface brightness of $1.68 \times 10^{39} \text{ erg s}^{-1} \text{ kpc}^{-2}$, and a total $H\alpha$ luminosity of $5.29 \times 10^{39} \text{ erg s}^{-1}$.

We aim to estimate $[\text{C II}]_{ion}$, the [C II] emission generated in the ionized phase. We explore ITERA models (Groves & Allen 2010) at solar metallicity, and a single burst star-formation history (resulting in old stellar populations consistent with the observed populations in the bulge) in the Levesque et al. (2010) starburst models. In order to get upper limits on $[\text{C II}]_{ion}$, we assume low a density regime ($n = 10 \text{ cm}^{-3}$), such that the gas is below the critical density of [C II] in the ionized phase ($n_{crit} \sim 50 \text{ cm}^{-3}$), and $[\text{C II}]_{ion}$ will be relatively bright. We find from these models that $[\text{C II}]_{ion}/H\alpha$ can be as high as one for typical diffuse ISM, meaning $[\text{C II}]_{ion}$ could be as high as $1.68 \times 10^{39} \text{ erg s}^{-1} \text{ kpc}^{-2}$. The assumption about the low density is supported by low extinction, and the fact that $H\alpha$ emission is diffuse with no identified H II regions in the bulge. It is possible then, that a significant fraction of [C II] emission arises from the ionized phase $[\text{C II}]_{ion} = 5.29 \times 10^{39} \text{ erg s}^{-1}$.

3.4.4 SHOCKS/TURBULENCE AND X-RAY HEATING

Bogdán & Gilfanov (2008) estimated the total energy that goes from Type Ia supernovae into the ISM in the bulge of M 31 is $L_{sh} \sim 1.5 \times 10^{40} \text{ erg s}^{-1}$. The problem is that we do not know how this mechanical energy is divided into gas heating versus dynamical driving (needed to explain observed outflows along the minor axis). Potentially, there is more than enough energy available from shocks, but it needs to be distributed among the hot gas at $\sim 10^6 \text{ K}$ that is emitting soft X-rays, ionized gas, outflows, and most interestingly for us the [C II] emission generated by shocks, $[\text{C II}]_{shock}$. From observations of the the Hickson compact group (HCG) of galaxies, Alatalo et al. (2015) find that the observed $[\text{C II}]/L_{FIR}$ ratio in HCG 57d is too high to be explained by the modelled photoelectric heating in PDRs alone. They consider elevated $[\text{C II}]/L_{FIR}$ due to contribution from the ionized gas or from shock heating of the diffuse gas colliding with the denser molecular gas in a companion galaxy HCG 57a. However, from Meijerink et al. (2011) modelling we learn that the shock heating influence on the [C II] line intensity is irrelevant for the high density and high stellar radiation fields models ($n = 10^{5.5} \text{ cm}^{-3}$ and $10^5 G_0$). The modelled [C II] line intensity is constant for three mechanical heating values Γ_{mech} equal zero, 3×10^{-18} and $2 \times 10^{-17} \text{ erg s}^{-1} \text{ cm}^{-2}$. Thus the shock heating contribution to generate [C II] emission should be even less important for low density regime that we observe in

the bulge.

There is also a hard, X-ray component, that shows a similar spatial distribution to the stars (traced by K-band light), indicating its star-related origins. Bogdán & Gilfanov (2008) associated this X-ray emission with the old stellar population, similar to the Galactic ridge emission in the Milky Way (the unresolved X-ray emission concentrated in the central parts of the Galaxy, coincident with its plane; Worrall et al. 1982). They postulate that it is a cumulative emission of numerous weak unresolved stellar sources (cataclysmic variables and active binaries). The total broad-band (0.5 – 10 keV) X-ray luminosity is $L_{Xray} \sim 3 \times 10^{38} \text{erg s}^{-1}$ (Bogdán & Gilfanov 2008).

The X-ray heating efficiency (i.e. ϵ_{Xray}) in X-ray dominated regions (XDRs) is typically 10 – 50% (Meijerink et al. 2007). Even if we assume ϵ_{Xray} as high as 50%, the resulting $[\text{C II}]_{Xray}$ is only $\sim 1.5 \times 10^{38} \text{erg s}^{-1}$, therefore X-rays can be responsible only for a small fraction of the total [C II] emission. However, in the bulge the efficiency, ϵ_{Xray} , is likely much lower than 50% due to the lower density $n \sim 10^{1-2} \text{cm}^{-3}$ than used in typical XDR models ($n \sim 10^{4-5} \text{cm}^{-3}$).

3.4.5 COSMIC RAYS HEATING

Ögelman et al. (2011) used the archival data from the *Fermi*-LAT all-sky survey and estimated that M 31 is ~ 20 times more luminous than the MW at cosmic ray energies $E_{CR} > 100 \text{MeV}$. We refer to the results from Meijerink et al. (2011) modelling to assess CR heating contribution to the [C II] emission. They assume the CR rates in the MW $\xi_{CR}^{MW} = 5 \times 10^{-17} \text{s}^{-1}$, thus from Ögelman et al. (2011) we infer $\xi_{CR}^{M31} = 10^{-15} \text{s}^{-1}$. The modelled by Meijerink et al. (2011) [C II] line intensity is constant with changing ξ_{CR} from 5×10^{-17} to 5×10^{-15} in the high density and high radiation fields models ($n = 10^{5.5} \text{cm}^{-3}$, $10^5 G_0$), while [C II] line intensity increases by $\sim 30\%$ for $\xi_{CR} = 5 \times 10^{-15}$ compared to 5×10^{-17} in the low density and low radiation field models ($n = 10^3 \text{cm}^{-3}$, $10^3 G_0$). Thus, we conclude that the $[\text{C II}]_{CR}$ can contribute $\lesssim 30\%$ to the total [C II] emission in the bulge of M 31.

3.4.6 ENERGY BALANCE IN THE BULGE OF M 31 SUMMARY

The energy balance in the bulge is summarized in Table 3.2, where we provide all estimated upper limit contributions to [C II] emission in the 1 kpc circle in the bulge of M 31. From our calculations it is clear that even though there is little star formation, there is sufficient UV flux in the bulge that photoelectric heating can provide enough energy to power the observed [C II] emission (assuming high values of the PE efficiency), however, this UV flux is generated by evolved stellar populations (Rosenfield et al. 2012). Nevertheless, the observed H α suggests that there is sufficient photoionization that [C II] could also arise purely from ionized gas, given reasonable ISM conditions. Other mecha-

nisms such as cosmic rays and X-rays may contribute but cannot be the dominant heating mechanisms.

TABLE 3.2: Contributions of the heating mechanisms to generate [C II] emission^a

Heating mechanism	Estimated upper limit contribution to [C II] emission	
	L [erg s ⁻¹]	[%]
Photoelectric ^b	1×10^{40}	440
Photoionization	5×10^{39}	180
Cosmic rays	9×10^{38}	30
X-rays ^c	2×10^{38}	5
Shock/mechanical	1×10^{40}	negligible

^a Estimated in the 1 kpc circle in the bulge of M 31.

^b Assuming 4% PE efficiency.

^c Assuming 50% X-ray heating efficiency.

3.5 COMPARISON OF THE ENERGY BALANCE IN THE BULGE WITH THE SLIM FIELDS IN THE DISK

With some understanding the energy balance in the bulge, we now compare it with the regions in the disk where we have measured [C II], i.e. the SLIM fields. To determine the energy balance in these fields, we also model them with MAGPHYS. We compare the observed [C II] emission in the SLIM fields with the predicted emission from UV_{att} , and measure photoelectric heating efficiency $\epsilon_{PE}^{UV} = 13.5\%$ (see Figure 3.5). The required photoelectric heating efficiency exceeds considerably the typically used values ($\epsilon_{PE}^{th} \sim 0.1 - 4\%$), however it might be caused by the fact that MAGPHYS code is meant to fit SEDs at galactic, not at sub-galactic scales. We find the TOT_{att} to be underestimated by a factor ~ 1.34 in comparison with the total dust emission integrated directly from MAGPHYS dust spectrum. However, the application of this correction to TOT_{att} results in $\epsilon_{PE}^{UV} = 10.1\%$, namely still above typical values. The discrepancy of the $\epsilon_{PE}^{UV} \sim 10\%$ compared to $\epsilon_{PE}^{th} \lesssim 4\%$ could be explained by underestimated UV_{att} , nevertheless $\epsilon_{PE}^{UV} \times UV_{att}$ prediction of [C II] emission works as a relative measure, so Figure 3.6 holds true.

It is worth noting that in Kapala et al. (2015) we estimated the ionized contribution to the total [C II] emission to be small, based on [N II] 122 μm emission line observations (see Section 2.3.3). The other mechanisms discussed in the previous section which were found to be non-dominant contributors to the [C II] emission are even more negligible in the disk emission. This is demonstrated by the decreases cosmic rays and X-ray density in the disk (e.g., Bogdán & Gilfanov 2008). Given this we ignore the contributions of these mechanisms. Given the small ionized contribution to [C II] and the irrelevance of other mechanisms, we expect [C II] emission in these fields to be generated mostly by photoelectric heating. The important thing here is that there exists one constant photoelectric heating efficiency (i.e. $\epsilon_{PE}^{UV} = 13.5\%$) that can predict reasonably well the

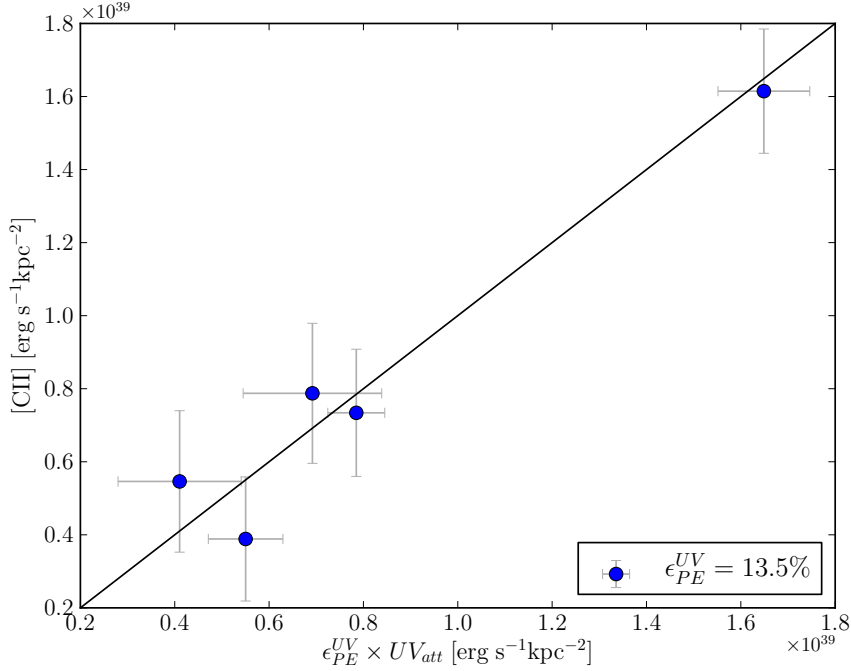


FIGURE 3.5: Observed [C II] emission in the SLIM fields versus predicted emission from UV_{att} based on MAGPHYS SED fitting and assuming photoelectric heating efficiency $\epsilon_{PE}^{UV} = 13.5\%$. The solid line indicates one-to-one relation.

observed [C II] emission in all of the SLIM fields (see Figure 3.5). If that is the case, the factor of 3 gradient across the disk in [C II]/TIR (see bottom panel in Figure 3.4) is *not* related to the PE efficiency. That raises the questions: what drives the [C II]/TIR gradient in the disk, and can this explain the anomalous [C II]/TIR ratio in the bulge in the bottom panel in Figure 3.4?

We find that the [C II]/TIR radial decline is related to the gradient in the UV_{att}/TOT_{att} (an estimate of the fraction of stellar energy that can contribute to gas heating, defined in Section 3.2.3.2) in the SLIM fields (see blue points in Figure 3.6). However, the value measured for the bulge (red point in Figure 3.6) diverges from the relation found in the disk. For the calculated UV_{att}/TOT_{att} ratio in the bulge, the [C II]/TIR ratio seems too high. The high value of the [C II]/TIR in the bulge is surprising, because the soft stellar radiation field (optical; see Figure 8 in Groves et al. 2012) should increase the relative amount of the energy absorbed by dust comparing to gas, therefore we expect [C II]/TIR ratio to lie below the values measured in the disk. The remaining explanations are that (1) a significant fraction of the [C II] emission in the bulge is generated by other heating mechanisms than photoelectric effect as discussed in Section 3.4; (2) the photoelectric heating efficiency ϵ_{PE}^{UV} is considerably higher in the bulge than in the disk, which is also possible, but with the currently available data set there is no way to evaluate ϵ_{PE}^{UV} .

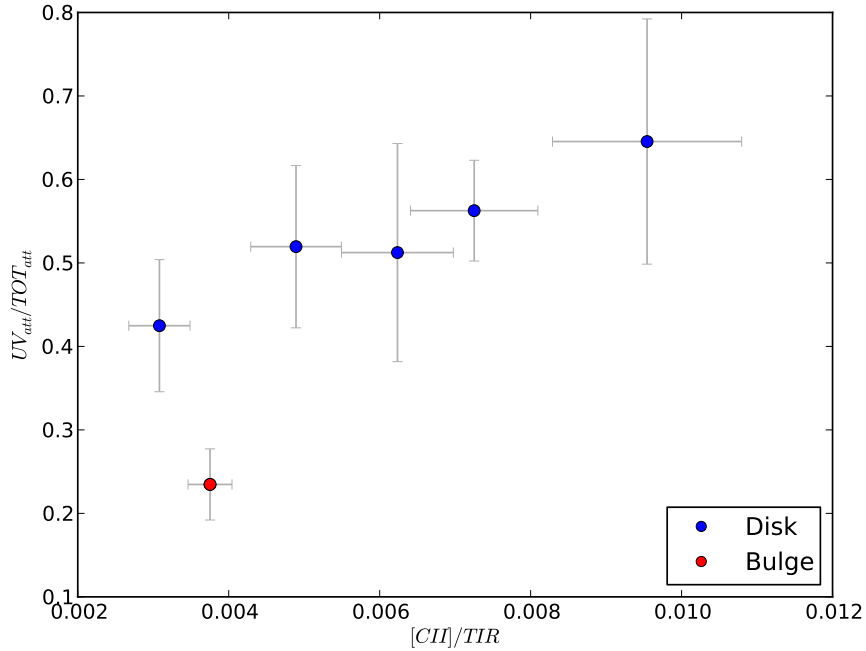


FIGURE 3.6: The $UV_{\text{att}}/TOT_{\text{att}}$ ratio as an estimate of the fraction of stellar energy that can contribute to gas heating versus the $[C\text{ II}]/TIR$ ratio as an often used proxy for gas heating efficiency.

3.6 DISCUSSION AND CONCLUSIONS

We investigate the energy balance in M 31 to understand the puzzling $[C\text{ II}]$ emission in the bulge (in comparison to the disk regions). The bulge of M 31 has a prominent $[C\text{ II}]$ emission ($\sim 3.5 \times 10^{38} - 1.6 \times 10^{39} \text{ erg s}^{-1} \text{ kpc}^{-2}$), comparable to the emission in our star-forming regions in the disk ($\sim 2 \times 10^{38} - 10^{40} \text{ erg s}^{-1} \text{ kpc}^{-2}$; Kapala et al. 2015). This is unexpected given the lack of ongoing star formation and the increased metallicity (see Section 3.1). The observed bulge $[C\text{ II}]/TIR$ ratio also seems in excess compared to the expected value from disk measurements (see Figure 3.4). The fact that the TIR from the bulge is generated by the soft, old stellar radiation heating, where Groves et al. (2012) showed that $\sim 25\%$ of the energy is absorbed at the FUV wavelengths (6–13.6 eV), and $\sim 75\%$ at longer wavelengths (optical), also goes against our predictions/expectations that $[C\text{ II}]/TIR$ should decrease. These observations give us a hint that $[C\text{ II}]$ might be generated, at least partially, by heating mechanisms that are different to those in the disk.

Based on multi-wavelength coverage from X-rays to radio, and energy balance calculation, i.e. using SED fitting, we achieved a better understanding of the heating sources of gas and dust in the bulge of M 31. We list here the potential heating sources and the estimated upper limits for energy transferred from each source to generate the observed

[C II] emission ($\sim 3 \times 10^{39} \text{erg s}^{-1}$):

- photoelectric $\lesssim 1 \times 10^{40} \text{erg s}^{-1}$ ($\lesssim 440\%$)
- photoionization $\lesssim 5 \times 10^{39} \text{erg s}^{-1}$ ($\lesssim 180\%$)
- cosmic rays $\lesssim 9 \times 10^{38} \text{erg s}^{-1}$ ($\lesssim 30\%$)
- X-ray $\lesssim 2 \times 10^{38} \text{erg s}^{-1}$ ($\lesssim 5\%$)
- shock/mechanical $\lesssim 1 \times 10^{40} \text{erg s}^{-1}$ (\sim negligible)⁴

Thus, the photoelectric heating mechanism could be the largest contributor to gas heating (where FUV flux is generated by evolved stellar populations), however photoionization and cosmic rays heating mechanisms may contribute to the observed [C II] “excess” in the bulge.

We showed that we can predict [C II] emission in the SLIM fields in the disk of M 31 based on the estimated fraction of the stellar energy that contributes to gas heating ($\epsilon_{PE}^{UV} \times UV_{att}$) with a constant photoelectric heating efficiency ($\epsilon_{PE}^{UV} = 13.5\%$). The photoelectric heating efficiency constancy is also supported by fact that [C II] works as a SFR tracer in each SLIM field despite the factor of 3 gradient in the [C II]/TIR found between these fields (Kapala et al. 2015). We explored potential drivers of the observed gradient across the disk in [C II]/TIR (other than the ϵ_{PE}^{dust}) and we found that the attenuated UV energy relative to the total attenuated energy (UV_{att}/TOT_{att}) correlates well with the [C II]/TIR ratio. Our conclusion from this is that it is the soft photon heating of dust (heating via photons less energetic than 6 eV, that cannot contribute to PE heating) that is driving the variation in the [C II]/TIR ratio across this disk. That is, TIR is varying much more strongly across the disk than [C II] (as seen in a comparison of the top and bottom panels in Figure 3.4) and that this is driven by the relative increase of heating of dust by photons that cannot eject photoelectrons (as measured by UV_{att}/TOT_{att}).

In the bulge we observe an “excess” of the [C II] emission which can be explained by other mechanisms that contribute to the gas heating in addition to the PE heating that dominates in the disk. The fact that UV_{att}/TOT_{att} fails to predict the observed [C II]/TIR ratio in the bulge can be consistently explained by additional to PE heating mechanisms powering [C II]. While our work suggests that an ionized gas contribution to [C II] is the most likely additional contributor to the [C II] emission, our study of the heating mechanisms in the bulge does not allow us to conclusively assign a fraction of the [C II] emission to each heating mechanism. A possible way to resolve this is to spatially resolve the [C II] emission such that we can assign the [C II] to the heating mechanisms which have different spatial distributions in existing observations. We have successfully proposed for SOFIA FIFI-LS observations to do exactly this, and will report this in later work.

⁴The estimate of the total energy in shocks is given, not the estimate of the ‘transferred’ energy. However from Meijerink et al. (2011) modelling we argue that the shock heating influence on [C II] line intensity is irrelevant, especially in a case of diffuse ISM of M 31’s bulge.

One of the main conclusions for this work is that $[C\ II]/TIR$ ratio (ϵ_{PE}^{dust}) appears to fail as an approximation of the photoelectric heating efficiency in M31. We propose that a better method is to use a SED fitting technique to derive a more precise estimate of the energy absorbed by dust in the PE heating wavelength range (UV_{att}), that together with the $[C\ II]$ emission allows us to determine the “true” photoelectric efficiency:

$$\epsilon_{PE}^{UV} = \frac{[C\ II]}{UV_{att}} \quad (3.5)$$

We plan to explore further the applications of the SED fitting method in energy balance studies in larger galaxy samples. For example, we calculated the UV_{att}/TOT_{att} across M31 in 1 kpc apertures (dashed circles in Figure 3.1). The resulting UV_{att}/TOT_{att} is shown in Figure 3.7, along with the corresponding SED fits in Appendix 3.B. There is a hint of the overall radial trend in UV_{att}/TOT_{att} , however the scatter is considerable.

It is essential to remember that none of the $[C\ II]$ emission in the bulge of M31 is powered by the star-formation. If one tries to use $[C\ II]$ emission to estimate SFR in the bulge, one would get $SFR \sim 0.003 - 0.006 M_{\odot} \text{yr}^{-1}$, overestimating the negligible star formation observed, and demonstrating clearly that naively applying SFR estimates without corrections is wrong.

3.A A CAVEAT ABOUT TIR PRESCRIPTIONS/APPROXIMATIONS IN A BULGE

TIR emission is generally defined as the integrated dust emission between 3 and 1000 μm (e.g., Dale & Helou 2002). In practice, we typically have photometry measurements in few IR bands, therefore many empirically derived linear combinations of multiband observations approximating TIR integral have been proposed (Draine & Li 2007; Dale & Helou 2002; Galametz et al. 2013). Due to the lower resolution of the longer wavelength bands (e.g., *Herschel* 500 μm with a FWHM of 36''), the TIR is often based purely on the shorter wavelength bands.

One of the commonly used prescriptions is derived by Draine & Li (2007), based on 8, 24, 70 and 160 μm bands. It has been proven to be very useful in the disk of M 31 (Kapala et al. 2015), however, we show that in case of a prominent bulge like M 31 it overestimates total dust emission.

The reason for an overestimation is that shorter wavelengths are severely affected by stellar light, e.g., 8 μm band is comparably bright as a peak of TIR emission at $\sim 100 \mu\text{m}$ (see Figure 3 in Groves et al. 2012).

Given this strong contamination, we have explored different empirical calibrations of the TIR from Galametz et al. (2013) which do not include wavelengths shorter than 24 μm . We find the TIR determined using the relation from Draine & Li (2007) is overestimated by a factor 2.5 – 3.3 in the central 250 pc aperture relative to 4 different prescriptions from Galametz et al. (2013).

Note, that this caveat is not an issue for global measurements (of non-AGN dominated galaxies), where bulge IR emission produced by the bulge is a small fraction of the global value. However, it is likely to be important for early type galaxies. The best solution to avoid this caveat is simultaneous modeling of stellar and dust emission (da Cunha et al. 2008), or applying stellar templates to match dust emission approximated by more complex model, when FUV–optical observations are not available (Draine & Li 2007; Draine et al. 2014)

3.B MAGPHYS SED MODELING ACROSS M 31

We use MAGPHYS SED modeling across the galaxy along the major axis in 1 kpc apertures (dashed circles in Figure 3.1) to derive the overall trend of UV_{att}/TOT_{att} with galactocentric radius in Figure 3.7. We color-coded the points with dust mass surface density (extracted from Draine et al. 2014, maps) to indicate the structure of the galaxy (e.g., spiral arms). We present all SED fits in Figures 3.8–3.12. In the future work, we plan to use the $\epsilon_{PE}^{UV} \times UV_{att}$ to predict [C II] emission in the disk of M,31.

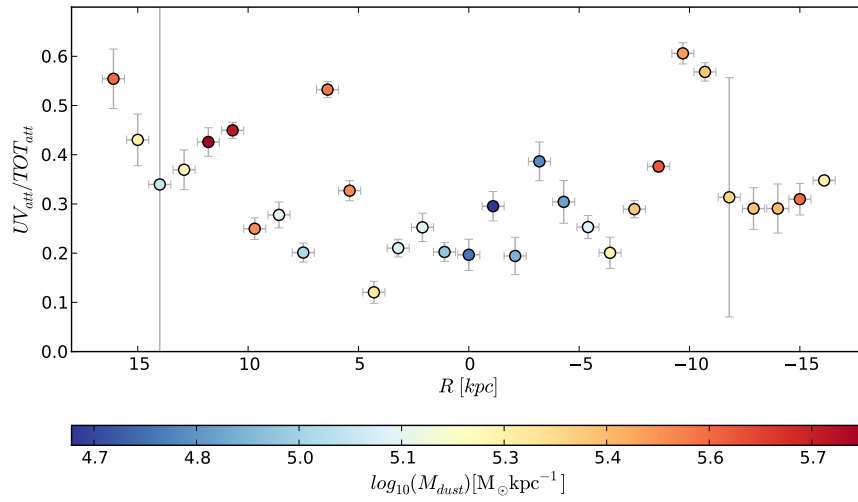


FIGURE 3.7: UV_{att}/TOT_{att} versus galactocentric radius (negative values indicate SW direction). The points are color-coded with dust mass surface density (M_{dust} extracted from Draine et al. 2014, maps)

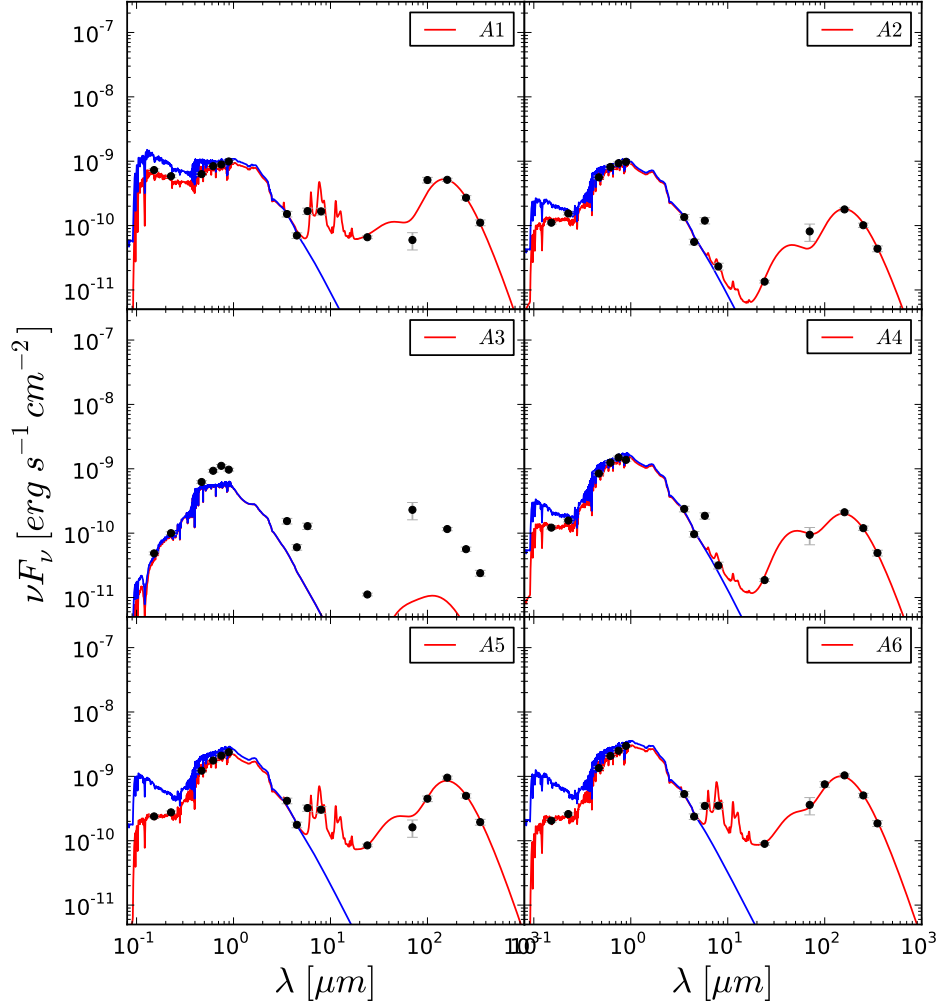


FIGURE 3.8: The SED across M31 along the major axis, measured within 1 kpc ($4.405'$) apertures A1–A6. The fluxes (GALEX FUV and NUV, SDSS u, g, r, i and z, Spitzer IRAC and MIPS24, and the five Herschel bands excluding SPIRE 500). Note that A3 is an extremely faint region, and MAGPHYS fitting fails there.

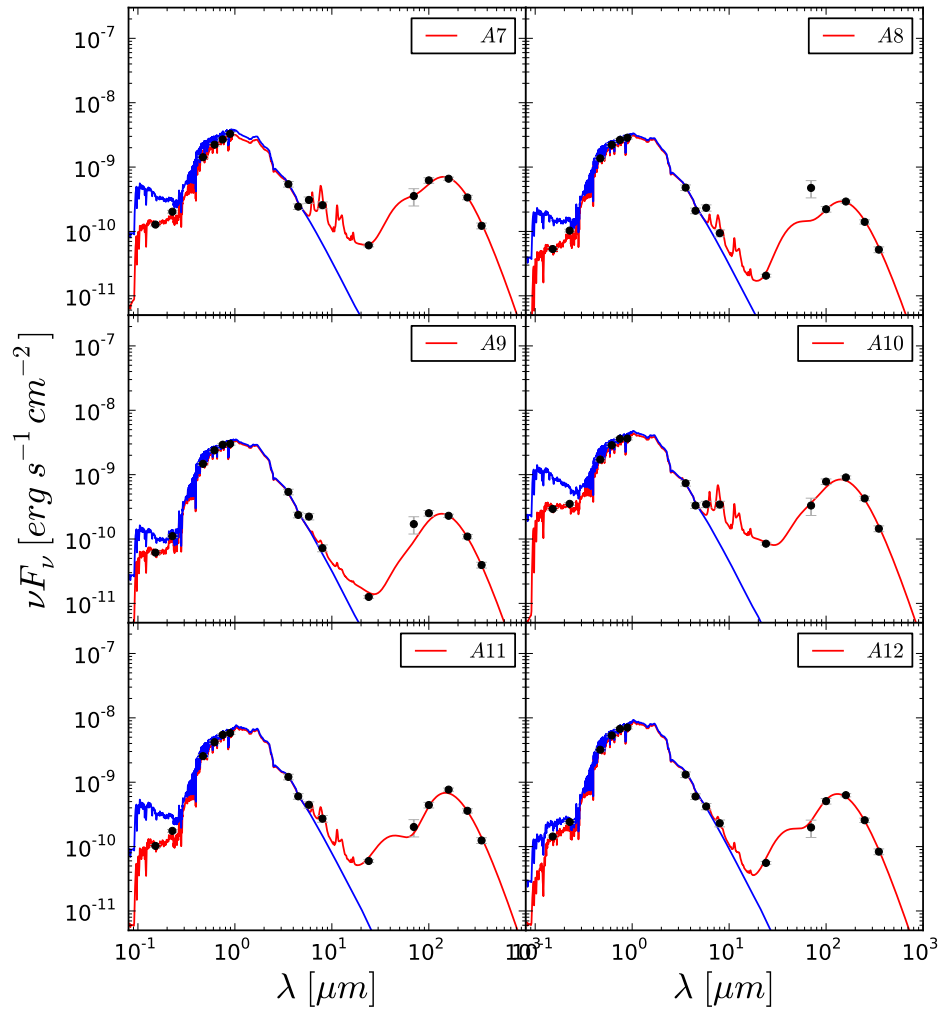


FIGURE 3.9: As in Figure 3.8, but for different apertures A7–A12 as labelled.

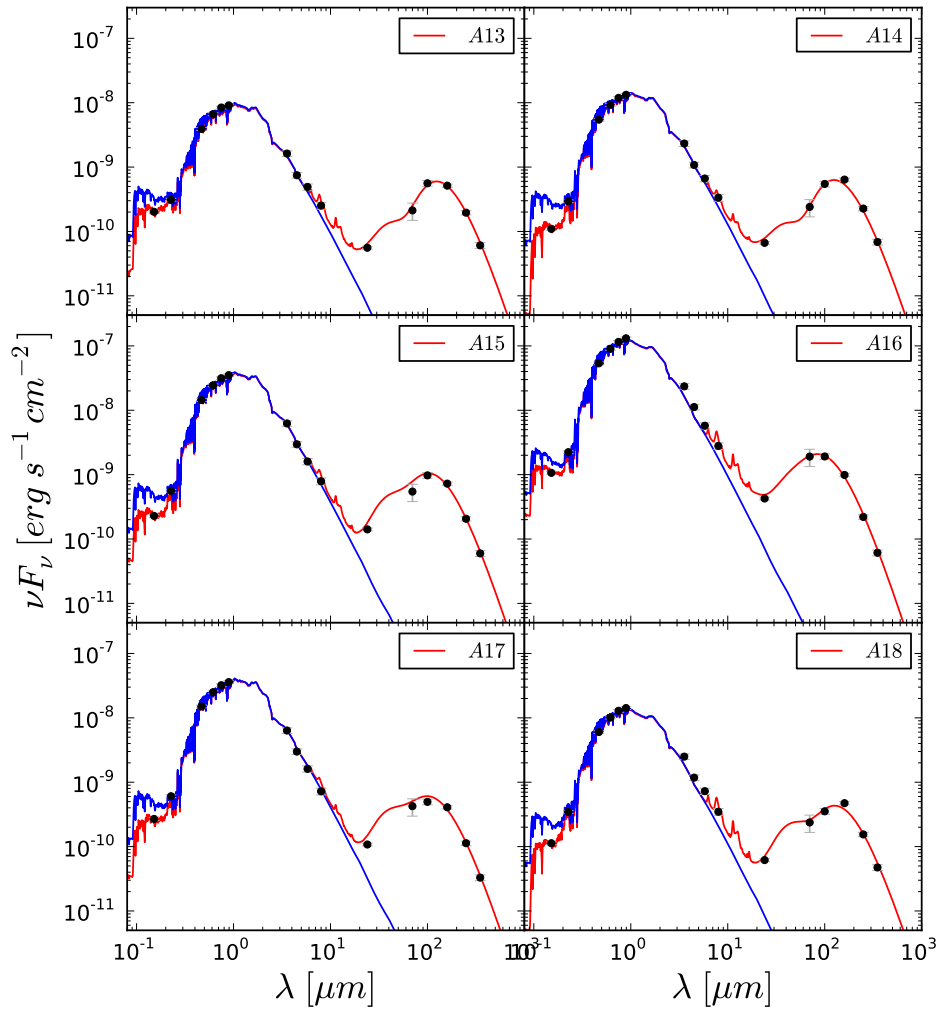


FIGURE 3.10: As in Figure 3.8, but for different apertures A13–A18 as labelled.

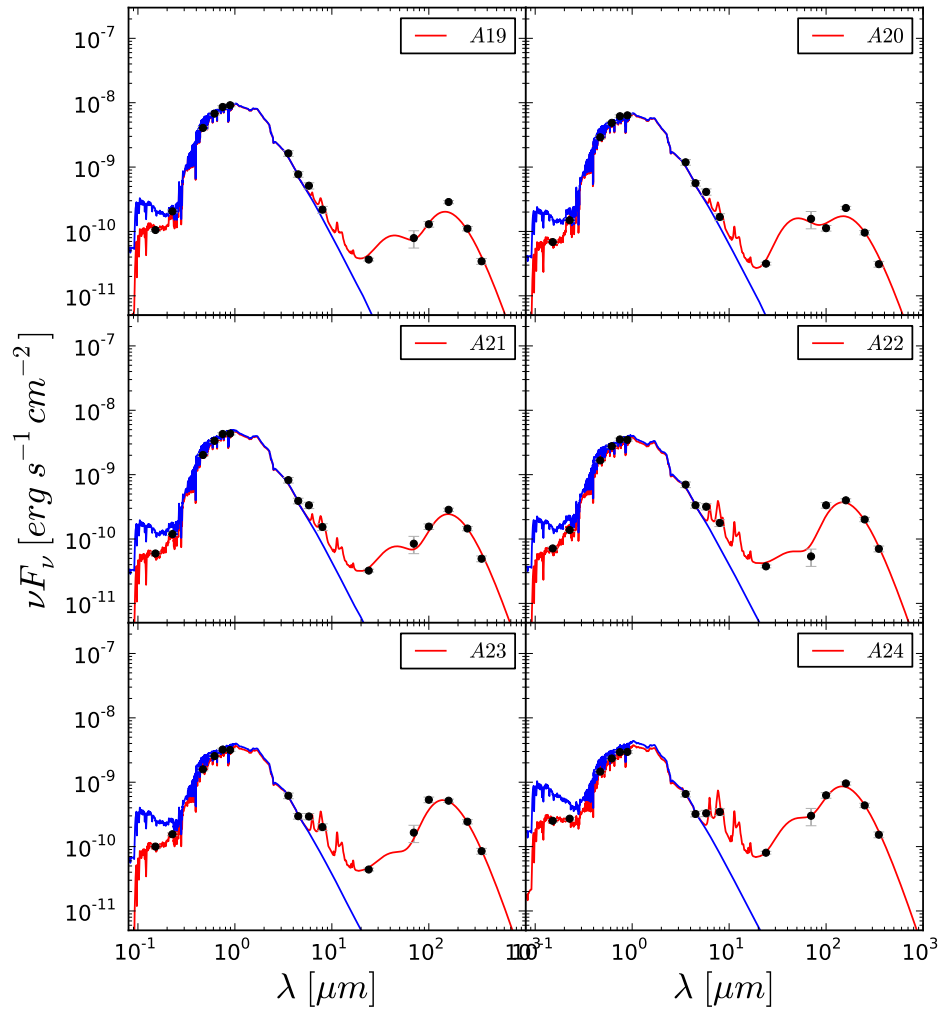


FIGURE 3.11: As in Figure 3.8, but for different apertures A19–A24 as labelled.

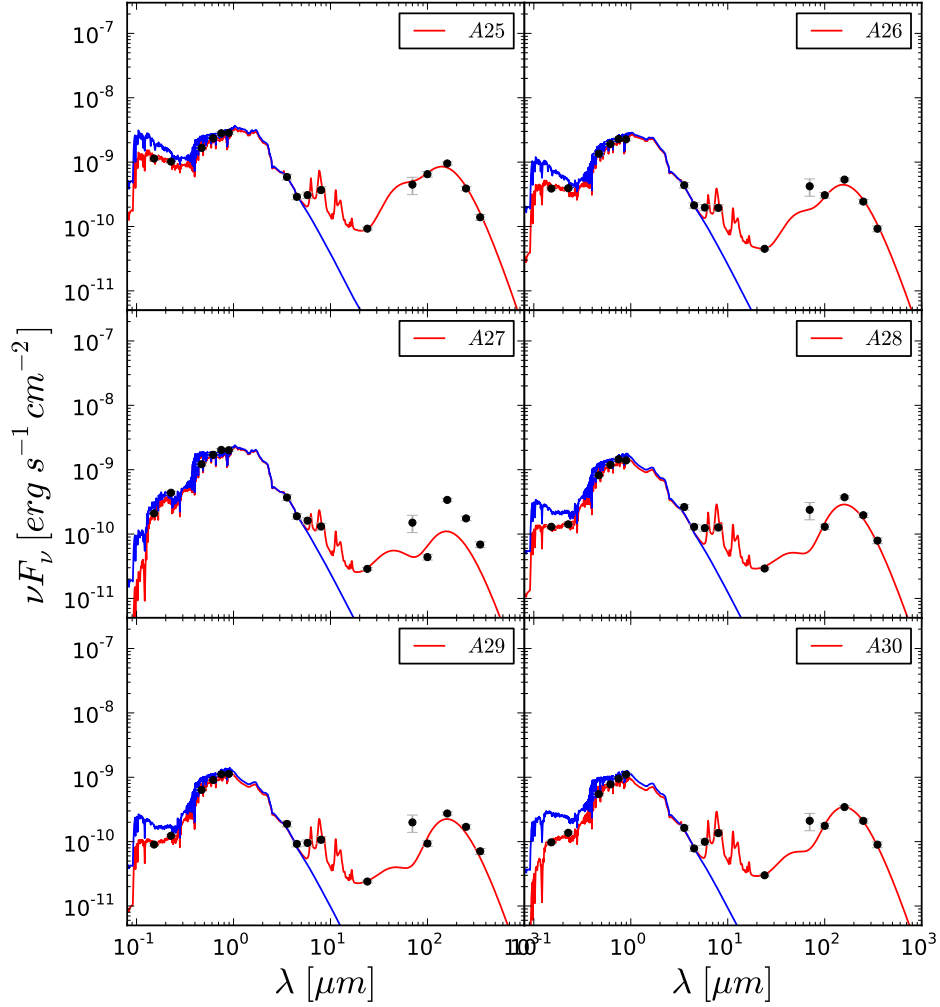


FIGURE 3.12: As in Figure 3.8, but for different apertures A25–A30 as labelled. Note that A27 is an extremely faint region, and MAGPHYS fitting fails there.

CHAPTER 4

STELLAR POPULATIONS RESPONSIBLE FOR HEATING THE ISM IN M 31

4.1 INTRODUCTION

The interstellar radiation field (ISRF) seen by the ISM is the combination of the spectra of all stars in a galaxy, extinguished by dust and weighted by the inverse square of their distance. In some cases, the radiation field is dominated by a nearby star, e.g. in H II regions powered by the OB stars within the regions. In other cases, the radiation field is not dominated by a single star, but so called “diffuse ISRF” that results from a superposition of the radiation from stars of all ages and spectral types (Telesco 1999). The ISRF is the dominant heating source of the diffuse ISM (i.e. of the IR-cirrus), and as such drives the thermal state and phase structure of the ISM. Thus, it is vital that we know the strength and spectral shape of the ISRF to understand the energy balance within galaxies. Due to this superposition of factors, the strength and spectral shape of the ISRF is strongly dependent upon the local and global star formation histories, and the geometry of stars and dust. Therefore the ISRF will significantly vary across a galaxy’s disk.

Measurements of the strength of the ISRF, in particular the optical-UV light responsible for most ISM heating, can be done directly via the integration of the spectra of all stars, or indirectly via the re-emitted IR light from dust that has absorbed the the ISRF (see Section 1.4). Previous direct measurements of ISRF were only done in the solar neighborhood, because of the observational limitations – the ability to resolve individual stars has been limited until recently to the Milky Way and bright stars in nearby galax-

ies. These stellar measurements done in nearby galaxies have been insufficient for the determination of the ISRF, because it is not necessarily dominated by those brightest stars. Indirect methods using dust emission have to make major assumptions in order to infer the average intensity of the radiation field from the temperature of the grains in equilibrium. The indirect method infers only the intensity, not the spectral shape of the ISRF. However, the indirect method has an advantage over the direct method, in that it does not require individual stars to be resolved, and thus can be applied in extragalactic studies.

The first attempt to measure the ISRF directly was by Habing (1968) who integrated the light of all visible stars (of earlier types than B9) in the local solar neighborhood to estimate the FUV interstellar radiation density in the range 912–2400 Å, as this had been suggested to be the dominant source of heating of the atomic interstellar gas. Since then, the ISRF has been modeled with simple (Mathis et al. 1983), and more complex ISRF models (time-dependent; Parravano et al. 2003). The latter work focuses on the H₂ dissociating radiation (912–1100 Å) and the radiation involved in photoelectric heating (912–2070 Å), because Parravano et al. (2003) argue that at a fixed mean density FUV radiation controls the amount of interstellar gas in the cold and warm neutral phases.

The indirect methodology to determine the ISRF from dust emission has been applied many times. Recently, using *Herschel* data in Galactic (e.g. by Bernard et al. 2010) and in extragalactic studies (e.g. in M 31 by Draine et al. 2014). The indirect method requires knowledge of the optical properties of dust grains (mass absorption coefficients, scattering cross sections, etc.) and the heat capacities of different grain materials. It also assumes an initial dust model with a specified physical nature of the dust (composition, geometry, and size distribution), that later gets adjusted to fit the observations (e.g., extinction, scattering, polarization, IR emission, and interstellar depletions). One of the physical dust models that has been proposed by Draine & Li (2007), includes mixture of large molecules polycyclic aromatic hydrocarbons (PAHs), graphite and amorphous silicate grains.

Recently, with the era of *HST*, we are able to resolve stars in other galaxies. The *HST* high resolution power and the Panchromatic Hubble Andromeda Treasury survey (PHAT; Dalcanton et al. 2012), enable us to apply both methods simultaneously in an external galaxy. We use a unique approach to directly constrain the ISRF intensity and spectral shape, based on ability to locate and model the spectral energy distributions (SEDs) of all of the relevant stars in M 31 from the PHAT photometric data. The outcome is spatially resolved spectra of the ISRF over a large area covering $\sim 1/3$ of M 31. In addition, the unprecedented resolution provided by the *Herschel Space Observatory*, give us high spatial resolution maps of the dust surface density and luminosity across the disk of Andromeda, providing detailed map of the dust heating, and thus the strength of the ISRF. Together, these observations give us an unprecedented insight into the total energy input and efficiency of this input into the ISM. In particular, in this Chapter we describe how we determine the UV ISRF, which is responsible for most of ISM heating.

In the following Sections, we explain our methodology (Section 4.2). We describe the

photometric data we use in section 4.3. In section 4.3.2 we present results from a preliminary study based on PHAT, and in the following section 4.5 we interpret these results. Finally, we discuss future directions (e.g. improving on M 31, using this methodology in other galaxies like M 33), and conclude in section 4.6.

4.2 METHODOLOGY

We aim to understand the fractional contributions of various stellar populations to the ISRF – and thereby, the ISM energy balance. By comparing the UV energy input we predict to the infrared emission, we aim to measure the typical scales on which this energy is absorbed by dust. Our objective is to dissect the ISRF, and we want to achieve that by stellar SED fitting in the M 31 galaxy, which offers an external view, but sufficient proximity to resolve individual stars.

The main steps in our methodology are:

1. using SED fitting to measure their unreddened spectra,
2. selecting all resolved stars in a region,
3. adding all these spectra to obtain the ISRF generated by the resolved stellar population
4. and correcting for incompleteness due to faintness limits, field star crowding, and stellar cluster crowding by adding in estimated spectra for the unresolved stellar populations from the star formation history

We explain each of these steps in more details below.

The PHAT survey has obtained HST near-UV to near-IR photometry of a few 10^8 stars across $\sim 1/3$ of the disk of M 31 (see Figure 4.2), enabling us to determine directly the ISRF in our nearby neighbor. PHAT gives us the ability to resolve individual stars (down to $\sim A0$ spectral type) and allows us to disentangle the effects of reddening and the intrinsic stellar properties by fitting their individual spectral energy distributions (see Figure 4.1).

By combining the inferred unreddened spectra of the stars in M 31, we gain knowledge of not only the intensity of the ISRF as a function of position through the galaxy, but also its spectral shape (that cannot be directly determined from using the dust methodology). The shape of intrinsic stellar SEDs give us a unique possibility to understand which stellar populations contribute most to the heating of the ISM, as the relative intensity of the radiation at different wavelengths affect the physical and chemical state of gas and dust. Additionally, by fitting the stellar SEDs we also obtain information on the

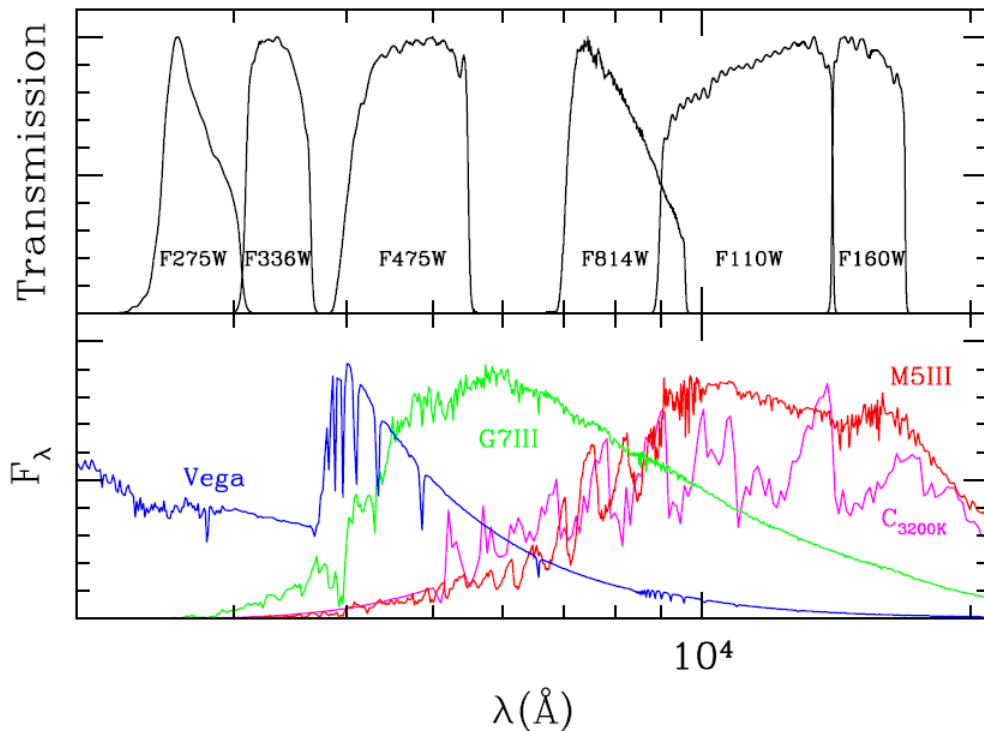


FIGURE 4.1: Relative transmission of the HST wide-bands used for PHAT observations as a function of wavelength are shown in the upper panel. Various stellar spectra are presented in the lower panel for comparison (a Vega A-star in blue, a G7III giant in green, an M5III giant in red and a carbon star with a 3200 K atmosphere in red. [Figure adapted from Dalcanton et al. (2012)]

extinction of the stars, providing unique maps of dust extinction curves (and therefore dust properties) in M 31.

Throughout this Chapter, we rely on the BEAST catalog, which provides the intrinsic parameters ($\log(g)$, T_{eff} , initial mass M_{birth}) for all stars (of earlier types than A0) along with their extinction. The details of the BEAST_v0 SED fitting technique are discussed in Section 4.3.2. We then select all stars from the BEAST catalog that lie in our region of interest. In particular, we concentrate on our SLIM regions (see Table 2.2) with corresponding *Herschel* spectroscopy. We also have the option to select specific stellar populations from the BEAST catalog, such as O-stars.

Once we locate subsample of stars that fall into our region of interest, we identify the full best fit stellar spectrum in the stellar library – the intrinsic (unreddened) stellar spectrum. Next, we convolve intrinsic stellar spectrum with the extinction curve (with fitted by BEAST_v0 A_V and R_V parameters), to obtain full best fit “observed” (reddened) stellar spectrum. Subsequently, we co-add all individual stellar and cluster spectra¹ in the

¹For now, we can only add cluster flux in the PHAT filters, as the full spectra are not available.

selected region/pixel.

The preliminary PHAT photometry is complete down to $\sim A0$ stars, therefore based on this photometry the BEAST_v0 catalog is “missing” flux from the stars that cannot be resolved but still contribute to the diffuse interstellar radiation field. We propose a way to assess the contribution of the unresolved sources to the ISRF, by using integrated photometry from FUV (*GALEX*) to NIR (*Spitzer* IRAC) to measure the total flux, which is the superposition of resolved, unresolved and scattered, plus background and foreground light. Once we correct for the background and foreground light, and subtract flux from all known resolved stars, we obtain upper limits on unresolved flux (as it still contains unknown contribution of scattered flux). As an additional constraint, we can also estimate the population of unresolved stars that contribute to the ISRF from star formation histories (SFHs) determined from the resolved stellar population, as described in Section 4.4.2.

In judging the portion of the ISRF that goes to the ISM heating (e.g. dust), we define the difference between unreddened and reddened stellar SEDs as “attenuated” flux. Especially, we are interested in estimating the amount of “missing” (absorbed and scattered) intrinsic stellar UV flux from the BEAST_v0 catalog. We integrate the SED from the previous step in a desired wavelength range (energy bin). We are most interested in the FUV wavelength range, as it is the radiation responsible for most dust heating and all photoelectric effect. This energy bin is typically dominated by massive OB stars, and we aim to learn how much energy comes from various stellar types (e.g. the short-lived O stars and the longer lived B stars). The final output/result is therefore UV_{att} – the UV stellar energy input into the ISM.

Once we know the intrinsic unreddened and observed reddened stellar SEDs we compare the ISRF to the dust heating (from dust emission) and gas heating (from $[C II]$, assuming heating equals cooling). In particular, we can re-evaluate indirect SFR tracers (e.g. $[C II]$, $H\alpha$, TIR, etc.) in light of our new knowledge about whether that re-radiated energy actually originated in young, massive stars. We can also look for correlations between distribution of stellar populations with tracers of ISM phases (e.g., CO – molecular, $H I$ – atomic, and $H\alpha$ – ionized), and judge how accurately our simplified picture of the ISM cycle delineated in Chapter 1 corresponds to observations.

4.3 THE SPATIALLY RESOLVED DATA

In this Section, we introduce the PHAT data set and the stellar SED fitting method that lie at the core of directly inferring the ISRF.

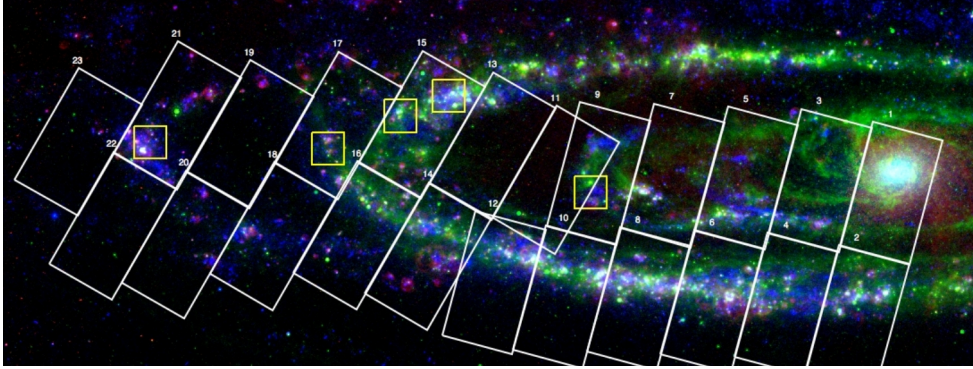


FIGURE 4.2: Three color image of M31, $24\ \mu\text{m}$, $H\alpha$ and Galex FUV. The image presents PHAT survey coverage, the 23 PHAT bricks are marked as white rectangles. Herschel SLIM regions are indicated as yellow boxes.

4.3.1 PHAT SURVEY

The PHAT survey obtained near-UV to near-IR photometry over $\sim 1/3$ of M 31 (see Figure 4.2). The observations were carried using the *Hubble Space Telescope* (HST) in 6 wide filters F275W, F336W, F475W, F814W, F110W and F160W. The PHAT footprint is made of 23 so-called “bricks” ($12' \times 6'.5$, $\sim 3 \times 1.5$ kpc), each consisting of 18 fields (each field has been observed in every filter at least twice). From these observations, photometry of over 10^8 individual stars has been measured (Williams et al. 2014), from the central regions to 20 kpc in the outskirts. The 6 filters presented in Figure 4.1 were carefully selected to give leverage to disentangle the effects of reddening and the intrinsic stellar properties by fitting the stellar SEDs. As we describe in Section 4.3.2, this allows each resolved star to be corrected for extinction and their intrinsic spectra determined.

TABLE 4.1: PHAT photometric properties

Radius ^b		PHAT 50% completeness magnitude limit ^a					
[kpc]	[$^\circ$]	F275W	F336W	F475W	F814W	F110W	F160W
0	0.0	25.0	24.5	23.5	22.5	19.0	18.0
5	0.37	25.0	24.5	26.0	25.0	22.0	21.5
10	0.73	25.0	24.5	27.0	26.0	23.5	22.5
15	1.10	25.0	24.5	27.5	26.5	24.5	23.5

^a Data from Dalcanton et al. (2012).

^b Galactocentric deprojected radius.

4.3.1.1 PHAT PHOTOMETRY & KNOWN *HST* ISSUES

All PHAT photometry was produced by the software package *DOLPHOT.v1.2* (Dolphin et al. 2002). Point spread function (PSF) fitting was used to measure the stellar photometry. Simultaneous fitting in all 6 bands means that any non-detections in any bands can be used as strict upper limit constraints in the stellar SED fitting.

Each PHAT photometric band is complete down to a certain magnitude, depending upon both the sensitivity of that band and the crowdedness of that region. Completeness can be assessed as a function of color and magnitude of the photometric catalogs using artificial star tests. By inserting “fake” stars with known properties (position, color and brightness), and proceeding as normal with the PSF photometry, one can estimate how many of these “fake” stars were recovered (e.g., 50% completeness means half were recovered).

As mentioned above, we also aim to assess the contribution of the unresolved sources to the ISRF, using integrated photometry from FUV, through to NIR wavelengths as upper limits. Our first choice in NUV to NIR wavelength range would be integrated photometry based on PHAT images. However, a set of known problems with *HST* photometry interfere with measuring integrated photometry, meaning that we must use *SDSS* images instead.

In optical and UV filters PHAT images can be affected by a number of different artifacts (see Dalcanton et al. 2012, for details). All of these artifacts are caused by bright stars, and appear in ACS/WFC and WFC3/UVIS cameras. Additionally, there are transient events (cosmic rays or “space debris” passing through the field), which usually can be flagged as cosmic-rays and masked, but it is impossible when only one exposure is available, which sometimes happen because of chip gaps in some instrument/camera. In the infrared, we find in our data that the illumination of $\sim 1/3$ of the WFC3/IR channel when pointed near a bright Earth limb leads to scattered light artifact.

One additional issue that complicates the M 31 integrated photometry is the diffuse background from Zodiacal light from the Milky Way, and even from the telescope itself. To correct images for this background, one needs to subtract measured background values from the images. No individual PHAT field extends off the galaxy, therefore we cannot measure and subtract correctly the background level. This is problematic since we cannot disentangle between unresolved starlight and background contribution to the smooth (diffuse) component. A second issue is that while stacking two exposures and matching/creating the mosaic from fields to bricks, the local background is not conserved. The background issues do not affect point source photometry, but they do change the integrated photometry in large apertures.

4.3.2 BEAST SED FITTING OF INDIVIDUAL STARS

The determination of intrinsic properties of individual stars is crucial in the process of directly inferring the UV radiation field. In this work, we considered stars more luminous than A0-type stars. For these stars, we infer their intrinsic properties through fitting their spectral energy distribution (SED). The technique we used has been developed and tested using observations from PHAT.

The details of this procedure are given in Gordon et al. (in prep., BEAST – the Bayesian Extinction and Stellar Tool), but we can briefly outline the procedure in this Section. For every single star in our selection, PHAT offers us 6 photometric measurements from UV to NIR. Each SED is then probabilistically compared with a large collection of stellar SED models that account for both stellar parameters (stellar birth mass M_{birth} , current mass M_* , effective temperature T_{eff} , logarithm of surface gravity $\log(g)$, radius R , luminosity L_* , metallicity Z_* and age)², and the extinction along the line of sight. The collection of templates is generated from the combination of the Castelli & Kurucz (2003) and TLUSTY Lanz & Hubeny (2003, 2007) stellar atmosphere models and Padova (Marigo et al. 2008) stellar evolution models. The final model grid is expanded with the addition of dust extinction, which in the current (BEAST_v0) catalogs was based on Fitzpatrick (1999) attenuation law where both A_V and R_V are free variables. Gordon et al. (in prep.) demonstrate that the six-filter near-UV to near-IR photometry from PHAT is sufficient to not only measure A_V , but also to constrain the selective extinction (R_V) which traces the growth and geometry of dust grains.

The BEAST gives as the best fit output an A_V , R_V and the intrinsic stellar properties, including the full spectrum for the star (even covering wavelength regions not observed). In particular, it give us the intrinsic spectrum i.e., dust-free. From this information, we can estimate the attenuated stellar emission as a function of wavelength.

Therefore, the BEAST gives us all relevant information about a single star (e.g. T_{eff} , $\log(g)$, Z_* , etc.), including fully characterized posterior probability distribution functions (PDFs) for the parameters, letting us accurately characterize the uncertainties. For the purpose of this work, the strong leverage of this technique comes from the fact that BEAST can predict the entire spectrum of the stars even in the bands that were not observed. This allows us to reconstruct the complete stellar UV input that will go into the ISM.

4.4 THE SPATIALLY UNRESOLVED DATA

We also make use of several other data products from PHAT and integrated photometry from other surveys to assess the contribution of stars we cannot spatially resolve to the ISRF. We use the (Johnson et al. 2012) cluster catalog, which provides the properties

²Note that a stellar SED can be identified by only 3 of the listed parameters, e.g. T_{eff} , $\log(g)$ and Z_* .

of stellar clusters in M31 (e.g. fluxes, locations and radii). It is necessary to include the cluster catalog in our assessment of the ISRF, because stars in clusters suffer from extreme crowdedness preventing us from performing individual stellar photometry, everywhere but in the outskirts of the cluster. We also present a procedure for generating synthetic catalogs from star formation histories (SFHs), which we use to analyze the unresolved stellar contribution. The latter give us an estimate of the incompleteness of the resolved stellar catalog. Finally, we introduce photometric data that we use to estimate incompleteness of the stellar catalogs, and to derive dust properties maps.

4.4.1 CLUSTERS AND CITIZEN SCIENCE

As mentioned above, the crowdedness of stellar clusters makes it difficult or impossible to resolve individual stars within a cluster’s radius. That is the reason why we incorporate the integrated photometry of clusters in our analysis, to account for the flux from these unresolved sources. The first cluster catalog in bricks 9, 15 and 21 was generated by “by-eye” identification (Johnson et al. 2012). To increase the sample and statistics, “the Andromeda Project” was created³. In this project citizen scientists helped to identify clusters (2753), foreground stars and background galaxies (2270). Johnson et al. (2015) measured integrated photometry of these identified clusters in PHAT filter passbands. The cluster catalog is 50% complete down to $\sim 500 M_{\odot}$ for ages < 100 Myr⁴.

For the integrated flux purposes we are interested in, cluster positions and radii are sufficient information. All stars, even if they are resolved, that lay within the cluster radius, are treated as cluster members and are removed from the BEAST catalogs (see Section 4.5.4 for details).

TABLE 4.2: *Fraction of flux enclosed in clusters compared to the resolved stellar catalogs in PHAT bricks*

	B 9 [%]	B 15 [%]	B 21 [%]
F275W	4.80	2.95	7.98
F336W	4.51	2.96	4.29

To quantify the contribution from the stars in crowded regions, we calculate the fractions of flux enclosed in clusters compared to the resolved stellar catalogs in the three PHAT bricks. The unresolved UV flux generated in clusters is small (few percent; see Table 4.2) compared to the flux generated by resolved stars, but not negligible.

³www.andromedaproject.com

⁴This varies with the position in the galaxy

4.4.2 SFH CATALOGS

Stars that are below the completeness limit (are too faint and/or too crowded to be resolved; see Section 4.3.1.1), contribute to the diffuse radiation field. Some part of this diffuse light is scattered light (from all types of stars, including bright ones), the other part comes from these faint (unresolved) stars. We need to estimate the contribution of the unresolved stars to the diffuse FUV field, to assess the importance of the FUV energy input from unresolved sources, that we cannot directly include in our method.

To analyze the unresolved stellar contribution, we use spatially resolved synthetic catalogs generated from the star formation histories (SFHs) of Lewis et al. (2015). The SFHs are derived for 500×500 pc regions using the Color-Magnitude Diagram (CMD) based analysis routine MATCH (Dolphin 2002). The MATCH routine takes a user-defined initial mass function (IMF) and binary fraction (fixed to 0.35 in this work) as well as reasonable ranges in age and metallicity. Distance and foreground extinction can be set or searched over a given range as well. Based on the optical and infrared PHAT photometry, the routine then computes many synthetic CMDs spanning the age and metallicity range. These individual CMDs are linearly combined and convolved with photometric errors and completeness as modeled by artificial star tests to form the best-fit composite CMD. The weights on each CMD are used to determine the maximum likelihood statistic based on a Poisson distribution, which is used to determine the best-fit solution. For a full description see Lewis et al. (2015).

The routine also includes a new dust model (see Appendix B in Lewis et al. 2015), which allows the user to more accurately describe the internal extinction in a galaxy. This is especially important working in the dustier fields of M 31. The dust is modeled as two distributions. The first, as mentioned above, describes the foreground extinction using a delta function with some width. The second is a log-normal distribution which models the extinction in the disk of the galaxy. Varying the parameters of the lognormal component gives the user the ability to account for the non-trivial amounts of differential extinction seen in each field.

We use the FAKE routine (which is part of the MATCH package) to calculate synthetic CMDs (a synthetic FAKE catalog) based on SFHs. Then the FAKE routine returns SEDs of the FAKE source catalog in the passbands of interest for this thesis work: PHAT, *Galex* FUV and NUV, *SDSS ugriz*, *2MASS JHK* and *IRAC*. We use the PHAT completeness limits based on artificial stellar tests, and we select all the sources below and above the completeness limit, that creates the FAKE faint and bright source catalogs. We add fluxes of all of the stars in the FAKE faint catalog to estimate the unresolved stellar population contribution (see Section 4.5.4 for details).

4.4.3 INTEGRATED PHOTOMETRY

4.4.3.1 GALEX

The far UV range is covered by *Galaxy Evolution Explorer (GALEX)* FUV (1350 – 1750 Å) and NUV (1750 – 2800 Å) bands. Far UV observations of M 31 (Thilker et al. 2005) have been obtained as part of the *GALEX* Nearby Galaxy Survey (NGS; Bianchi et al. 2003, 2005). Typical 1σ limits are 6.6×10^{19} and 2.8×10^{19} erg s⁻¹ cm⁻² Å⁻¹ for FUV and NUV, respectively (in surface brightness these limits correspond to 28.0 (28.2) AB_{mag} arcsec⁻¹ in FUV (NUV)). The FWHMs is 4.0'' for FUV, and 5.6'' for NUV bands (pixel size of both bands is 1.4''), therefore these bands cannot be used for individual star photometry, but are vital for the integrated photometry of our regions of interest. We subtract constant sky values 0.000929 MJy sr⁻¹ (FUV), and 0.004712 MJy sr⁻¹ (NUV) derived by (Thilker et al. 2005).

4.4.3.2 SDSS

The Sloan Digital Sky Survey (SDSS; York et al. 2000) covered entirely the disk of M 31 in a contiguous strip using the 5 *ugriz* filters. As *SDSS* imaging is well-calibrated, and the strip large enough to estimate the sky background, this data is ideal for determining the integrated optical photometry of M 31. Here we use the *ugriz* mosaics of Tempel et al. (2011). Details of the reduction of the *SDSS* images and the important sky removal are described in Tempel et al. (2011) and Tempel et al. (in prep.). The units are nanomaggies per pixel (0.396''), where nanomaggie is a linear unit of flux density equal to 10⁻⁹ maggies. A star of brightness 1 nanomaggie has a magnitude of 22.5 in any band, or a flux density of 3.631×10^{-6} Jansky. The average point-spread function across the images is 1'', more than sufficient for our integrated photometry.

4.4.3.3 SPITZER

Near to mid-infrared observations of the entire disk M 31 were taken by *Spitzer* (Werner et al. 2004) with IRAC instrument (Fazio et al. 2004), with details of the observations and reduction process found in Barmby et al. (2006), and with the Multiband Imaging Photometer (MIPS; Rieke et al. 2004) by Gordon et al. (2006). We specifically use here the background subtracted images from Draine et al. (2014), that have been convolved to SPIRE 350 μm resolution using the kernels of Aniano et al. (2011). The full details of the convolution and background subtraction can be found in Draine et al. (2014).

A uniform background was subtracted from each image (2.40 MJy sr⁻¹(8 μm), -0.0043 MJy sr⁻¹(24 μm)), measured as the median surface brightness in regions on the edges of the map, away from the main body of M 31 (these values showed no clear gradient).

For the *Spitzer* bands we considered, the IRAC $8\ \mu\text{m}$ has a FWHM= $2''.0$ and the MIPS $24\ \mu\text{m}$ has a FWHM= $6''.5$.

4.4.3.4 HERSCHEL PACS AND SPIRE

M 31 was observed at far-infrared wavelengths (see Figure 4.3) by the *Herschel Space Observatory* (PI O. Krause) using the PACS 70, 100, 160 μm and SPIRE 250, 350, 500 μm photometric bands (Griffin et al. 2010, Spectral and Photometric Imaging Receiver). For details of the PACS and SPIRE observations and processing see Groves et al. (2012) or Draine et al. (2014).

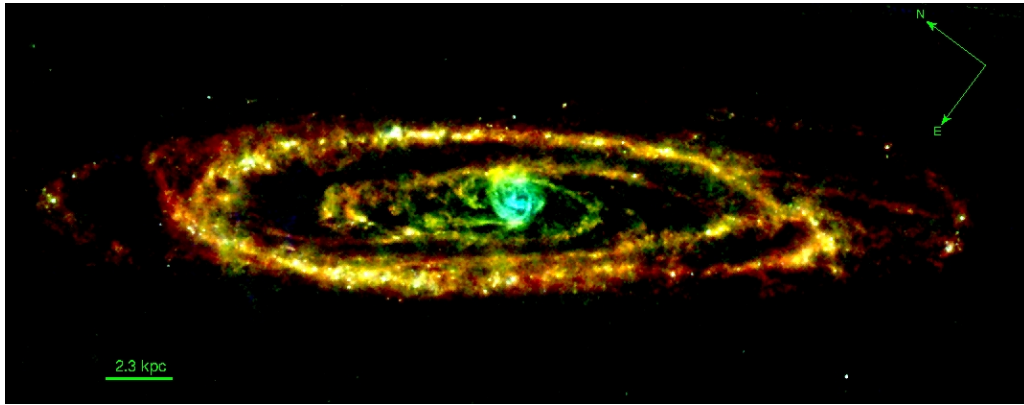


FIGURE 4.3: *Infrared 3-color image of M 31: PACS 70 (blue), PACS 100 (green) and SPIRE 250 (red).*

The final image size of all PACS and SPIRE images is $\sim 3^\circ \times 1^\circ$ aligned with the position angle of M 31's major axis. All images were reduced to level one using HIPE v6.0, and then SCANAMORPHOS v12.0 (Roussel 2012) was used to produce the final product. The FWHMs are $5''.6$ for 70 μm , $6''.8$ for PACS 100 μm , $11''.4$ for PACS 160 μm , $18''.2$ for SPIRE 250 μm , $24''.9$ for SPIRE 350 μm and $36''.3$ for SPIRE 500 μm . Beam sizes are taken from PACS Observer's Manual⁵ for $20''\text{s}^{-1}$ scans. $1''$ pixel size was used for all PACS bands, $6''$ for SPIRE 250 μm , $10''$ for SPIRE 350 μm and $14''$ for SPIRE 500 μm .

Similarly to *Spitzer* images, a uniform background was subtracted from each image: $3.17\ \text{MJy sr}^{-1}$ (70 μm), $3.23\ \text{MJy sr}^{-1}$ (100 μm) and $2.29\ \text{MJy sr}^{-1}$ (160 μm), $6.03\ \text{MJy sr}^{-1}$ (250 μm), $3.46\ \text{MJy sr}^{-1}$ (350 μm) and $1.66\ \text{MJy sr}^{-1}$ (500 μm).

⁵http://herschel.esac.esa.int/Docs/PACS/html/pacs_om.html

4.4.3.5 IR DATA PRODUCTS – DUST SED FITTING

The thermal emission from dust grains can be well approximated by a constant temperature (e.g. Ysard et al. 2012), under the assumption is that dust grains are in thermal equilibrium with the ISRF. We fit modified blackbody functions to the dust SED from $100 \mu\text{m}$ to $350 \mu\text{m}$ in each pixel (see example fits in Figure 4.4) of the images convolved to match $350 \mu\text{m}$ PSF, as a compromise between the signal-to-noise and the resolution. The spectrum can be approximated by modified blackbody, and the flux can be expressed as

$$F_\nu = \kappa_\nu \sigma_d B_\nu(T), \quad (4.1)$$

where σ_d is dust surface density and κ_ν is an opacity function

$$\kappa_\nu = \kappa_{350} \left(\frac{\nu}{\nu_{350}} \right)^\beta, \quad (4.2)$$

with opacity measured at $350 \mu\text{m}$ $\kappa_{350} = 1.92 \frac{\text{cm}^2}{\text{g}}$, and a fixed spectral index $\beta = 1.8$.

B_ν is the Planck function

$$B_\nu(T) = \frac{2h\nu^3}{c^2} \frac{1}{e^{h\nu/kT} - 1}. \quad (4.3)$$

Finally, we integrate the above equation to obtain the total infrared emission (TIR):

$$TIR = \kappa_{350} \int_8^{1000} \sigma_d B_\nu(T) \left(\frac{\nu}{\nu_{350}} \right)^\beta d\nu. \quad (4.4)$$

From the fit we determine dust temperature, surface density and total IR emission (Figure 4.5). Draine et al. (2014) and author of this work use the same IR data, therefore they provide the properties of the dust at the highest spatial resolution to date ($\sim 95 \text{ pc}$).

4.5 ANALYSIS & RESULTS

4.5.1 THE REGION SELECTION AND IMAGE PROCESSING

In this preliminary analysis, we concentrate on the SLIM fields, as the multi-wavelength coverage is the most thorough there (e.g., includes spectroscopic observations of the [C II], H α , and interferometric mapping of CO). We use the SLIM Fields 1, 3 and 5 (as

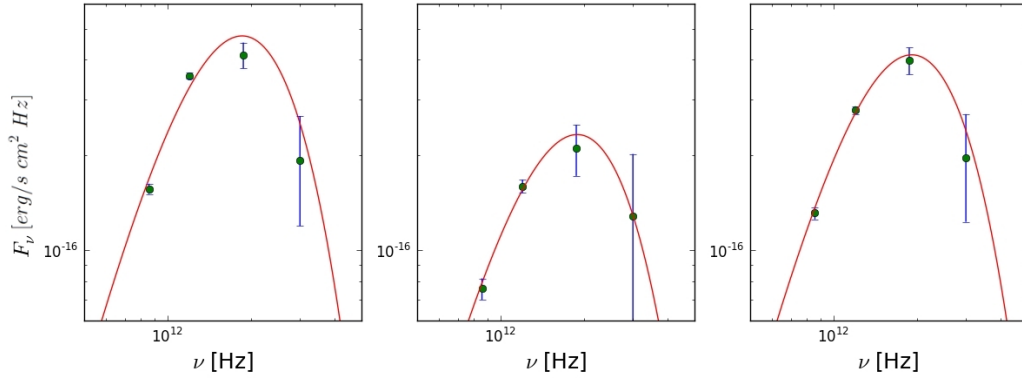


FIGURE 4.4: Three randomly drawn example IR modified blackbody fits from the map of M 31.

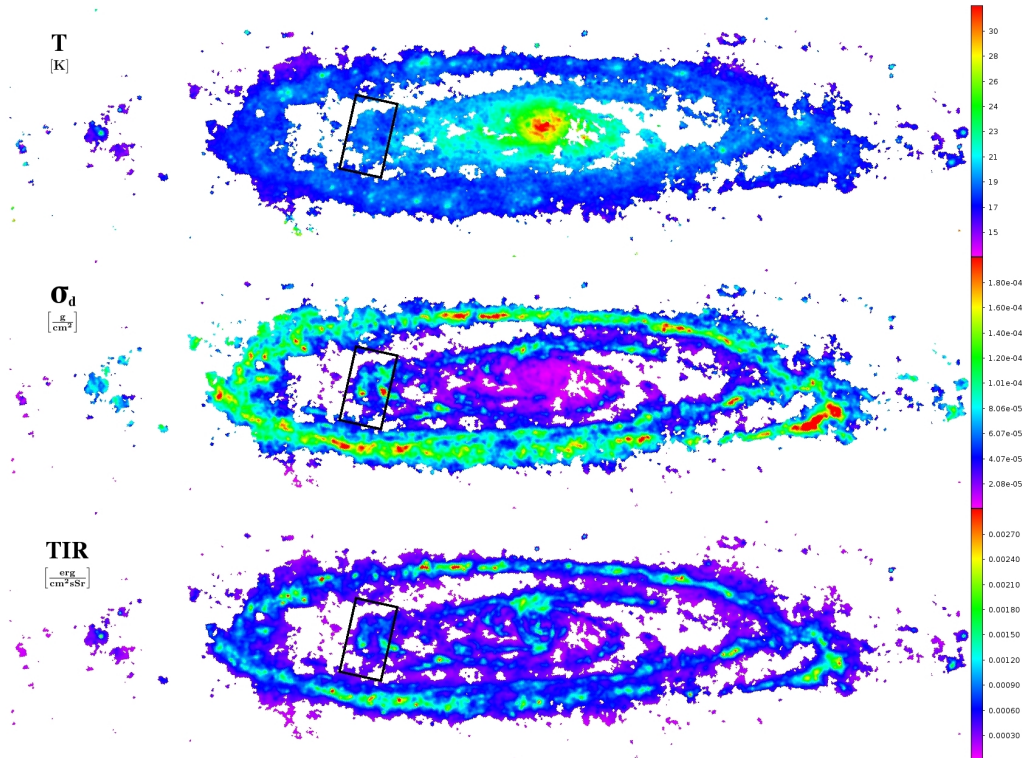


FIGURE 4.5: Properties of dust in M 31 from modified black body fitting. The top panel shows the temperature distribution in K. The middle panel presents the dust mass surface density in g cm^{-2} . The bottom one shows the total IR specific intensity in $\text{erg s}^{-1} \text{cm}^{-2} \text{sr}^{-1}$. Brick 9 from the PHAT survey (4 kpc^2 area) is highlighted by a black box.

only these regions overlap with the PHAT bricks where BEAST_v0 catalogs were created). We also use a small region in PHAT brick 21 (a subregion of SLIM field 1), as it the only brick in the preliminary SFH catalog, in the assessment of contributions of the unresolved

stellar populations. The central positions of the $3' \times 3'$ SLIM fields are listed in Table 2.2.

We convert the units in all images to Jansky, and we integrate the flux in each of these regions from the GALEX, SDSS, and IR mapping using the DS9 FUNTOOLS package functs⁶. The units of each original image are given in Section 4.3 and the conversion we use to put them on the same scale is in Appendix 4.A.

4.5.2 BEAST_v0 CATALOGS – MEASURING UV_{att}

We use the intrinsic properties of individual stars in M31 output from the BEAST_v0 processing (Section 4.3.2) to reconstruct the a map of stellar UV energy input, which can be used for spatial comparison with ISM dust and gas tracers. To determine the intrinsic and attenuated UV field of each selected regions, all stars lying inside the desired regions are selected from the catalogs. Using $\log T_{eff}$, $\log g$, A_V , R_V , the Castelli & Kurucz (2003) stellar library and Cardelli et al. (1989) extinction law, we construct the reddened and unreddened stellar spectrum. Then we sum the spectra of all the stars to create the reddened and intrinsic stellar spectra for each field (respectively red and blue in Figure 4.6 for SLIM field 3).

We define UV_{att} , the attenuated UV field, as the difference between the total intrinsic and reddened SEDs in the FUV energy bin, from 100 nm to 206 nm. The UV_{att} is the UV energy input of the stars within the selected region into the ISM. A map of the UV_{att} can be calculated by treating each pixel as a region. The grid of pixels comes from the image we intend to compare with the UV_{att} map (e.g., to match [C II] resolution in Figure 4.7).

4.5.3 STELLAR POPULATIONS CONTRIBUTING TO THE UV ISRF

The resolved stellar SED fit results from PHAT allow us to assess the contribution of individual stars to the intrinsic UV radiation field over a range of scales – a study that has only previously been possible in the solar neighborhood (e.g., Habing 1968).

In Figure 4.8 we illustrate the fractional contribution of various mass stars to the total UV_{att} in SLIM fields 1, 3 and 5. We select stars with $8M_{\odot} < M_{birth} < 20M_{\odot}$ as representative of B0–B3 stellar types, and $M_{birth} > 20M_{\odot}$ as O-stars.

From analysis of the SED fits to resolved stellar photometry, we find that the attenuated UV emission is generated predominantly by B-stars ($\sim 60\%$), while only $\sim 30\%$ is coming from O-stars (with lifetimes $\lesssim 10$ Myr). This demonstrates that on \sim kiloparsec scales in M31, massive B-stars dominate the UV field as in the solar neighborhood. The SLIM regions are the most active star-forming sites in M31, and even there B-stars make a large contribution to the ISRF. Interestingly, while in SLIM fields 3 and 5, the relative

⁶<http://hea-www.harvard.edu/RD/funtools/ds9.html>

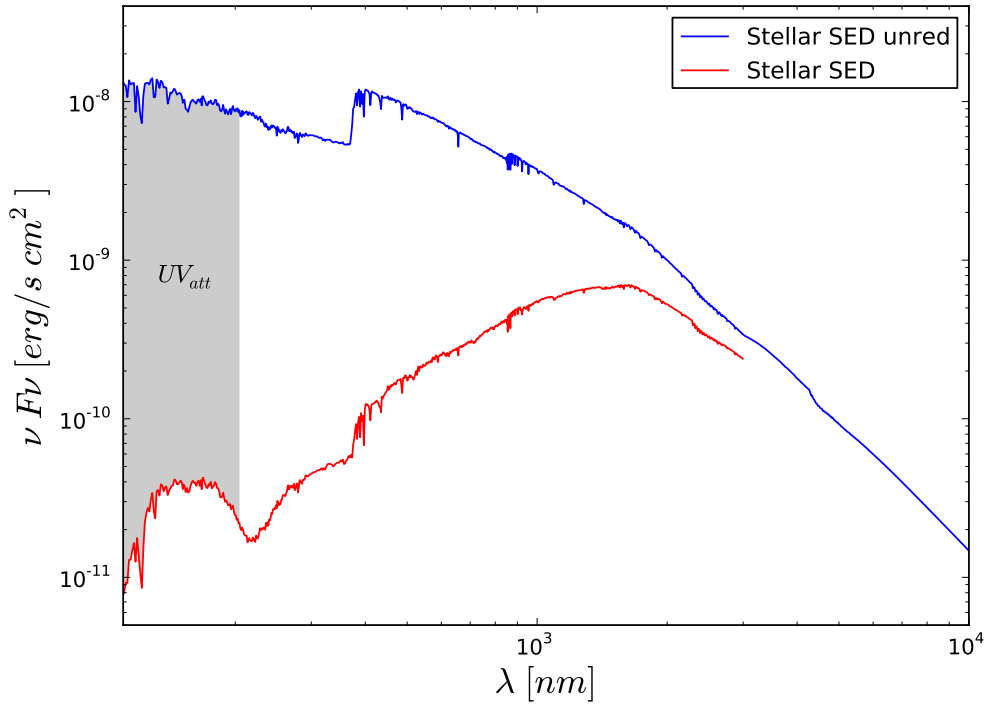


FIGURE 4.6: A plot showing the total SEDs created from the sum of individual stellar BEAST_v0 SEDs: the observed (reddened; red) and the intrinsic (unreddened; blue), in SLIM field 3. The shaded area shows our UV_{att} measurement of the FUV flux (100 – 206 nm) that is lost from the line of sight.

contributions of O & B-stars are similar, in the most distant field (SLIM field 1) the O-stars contribute measurably less UV to the total UV light.

4.5.4 COMPLETENESS AND OTHER ISSUES

In this section, we estimate what fraction of light is coming from:

- diffuse emission (scattered light)
- light from unresolved stars (estimated from simulated CMD with SFR; Lewis et al. 2015)
- resolved light from stars in stellar (BEAST_v0) and clusters in cluster catalogs

Integrated fluxes in the images give us the upper constraints on the total (resolved and unresolved stars, scattered light) that can appear in the region (note that we have re-

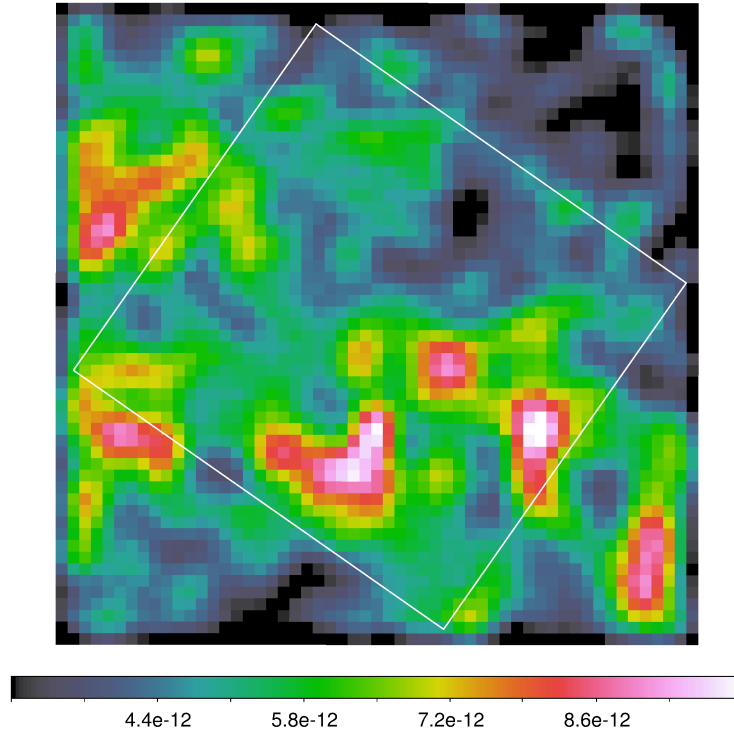


FIGURE 4.7: The preliminary resolved UV_{att} map in $\text{erg s}^{-1}\text{cm}^{-2}$ in SLIM field 3 (white box).

moved the background and foreground component from the *GALEX*, *SDSS* and *IRAC* images). By fitting resolved stars (BEAST_v0 catalog) and unresolved stars (fraction of SFH catalog), masking foreground and background, we can deduce what fraction of light is scattered. The straightforward way to proceed is to compare the integrated fluxes from the catalog and the images in the same physical region. We can illustrate all components that contribute to the total flux by a simple formula:

$$F_{tot} = F_{res} + F_{unres} + F_{cls} + F_{scatt}, \quad (4.5)$$

where F_{tot} – total integrated fluxes, F_{res} – BEAST_v0 catalog, F_{unres} – flux from unresolved stars from SFH catalog, F_{cls} – clusters and F_{scatt} – scattered light.

The procedure to address the completeness issue is to compare the integrated fluxes of the images, and catalogs: BEAST_v0, cluster, and SFH (Lewis et al. 2015), in the selected regions. To compare with integrated photometry of the images, we simply sum all reddened and unreddened fluxes in each accessible filter in the selected region. For BEAST_v0 catalogs the accessible filters are all PHAT filters, while for SFH catalogs – all FAKE output filters. To enable a direct comparison between the SEDs, we applied 50% completeness cuts on PHAT filters in SFH catalogs (see Section 4.4.2). The comparison

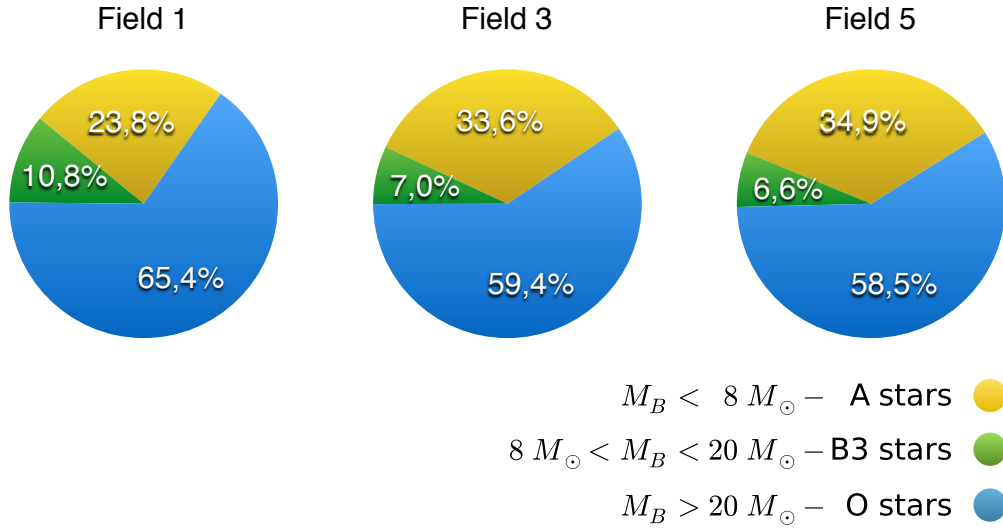


FIGURE 4.8: Pie charts showing the relative energy contribution to ISM from different stellar populations for SLIM fields 1, 3 and 5.

of all of these integrated fluxes is presented in Figure 4.10.

We also include the PHAT cluster catalog to obtain the total input UV energy. The cluster catalogs contain the position of the centers of clusters, their radius and fluxes in all 6 PHAT bands. We cannot simply add individual stellar and cluster fluxes in PHAT bands, because some of the stars from the BEAST_v0 catalog fall into these radii of clusters (see Figure 4.9). To avoid double counting their energy input, we select and reject these stars from BEAST_v0 catalog.

TABLE 4.3: Estimated fraction of the unresolved flux^a F_{unres} in the synthetic “red-denied” stellar catalog based on SFHs in all PHAT filters

	F275W	F336W	F475W	F814W	F110W	F160W
B 21 F 6	23.3%	56.7%	38.5%	30.6%	28.4%	22.6%

^a defined as the integrated flux of the stars below 50% completeness limit

As described in Section 4.4.2 synthetic FAKE stellar catalog represents all stars (below and above the completeness limit) in the given 500×500 pc region. To estimate the faint fraction of stars that should be detected (therefore included and fitted in the BEAST_v0 catalog) and the part that we miss, we apply 50% completeness limit derived from ASTs. Due to the time steps in the synthetic SFH and extinction issues, we do not expect the brightest part of SFH catalog, where there are small numbers of massive stars, to match BEAST_v0. Nevertheless, in the context of completeness of stellar catalogs, we are mostly interested in the old/low mass star contribution to the unresolved UV field. The old/low mass stars emit mostly in the longer wavelengths, where scattering should not be as

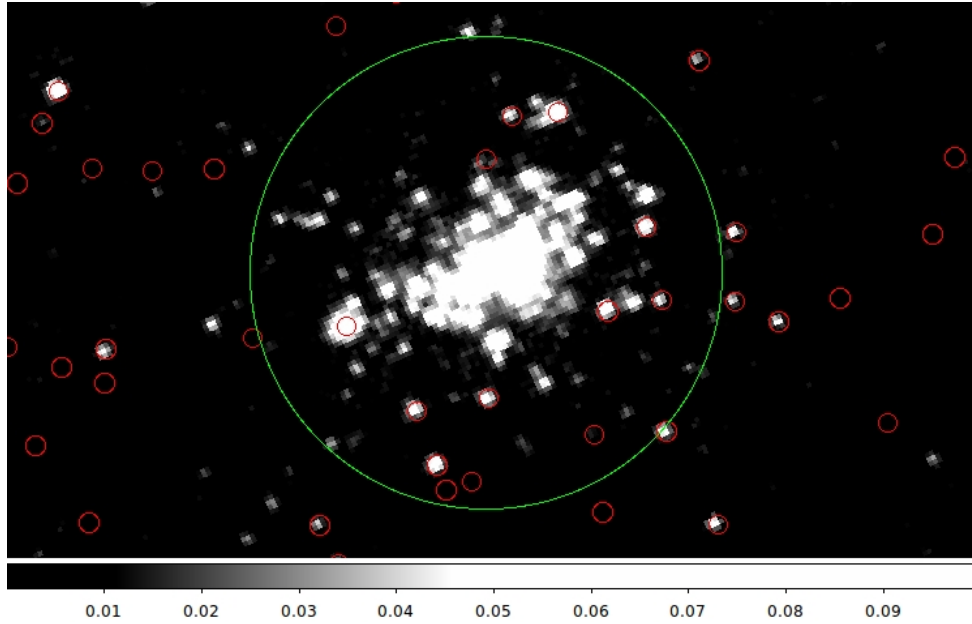


FIGURE 4.9: *Brick 9 field 11 of M 31. PHAT image in F336W band, cluster with its radius in green, stars from BEAST_v0 catalog in red showing they overlap.*

important, so our total flux from the stellar catalogs should match well with the image integrated photometry at near-IR and optical wavelengths. We give the estimated fractions of the unresolved flux in the synthetic “reddened” stellar catalog in all PHAT filters in Table 4.3.

Note, that due to known issues in the *HST* imagery (see Section 4.3.1.1), extracting photometry from large apertures (~ 500 pc) is very difficult if not impossible. Thus, we decided to use SDSS images instead for the large aperture integrated photometry.

4.5.4.1 ISSUES WITH THE EARLY VERSION OF BEAST

The BEAST_v0 catalog takes as an input a preliminary PHAT resolved photometric *gst* catalog (with applied S/N, crowdedness and sharpness cuts). The catalog was additionally trimmed to select stars with detections in at least 4 bands. BEAST_v0 treats non-detections as lack of information, while BEAST_v1 will use them as the upper limits to better constrain the SED fitting.

To double check the BEAST_v0 results for UV_{att} , we applied MAGPHYS SED fitting method (da Cunha et al. 2008) to the integrated stellar and dust photometry in PHAT brick 9 field 8. This method balances total energy emitted in the IR with the attenuated stellar energy to predict the intrinsic (unreddened) stellar spectrum. We compare this predicted MAGPHYS unreddened stellar spectrum with the co-added unreddened individual

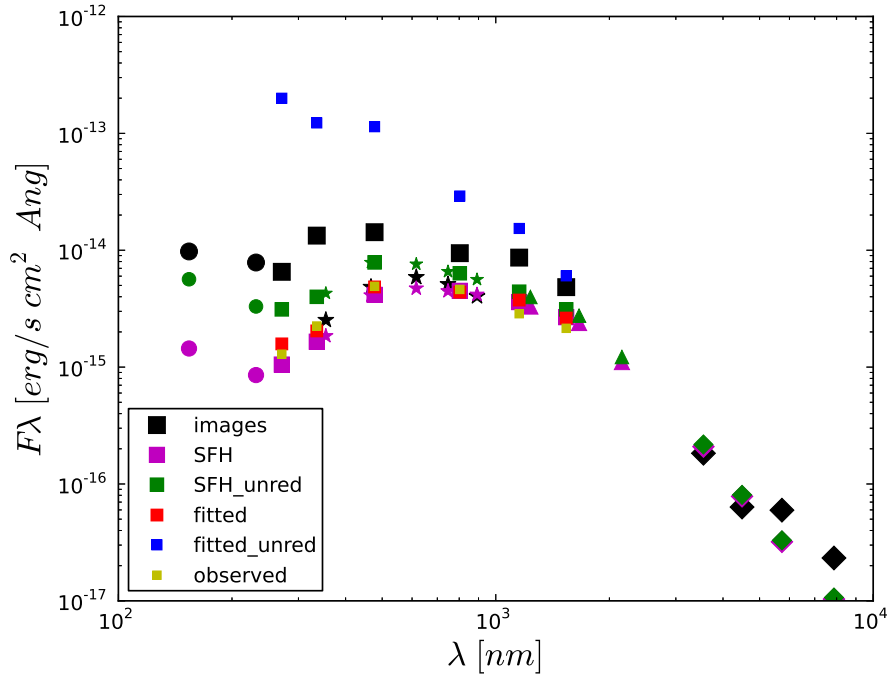


FIGURE 4.10: A plot showing integrated fluxes in brick 21 field 6 (subregion of SLIM field 1) in each filter. Circles indicate GALEX, squares – PHAT, stars – SDSS, triangles – 2MASS and diamonds – IRAC. Colors indicate source: images – original images, SFH/SFH_unred – SFH catalogs (50% completeness cuts applied to enable direct comparison with BEAST_v0 catalogs), fitted/fitted_unred – BEAST_v0 catalogs, obs – PHAT aperture photometry.

stellar BEAST_v0 spectra in Figure 4.11. This comparison suggests that the preliminary BEAST_v0 stellar catalogs might significantly overestimate attenuation of stars. The fraction of stars with $A_V > 5$ in brick 9 is 10%, in brick 15 is 12%, and in the outermost brick 21 it is 4%, while with $A_V > 8$ it is respectively 3%, 3% and 1%.

Another argument suggesting significant overestimate of the stellar attenuation is that the integrated intrinsic SED from resolved BEAST_v0 stellar catalog is much higher than the integrated intrinsic SED from the synthetic stellar catalog based on SFH (see Figure 4.10), where 50% completeness cuts have been applied to allow for direct comparison. Due to the discrepancy between unreddened SEDs from the BEAST_v0 and SFH catalog (with applied completeness cuts), the estimate of the intrinsic flux from unresolved stars (incompleteness of the BEAST_v0 catalog) is impossible. However, we were able to assess the fraction of the unresolved flux in the synthetic “reddened” stellar catalog (see Table 4.3).

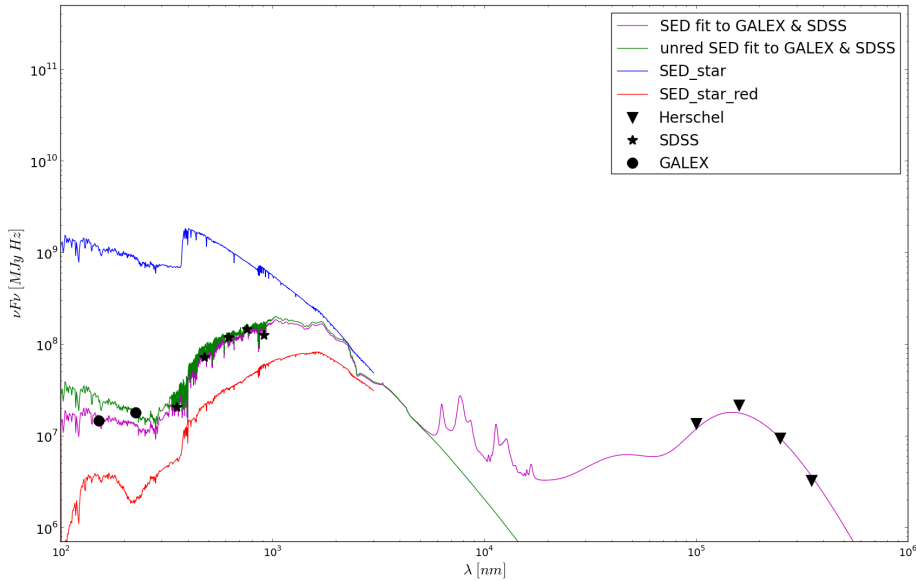


FIGURE 4.11: A comparison of resolved stellar SED fitting with integrated SED fitting to stellar and dust photometry using MAGPHYS (da Cunha et al. 2008), in PHAT brick 9 field 8.

4.5.5 EXTINCTION FROM STARS VERSUS DUST COLUMN

We can also compare the BEAST_v0 results with an independent upper limit on the dust column density (A_V) from infrared SED modeling (see IR map in Figure 4.3). Although this test is useful given the possible significant overestimate of the stellar attenuation mentioned in the previous Section, the two methods are not directly comparable. The stellar method to derive extinction is dependent upon the location of the star relative to the dust (we gain information only about the dust in front of the star), while from the other method we get the total dust along a line-of-sight. One can imagine that we measure photometry of two adjacent stars, but due to projection effects one star can be situated in front of the dusty disk, while the other star might sit behind the dust. The conclusions one would draw is that the A_V is changing dramatically between these two adjacent positions on the map, would be wrong. Worth noticing, is that each stellar derived extinction measurement is made at a line-of-sight, at very high resolution (PSF limited), while the IR maps are averaged over 95 pc.

The stellar number density from brick 9 in PHAT (Figure 4.12, top panel) generally traces the ring structure of M 31. Minima in this structure correspond to high A_V regions (Figure 4.12, middle), where faint stars are no longer detected. These faint stars contribute little to the total FUV and hence do not affect our further analysis.

There is a good correspondence between the A_V determined from stellar SED fitting and

the dust surface density. The young, massive stars tend to be associated with high A_V regions, as expected due to proximity to their birth clouds. This suggests that extinction measurements in the preliminary BEAST_v0 catalogs might be qualitatively correct, but even small number of over-extinguished very bright stars can cause to quantitatively overestimate the integrated/total intrinsic ISRF.

4.5.6 ISSUES WITH MEASURING ISRF ON DIFFERENT SPATIAL SCALES

There are several scale dependent issues with measuring the ISRF or UV_{att} . If we try to determine the ISRF on very small scales, such as a few parsecs, we may actually over resolve the ISRF, meaning that our integrated “local ISRF” misses out on the light from nearby stars that will contribute and maybe even dominate the local heating of dust and gas. To prevent this we need to make sure that the scales we probe are \geq the mean free path of the heating UV photons. In practice, this means for M 31 we should only look at ~ 100 pc scales. On the other hand, if we look at too large scales, we smooth over any variations in the local ISRF due to pockets of star-formation or dense dust clouds, and end up with a mean global determination of the ISRF.

4.5.7 COMPARISON OF UV_{att} AND TOTAL DUST EMISSION

To connect stellar UV energy input to dust heating, we examine the correlation between the total IR and attenuated UV on ~ 200 pc scales in Figure 4.13. There is a clear correlation between TIR and UV_{att} . Note that our UV_{att} represents only a fraction of the total absorbed UV, since we use only the near-UV HST bands in this plot and we measure the attenuated rather than absorbed UV flux.

Figure 4.13 shows that the relationship between TIR and UV_{att} has a super-linear slope on ~ 200 pc scales in both brick 9 and 15. Several effects may contribute to this steep relation: (1) in the brightest UV pixels, there is a higher fraction of young stars leading to a “bluer” UV field, which we do not account for in the above plot of UV_{att} ; (2) in regions where attenuation is lower, UV photons may escape from the 200 pc pixels. The visible shift between the points belonging to two bricks in Figure 4.13 suggests higher overall dust attenuation in brick 15 which is consistent with higher total dust mass surface density in the 10 kpc ring (see radial profile in Figure 3(a) in Draine et al. 2014).

We do not expect a one-to-one balance between UV_{att} and the total dust emission (Figure 4.13). UV_{att} reveals the dust absorption along the line of sight (and includes the scattering out of our sightline). The total dust emission however reveals the total amount of energy absorbed, meaning it is an isotropic measure. Given the high inclination of M 31, we would naively expect a higher value of UV_{att} to dust emission as we are biased to a more optically thick view (whereas viewing M 31 face on would reveal a more optical thin bias compared to the dust Jonsson et al. 2010). It might be yet another argument

suggesting overestimated extinction in BEAST_v0 catalogs.

4.6 OUTLOOK AND IMPROVEMENTS USING BEAST_v1

In the future work, we will use new BEAST_v1 stellar catalogs over the full PHAT coverage, which will significantly improve our results, and which should remove the overestimate of the intrinsic UV ISRF. The new BEAST_v1 stellar catalogs will be using improved simultaneous multi-band photometry meaning fainter stars will be included in the catalog down to $\sim F0$ spectral type, instead of A0. Not only new stellar PARSEC (Bressan et al. 2012) evolution models will be used, but the new BEAST technique itself will improve as well to fully account for crowding and updated dust modelling.

In Section 4.5.4, we showed an example of the application of SFH catalog to estimate the contribution from unresolved stellar populations to the ISRF. The recently published SFH catalog by Lewis et al. (2015) covers now entire PHAT footprint except for the bulge (bricks 1 and 3).

For the integrated fluxes we are interested in, cluster positions and radii are sufficient information, but for detailed SED analysis we will use the results of stochastic stellar populations fits to the cluster SEDs (Fouesneau et al. in prep.). The output from the stellar cluster modeling is a spectrum – like the output from the BEAST is a stellar spectrum. The stochasticity included in the cluster modeling takes into account the discrete sampling of the initial mass function (IMF), allowing massive stars even in a low mass cluster $\lesssim 10^4 M_\odot$ (e.g., Fouesneau et al. 2012). Continuous modelling would not let a low mass cluster include massive stars, while such clusters are observed. This method was successfully tested in M31, for details see Fouesneau & Lançon (2010) and Berman et al. (2012).

We intend to compare the results based on new BEAST_v1 catalogs, e.g. intrinsic ISRF maps with multiwavelength observations. In addition to the [C II] maps described in the previous Chapters, we have privileged access to new high resolution H I maps being created with the *Karl G. Jansky Very Large Array* (PI Leroy) and to new CO(1-0) maps created with *Combined Array for Research in Millimeter-wave Astronomy* (PI Schrubba). We will be able to analyze how the intrinsic UV ISRF sets the observed tracers of the ISM phases. The fine resolution $\sim 20\text{--}40$ pc will enable us to perform that experiment.

We will be able to measure on which scales the energy is deposited. The experiment is to change the scales from large to small (e.g. pixel sizes from 700 pc to 100 pc), and to find at which scales the $UV_{att} - TIR$ relation stops steepening.

We will compare UV_{att} maps with all accessible tracers of SFRs (see an example in Figure 4.14). We will re-assess [C II], and H α plus $24 \mu\text{m}$ as SFR tracers (in analogous way as we did with TIR), based on the improved information about direct, resolved star-formation from the BEAST_v1. We can go even step further and compare stellar

energy input in the ionizing wavelength range (< 100 nm) with $H\alpha$ emission corrected for extinction (Choi et al. in prep.).

4.7 CONCLUSIONS

We have presented a methodology to determine the UV interstellar radiation field using preliminary BEAST_v0 results based on PHAT *HST* photometry.

Preliminary results based on the BEAST_v0 SED fits to the resolved stellar photometry suggest that the attenuated UV emission is generated predominantly by B0–B3 type stars ($\sim 60\%$), and only approximately 30% is coming from O-stars (with lifetimes shorter than 10 Myr). The significance of this result is that B-stars are responsible for majority of the heating of the ISM, even in the regions of M 31 with the highest Σ_{SFR} . This means that in M 31 SFR tracers such as dust emission or [C II] trace mostly stars $\sim 10^8$ yr old, not only recent massive star-formation.

From a comparison to the new *Herschel* infrared observations with the preliminary UV_{att} maps based on the BEAST_v0, we find (1) a strong correlation between the stellar attenuation and dust surface density, (2) the attenuated NUV light correlates well with total dust (re)emission in the IR.

4.A PHOTOMETRIC SYSTEMS

Each instrument installed on telescope and each filter has its own unique response function. The filter transmission is a wavelength dependent function describing sensitivity to incident radiation (see *HST* filters used by PHAT in Figure 4.1, top panel). It depends on the optical system, detectors and filters used.

Commonly used photometric systems (Phillips 2008) are:

- AB_{mag} – Absolute magnitude system defines the colors of a source of constant frequency flux density, F_ν to be zero. Zero magnitude in this system corresponds to the flux density of Vega at the λ_{eff} of the Johnson V band (~ 5500 Å).

$$AB_{mag}(\nu) = -2.5 \log_{10} F_\nu - 48.60 \quad (4.6)$$

- ST_{mag} – magnitude system is defined in an analogue way to AB, except colors are zero for a source of constant wavelength flux density, F_λ . Zero magnitude in this system corresponds to the flux density of Vega at the λ_{eff} of the Johnson V band (~ 5500 Å).

$$ST_{mag}(\lambda) = -2.5 \log_{10} F_\lambda - 21.1 \quad (4.7)$$

- $VEGA_{mag}$ – a historical visible photometric system, where zero point is to set the colors of the A0 V star Vega to be zero, e.g. it has the same magnitude in all bands. In the Johnson system Vega has a magnitude of 0.03 in all bands.

To convert between two magnitude systems, one need to know conversion constants for each filter. The conversion constant $conv$ from Vega to AB magnitude system for some commonly used filters are given in Table 4.4.

$$m_{AB} = m_{Vega} + conv$$

TABLE 4.4: Conversion from Vega to AB magnitude system.

Filter	$\lambda_{eff}[\text{\AA}]$	$conv$	Source
HST F275W	2710.2	1.50	HST tables ^a
HST F336W	3354.8	1.18	HST tables
HST F475W	4773.7	-0.10	HST tables
HST F814W	8029.5	0.42	HST tables
HST F110W	11534	0.76	HST tables
HST F160W	15369	1.25	HST tables
GALEX FUV	1538.6	2.223	Bianchi (2011)
GALEX NUV	2315.7	1.699	Bianchi (2011)
SDSS u	3546	0.944	Hewett et al. (2006)
SDSS g	4670	-0.116	Hewett et al. (2006)
SDSS r	6156	0.131	Hewett et al. (2006)
SDSS i	7471	0.354	Hewett et al. (2006)
SDSS z	8918	0.524	Hewett et al. (2006)
2MASS J	12350	0.89	Cohen et al. (2003)
2MASS H	16620	1.37	Cohen et al. (2003)
2MASS K	21590	1.84	Cohen et al. (2003)
IRAC 3.6	35500	2.78	IRAC Data HandBook 3.0 2006
IRAC 4.5	44930	3.26	IRAC Data HandBook 3.0 2006
IRAC 5.8	57310	3.75	IRAC Data HandBook 3.0 2006
IRAC 8	78720	4.38	IRAC Data HandBook 3.0 2006

^a www.stsci.edu/hst/wfc3/phot_zp_lbn

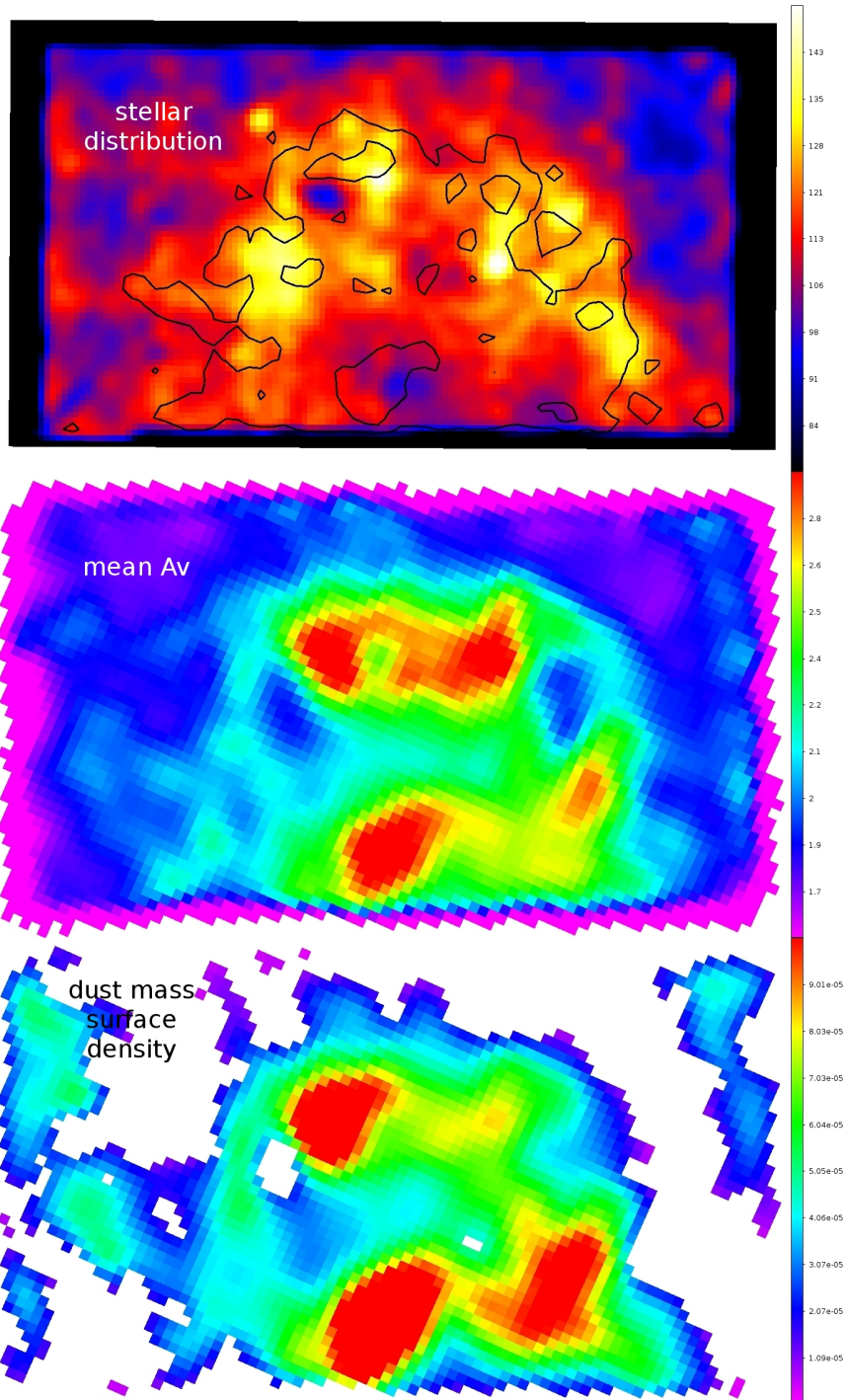


FIGURE 4.12: Stars and dust in PHAT's brick 9. The top panel presents the distribution of all stars from the PHAT catalog (in ~ 20 pc pixels) while contours show number density of B3 and earlier spectral type stars. Middle, the mean A_V from PHAT catalog in ~ 200 pc pixels. Bottom, dust mass surface density in ~ 200 pc pixels.

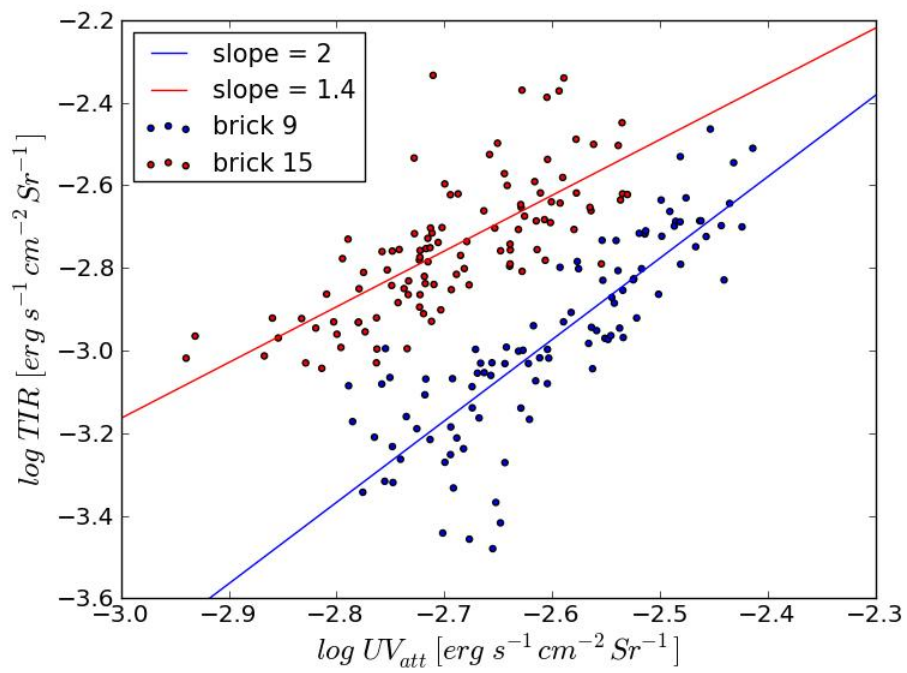


FIGURE 4.13: Scatter plot of the total IR vs attenuated UV (F275W and F336W) from all stars in brick 9 (blue) and 15 (red) in the PHAT catalogs in ~ 200 pc pixels. For both bricks the best-fit power-law is overlaid.

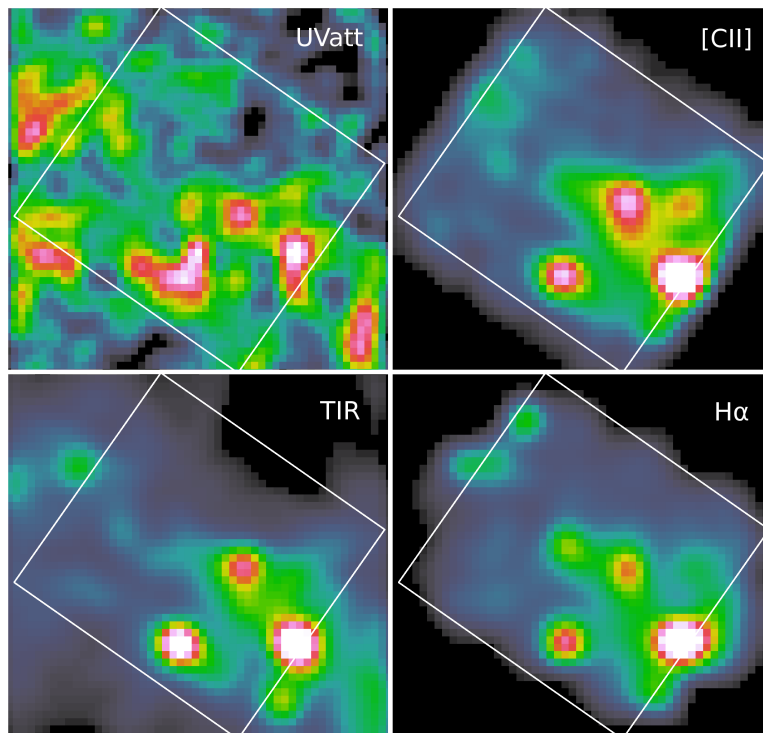


FIGURE 4.14: A comparison of preliminary UV_{att} maps with ISM tracers: Herschel $[C II]$, Herschel TIR and Calar Alto $H\alpha$ in SLIM field 3. All maps are convolved to match $[C II]$ resolution.

CHAPTER 5

SUMMARY

The energy balance of the ISM (the balance between heating and cooling processes) is a broad and multi-layered topic. It requires the determination of the chemical, thermal and density structure of the ISM. We do not yet comprehend the details of the physical processes that shape the ISRF and ISM phase distribution across galaxies, as they are linked and extremely complex. The energy balance controls the cycle of the ISM, and sets the structure of the ISM phases, which in turn control the processes of star-formation (SF). Therefore understanding the energy balance of the ISM is an essential step towards understanding the processes which shape evolution of galaxies across the cosmic time, and lead to the diversity of galaxy properties in the Universe.

In this thesis I pursued several open questions about these heating and cooling processes, which are key for understanding the energy balance of the ISM.

- What stellar populations are responsible for the heating of the ISM?
- From which phase does the dominant coolant [C II] arise?
- Is [C II] as a good SFR tracer?
- On what scales the energy is deposited?

Answering these questions help to understand what are the fractional contributions from different mechanisms and stellar populations to heating the ISM, and re-evaluate SFR tracers like [C II]. We investigated how much energy is available from stars in Chapter 4, how much energy is injected to the ISM in Chapter 3, and how the ISM cools in Chapter 2. We spatially separated star-forming and diffuse regions in Chapter 2. We showed that on ~ 700 pc scales [C II]-SFR relation seen on global scales has been recovered.

This work focuses on the energy balance in M31, an ideal laboratory to study the interstellar medium due to its proximity (allows for high spatial resolution), external perspective (avoids line-of-sight confusion), and as it is a representative of the large, star-forming, metal-rich galaxies where most of the star formation in the local Universe oc-

curs (Karim et al. 2011). We compiled a unique multi-wavelength set of data in M 31. In this work we presented the Survey of Lines in M 31 (SLIM) with contributing new Integral Field Spectroscopic *Herschel* PACS [C II] and Calar Alto PPAK H α data. These observations allowed us to study the dominant neutral gas coolant – [C II] on ~ 50 pc scales, and to use pure H α emission maps (without necessity to correct them for stellar and [N II] emission). We combine archival *ISO* [C II] measurements in the bulge of M 31 (Mochizuki 2000) with ancillary data to identify potential heating sources responsible for gas heating in the absence of young stars. For the first time in extragalactic studies, we directly constrain the ISRF intensity and spectral shape, based on ability to locate and model the spectral energy distributions (SEDs) and extinction of all of the bright stars in M 31 from the PHAT.

The key results from this thesis are:

- While the H α emission in M 31 is concentrated in the SFR regions, we find that a significant amount (~ 20 – 90%) of the [C II] emission comes from outside star-forming regions, and that the total IR (TIR) emission has the highest diffuse fraction of all SFR tracers.
- The differences in the relative diffuse fractions of [C II], H α and IR tracers are likely caused by a combination of energetic photon leakage from H II regions and heating by the diffuse radiation field arising from older (B-star) stellar populations. However, we find that by averaging our measurements over \sim kpc scales, these effects are minimized, and the relation between [C II] and SFR found in other nearby galaxy studies is retrieved. This suggests that $\lesssim 700$ pc scales energy is deposited. In the future we will try to constrain more accurately these scales by using intrinsic stellar radiation field and total dust emission.
- We find that the [C II] – SFR correlation holds even at the small scales (~ 50 pc), although the relation typically has a flatter slope than found at larger (\sim kpc) scales, where [C II] traces the SFR approximately linearly. This may be a result of the diffuse [C II] emission.
- We find a weak correlation of the [C II]/TIR to dust color in each Field, and find a large scale trend of increasing [C II]/TIR with galactocentric radius (decreasing metallicity). We attribute this [C II]/TIR variation mostly to a change in the TIR emission, rather than in the photoelectric efficiency. Given we find a constant correlation of [C II] and SFR (correlating with the FUV strength and thus more representative of the true PE efficiency) between our fields, we suggest that the variation in [C II]/TIR is due to a differing diffuse contribution to the TIR.
- The photoelectric heating mechanism seems as the largest contributor to gas heating (where FUV flux is generated by evolved stellar populations), however photoionization and cosmic rays heating mechanisms are likely to be responsible for the observed [C II] “excess” in the bulge.

- We showed that we can predict [C II] emission in the SLIM fields in the disk of M 31 based on the estimated from integrated SED fitting fraction of the stellar energy that contributes to gas heating ($\epsilon_{PE}^{UV} \times UV_{att}$) with a constant photoelectric heating efficiency ($\epsilon_{PE}^{UV} = 13.5\%$). We also found that the attenuated UV energy relative to the total attenuated energy (UV_{att}/TOT_{att}) correlates well with the [C II]/TIR ratio, suggesting that it is the soft photon heating of dust that is driving the variation in the [C II]/TIR ratio across this disk. This is in agreement with a previous result suggesting that TIR is varying much more strongly across the disk than [C II].
- In the bulge we observe an “excess” of the [C II] emission which can be explained by other mechanisms that contribute to the gas heating in addition to the PE heating that dominates in the disk. The fact that UV_{att}/TOT_{att} fails to predict the observed [C II]/TIR ratio in the bulge can be consistently explained by additional to PE heating mechanisms powering [C II].
- We propose that a better method to approximate the PE heating efficiency (than $\epsilon_{PE}^{dust} = [CII]/TIR$) is to use a SED fitting technique to derive a more precise estimate of the energy absorbed by dust in the PE heating wavelength range (UV_{att}), that together with the [C II] emission allows us to determine the “true” photoelectric efficiency $\epsilon_{PE}^{UV} = [CII]/UV_{att}$.
- Preliminary results based on the SED fits to the resolved stellar photometry suggest that the attenuated UV emission is generated predominantly by B0–B3 type stars ($\sim 60\%$), and only approximately 30% is coming from O-stars (with lifetimes shorter than 10 Myr). This means that in M 31, SFR tracers that measure longer timescales, such as UV & [C II] might be dominated by heating generated by stars $\sim 10^8$ yr old, not only recent star-formation, which would lead to the overestimate of SFRs, depending on what timescale the SF tracer is supposed to track.
- We find a strong correlation between the stellar attenuation and dust surface density, and that the attenuated NUV light correlates well with total dust (re)emission in the IR.

5.1 OUTLOOK

The complexity of the energy balance of the ISM has been mentioned many times in this work. It should not be surprising then, that there are numerous aspects of the heating and cooling processes that we still do not understand.

Using all available data, we were able to establish a list of sources capable of powering [C II] emission in the bulge of M 31. However, the insufficient resolution and sparse coverage of the [C II] observations prohibited us from coming to more conclusive results. The new instrument FIFI-LS on-board SOFIA enables us to map efficiently [C II] emission line at the same resolution as *Herschel* PACS. We will use its capabilities in the

spatially resolved studies in order to get the answer what exactly is responsible for heating [C II], and what are the implications for our understanding of energy balance and for [C II] as a SFR tracer (see Section 5.1.1).

The other interesting aspect of energy balance is the influence of environment. Specifically, how the low metallicity affects the intrinsic interstellar radiation field and interstellar medium? We will explore this topic in Section 5.1.2.1.

5.1.1 SOFIA FIFI-LS OBSERVATIONS IN THE BULGE

In the SOFIA observing cycle 3 we successfully applied for 4.5 hr to follow-up of the work presented in Chapter 3. Our project aims to disentangle various scenarios for the origins of [C II] in the bulge of M31 known to be dominated by old stellar populations. We will exploit the high spatial resolution of FIFI-LS instrument to observe [C II] 158 μm and [O I] 63 μm emission lines.

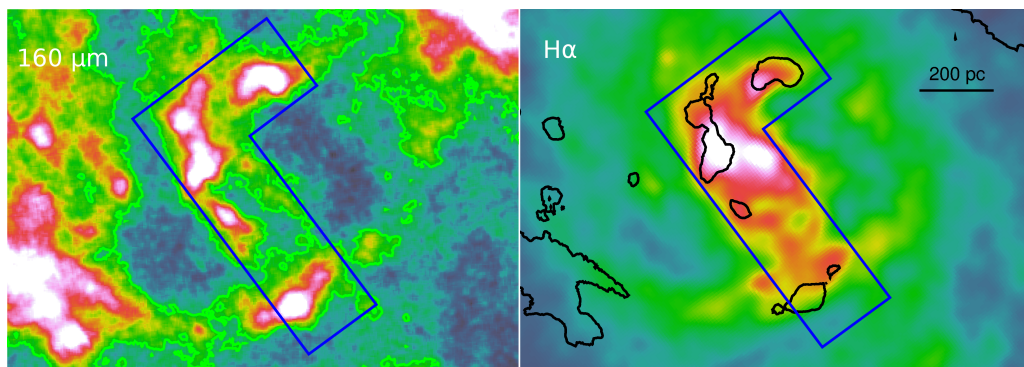


FIGURE 5.1: Zoom into the bulge of M31. Blue L-shape mark the proposed observations footprint in red channel. Green contours on PACS 160 μm map show our predicted $S/N > 4$ coverage. $H\alpha$ image is convolved to match PACS160 resolution to enable direct comparison. Black PACS160 peak emission contour overlaid on $H\alpha$ image to point out difference between them.

We will investigate spatial correlation of [C II] 158 μm line with dust (i.e. traced by PACS 100 μm – peak of the dust emission; tracing neutral phase) or $H\alpha$ (tracing ionized phase; Devereux et al. 1994) emission. Dust and $H\alpha$ emission show significantly different spatial distributions (Figure 5.1). Although we have only upper limits on H I (neutral gas) emission (Braun et al. 2009), based on CO (1-0) detections (Melchior et al. 2000) coinciding mostly with dust emission, we expect some H I to be present, between ionized and molecular emission. To take advantage of simultaneous observations in the blue channel, we will also map the [O I] 63 μm emission line. The [O I] line combined with the [C II] line will enable us to disentangle between emission from photo-dissociation regions (PDRs) or X-ray dominated regions (XDRs), based on Meijerink & Spaans (2005); Meijerink et al. (2007); Meijerink (2011) diagnostics.

5.1.2 UPGRADED BEAST STELLAR CATALOGS

5.1.2.1 APPLICATION OF OUR METHODOLOGY IN LOW-METALLICITY ENVIRONMENTS OF THE MAGELLANIC CLOUDS

The similarity of Galactic and M 31's ISRFs that we found in the course of these studies is not that unexpected (see Chapter 4). M 31 has SFR surface density comparable to the solar neighborhood, a gas-phase metallicity that is approximately solar, etc. To really understand the energy balance we need to move to different conditions to test our understanding of the processes. We will repeat our heating source analysis with a new *HST* observation program targeting the lower mass and metallicity environment of the Small Magellanic Cloud (SMC; PI Sandstrom; see Figure 5.2). The energy balance is likely to be different in the lower metallicity environment, because of the lower dust abundance, and therefore less efficient shielding of molecular clouds against stellar radiation field. In particular, this environment might lead to a smaller reservoir of the molecular gas that fuels star-formation, but also might lead to a higher fraction of CO-dark-H₂ gas.

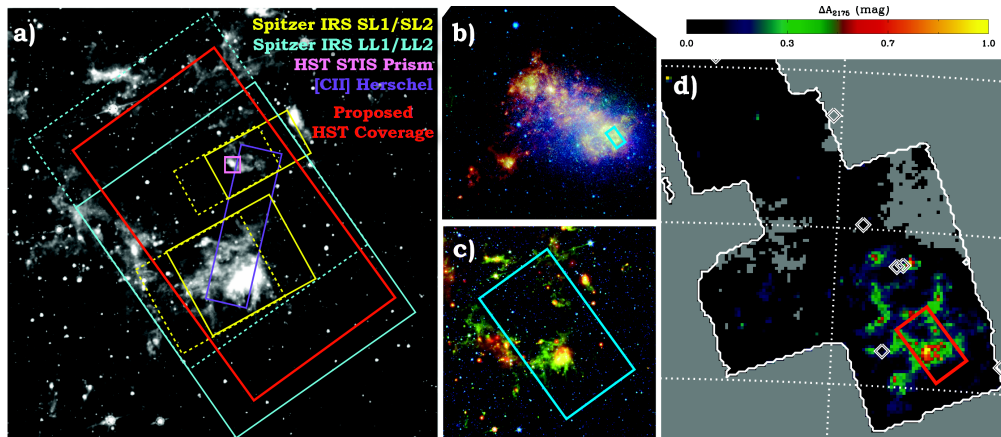


FIGURE 5.2: The *HST* coverage of our multi-band imaging (in red) overlaid on a) the $8\ \mu\text{m}$ map of the SMC from SAGE-SMC (Gordon et al. 2011) and S3MC (Bolatto et al. 2007), b) a three-color infrared image of the full SMC, c) a three color image (24 , 8 and $3.6\ \mu\text{m}$) focused on the SW Bar region and d) a map of the $2175\ \text{\AA}$ bump strength predicted from the abundance of PAHs (Sandstrom et al. 2010).

An even more extreme environment is the 30 Doradus nebula in the Large Magellanic Cloud (LMC), which hosts the most intense star formation in the local group (LG). Similar photometry to PHAT was obtained by the Hubble Tarantula Treasury Project (HTTP; PI Sabbi). 30 Doradus region will be mapped in the [C II] emission by the Stratospheric Terahertz Observatory (STO), a NASA balloon mission (PI Walker). We will use these observations to investigate energy balance in this starburst environment, using the same methodology as in M 31.

In the future, we would like to propose to obtain a complementary HST photometry to the ACS Nearby Galaxy Survey Treasury (ANGST) for dwarf galaxies that have maps of ISM tracers like [C II] from the Dwarf Galaxies Survey (DGS; PI Madden), i.e. in the UV bands that are needed for the energy balance study.

5.1.3 LONG-TERM PERSPECTIVES

Our studies on the well resolved heating-cooling balance in the ISM, together with new instruments built to characterize this multiphase ISM (e.g., SOFIA, STO), will create local benchmarks, linking the better understood Local Group to the unresolved galaxies that will be observed with James Webb Space Telescope (JWST; i.e. 3.3 μm PAH feature) and Atacama Large Millimeter/submillimeter Array (ALMA; i.e. [C II] emission) up to redshifts as high as ~ 8 . Results of my projects on heating and cooling tracers will help to understand galaxy evolution, will serve as a precursor for the future work on wider range of extreme environments in more diverse sample of galaxies, i.e. starbursts.

LIST OF FIGURES

1.1	Illustration of the cycle of energy and matter in the ISM	2
1.2	Average extinction curves of the SMC, LMC and MW	8
1.3	The efficiency of PE heating as a function of grain size and charge	9
1.4	A single transition Grotrian diagram of the C+ 158 μm	11
1.5	Excitation of the $^2P_{3/2}$ fine structure level of C+	12
1.6	A scheme of a photodissociation region	12
1.7	SFR to C+ relation in normal galaxies	13
1.8	The C+/FIR ratio “deficit”	14
1.9	SED of the ISRF in the Solar neighborhood	16
2.1	The SLIM survey coverage	26
2.2	The H α and C+ emission maps Fields 1–3	29
2.3	The H α and C+ emission maps Fields 4–5	30
2.4	PPAK IFS map and an example spectrum in Field 1	31
2.5	H α , C+, 24 μm and TIR emission from the SF region versus the total emission as a function of radius	36

2.6	$H\alpha$, C+, $24\mu\text{m}$ and TIR emission from the SF region vs. the total emission as a function of Σ_{SFR}	37
2.7	The relation between the C+ and SFR surface densities	40
2.8	C+/TIR surface brightness ratio versus dust color	44
2.9	C+/TIR surface brightness ratio versus the galactic radius	46
3.1	The overview of the ISO pointings and defined apertures used for the analysis	56
3.2	The SED of the central 1 kpc region of M 31	60
3.3	The intrinsic stellar spectrum of the entire disk of M 31, the illustration of attenuation effects on the intrinsic SED, the definition of UV_{att} and TOT_{att}	61
3.4	The average C+ and C+/TIR surface brightness ratio versus metallicity	62
3.5	Observed C+ emission in the SLIM fields versus predicted emission from UV_{att}	68
3.6	UV_{att}/TOT_{att} versus C+/TIR	69
3.7	UV_{att}/TOT_{att} versus galactocentric radius	73
3.8	The SED fits A1–A6	74
3.9	The SED fits A7–A12	75
3.10	The SED fits A13–A18	76
3.11	The SED fits A19–A24	77
3.12	The SED fits A25–A30	78
4.1	Transmission of the PHAT filters and SEDs of various stellar types	82
4.2	The PHAT survey coverage	84
4.3	Infrared 3-color image of M 31	90
4.4	Three randomly drawn example IR modified blackbody fits from the map of M 31.	92
4.5	Properties of dust in M 31: temperature, mass surface density and TIR	92
4.6	Integrated stellar SEDs in SLIM field 3	94

4.7	The preliminary resolved UV_{att} map in $\text{erg s}^{-1}\text{cm}^{-2}$ in SLIM field 3 (white box).	95
4.8	Pie charts showing the relative energy contribution to ISM from different stellar populations for SLIM fields 1, 3 and 5.	96
4.9	The overlap of the stellar and cluster catalogs	97
4.10	A comparison of the integrated fluxes from various methods in brick 21	98
4.11	A comparison of resolved stellar SED fitting with integrated SED fitting using MAGPHYS	99
4.12	Comparison of extinction maps derived from stars and dust	104
4.13	The relation between UV heating and dust cooling	105
4.14	A comparison of preliminary UV_{att} maps with SFR tracers: C+, TIR and $H\alpha$ in SLIM field 3.	106
5.1	SOFIA FIFI-LS coverage	110
5.2	<i>HST</i> , <i>Spitzer</i> and <i>Herschel</i> coverage in SMC	111

LIST OF TABLES

1.1	Phases of the interstellar gas	3
2.1	M 31 information	25
2.2	Coordinates of Field centers	26
2.3	The average [C II] emission, Σ_{SFR} and metallicity of the Fields	33
2.4	Ratios of fraction of emission of the ISM tracers coming from SF regions over total emission per field, for a H α contour $L_0 = 4.19 \times 10^{38} \text{ erg s}^{-1} \text{ kpc}^{-2}$ defining SF region	35
2.5	The average [C II] emission, Σ_{SFR} and metallicity of the Fields	41
3.1	ISO and Herschel measurements across the bulge of M 31	57
3.2	Contributions of the heating mechanisms to generate [C II] emission	67
4.1	PHAT photometric properties	84
4.2	Fraction of flux enclosed in clusters compared to the resolved stellar catalogs in PHAT bricks	87
4.3	Estimated fraction of the unresolved flux F_{unres} in the synthetic “reddened” stellar catalog based on SFHs in all PHAT filters	96
4.4	Conversion from Vega to AB magnitude system.	103

BIBLIOGRAPHY

- Abel, N. P. 2006, *MNRAS*, 368, 1949
- Aihara, H., et al. 2011, *ApJS*, 193, 29
- Alatalo, K., Appleton, P. N., & Lisenfeld, U. 2015, in *IAU Symposium*, Vol. 309, *IAU Symposium*, ed. B. L. Ziegler, F. Combes, H. Dannerbauer, & M. Verdugo, 178–181
- Aniano, G., Draine, B. T., Gordon, K. D., & Sandstrom, K. 2011, *PASP*, 123, 1218
- Astropy Collaboration, Robitaille, T. P., Tollerud, E. J., et al. 2013, *A&A*, 558, A33
- Azimlu, M., Marciniak, R., & Barmby, P. 2011, *AJ*, 142, 139
- Bakes, E. L. O., & Tielens, A. G. G. M. 1998, *ApJ*, 499, 258
- Barmby, P., Ashby, M. L. N., Bianchi, L., et al. 2006, *ApJ*, 650, L45
- Beerman, L. C., Johnson, L. C., Fouesneau, M., et al. 2012, *ApJ*, 760, 104
- Bennett, C. L., Fixsen, D. J., Hinshaw, G., et al. 1994, *ApJ*, 434, 587
- Bernard, J.-P., Reach, W. T., Paradis, D., et al. 2008, *AJ*, 136, 919
- Bernard, J.-P., Paradis, D., Marshall, D. J., et al. 2010, *A&A*, 518, L88
- Bianchi, L. 2011, *Ap&SS*, 335, 51
- Bianchi, L., Madore, B., Thilker, D., Gil de Paz, A., & GALEX Science Team. 2003, in *Bulletin of the American Astronomical Society*, Vol. 35, *American Astronomical Society Meeting Abstracts*, 1354
- Bianchi, L., Seibert, M., Zheng, W., et al. 2005, *ApJ*, 619, L27
- Bigiel, F., & Blitz, L. 2012, *ApJ*, 756, 183
- Bogdán, Á., & Gilfanov, M. 2008, *MNRAS*, 388, 56
- Bolatto, A. D., Wolfire, M., & Leroy, A. K. 2013, *ARA&A*, 51, 207
- Bolatto, A. D., Simon, J. D., Stanimirović, S., et al. 2007, *ApJ*, 655, 212
- Braine, J., Gratier, P., Kramer, C., et al. 2012, *A&A*, 544, A55
- Braun, R., Thilker, D. A., Walterbos, R. A. M., & Corbelli, E. 2009, *ApJ*, 695, 937
- Bressan, A., Marigo, P., Girardi, L., et al. 2012, *MNRAS*, 427, 127
- Brown, T. M., Ferguson, H. C., Stanford, S. A., & Deharveng, J.-M. 1998, *ApJ*, 504, 113
- Bruzual, G., & Charlot, S. 2003, *MNRAS*, 344, 1000
- Calzetti, D., Kennicutt, R. C., Engelbracht, C. W., et al. 2007, *ApJ*, 666, 870
- Cappellari, M., & Emsellem, E. 2004, *PASP*, 116, 138
- Cardelli, J. A., Clayton, G. C., & Mathis, J. S. 1989, in *IAU Symposium*, Vol. 135, *Interstellar Dust*, ed. L. J. Allamandola & A. G. G. M. Tielens, 5P

- Carilli, C., & Walter, F. 2013, ArXiv e-prints
- Castelli, F., & Kurucz, R. L. 2003, in IAU Symposium, Vol. 210, Modelling of Stellar Atmospheres, ed. N. Piskunov, W. W. Weiss, & D. F. Gray, 20P
- Chabrier, G. 2003, PASP, 115, 763
- Charlot, S., & Fall, S. M. 2000, ApJ, 539, 718
- Chary, R., & Elbaz, D. 2001, ApJ, 556, 562
- Ciardullo, R., Rubin, V. C., Ford, Jr., W. K., Jacoby, G. H., & Ford, H. C. 1988, AJ, 95, 438
- Clegg, P. E., Ade, P. A. R., Armand, C., et al. 1996, A&A, 315, L38
- Cohen, M., Wheaton, W. A., & Megeath, S. T. 2003, AJ, 126, 1090
- Cormier, D., Lebouteiller, V., Madden, S. C., et al. 2012, A&A, 548, A20
- Cormier, D., Madden, S. C., Lebouteiller, V., et al. 2015, ArXiv e-prints
- Croxall, K. V., K. in prep.
- Croxall, K. V., Smith, J. D., Wolfire, M. G., et al. 2012, ApJ, 747, 81
- da Cunha, E., Charlot, S., & Elbaz, D. 2008, MNRAS, 388, 1595
- Dalcanton, J. J., Williams, B. F., Lang, D., et al. 2012, ApJS, 200, 18
- Dale, D. A., & Helou, G. 2002, ApJ, 576, 159
- Dale, D. A., Gil de Paz, A., Gordon, K. D., et al. 2007, ApJ, 655, 863
- de Looze, I., Baes, M., Bendo, G. J., Cortese, L., & Fritz, J. 2011, MNRAS, 416, 2712
- De Looze, I., Cormier, D., Lebouteiller, V., et al. 2014, ArXiv e-prints
- Devereux, N. A., Price, R., Wells, L. A., & Duric, N. 1994, AJ, 108, 1667
- Díaz-Santos, T., Armus, L., Charmandaris, V., et al. 2013, ApJ, 774, 68
- Dolphin, A. E. 2002, MNRAS, 332, 91
- Dolphin, A. E., Saha, A., Claver, J., et al. 2002, AJ, 123, 3154
- Draine, B. T. 2011, Physics of the Interstellar and Intergalactic Medium
- Draine, B. T., & Li, A. 2007, ApJ, 657, 810
- Draine, B. T., Aniano, G., Krause, O., et al. 2014, ApJ, 780, 172
- Falcón-Barroso, J., Sánchez-Blázquez, P., Vazdekis, A., et al. 2011, A&A, 532, A95
- Fazio, G. G., Hora, J. L., Allen, L. E., et al. 2004, ApJS, 154, 10
- Fitzpatrick, E. L. 1999, PASP, 111, 63
- Fouesneau, M., & Lançon, A. 2010, A&A, 521, A22
- Fouesneau, M., Lançon, A., Chandar, R., & Whitmore, B. C. 2012, ApJ, 750, 60
- Galametz, M., Kennicutt, R. C., Calzetti, D., et al. 2013, MNRAS, 431, 1956
- Glover, S. C. O., & Clark, P. C. 2012, MNRAS, 426, 377
- Goldsmith, P. F., Langer, W. D., Pineda, J. L., & Velusamy, T. 2012, ApJS, 203, 13
- Gordon, K. D., Clayton, G. C., Misselt, K. A., Landolt, A. U., & Wolff, M. J. 2003, ApJ, 594, 279
- Gordon, K. D., PHAT, t., & Kapala, M. J. in prep.
- Gordon, K. D., Bailin, J., Engelbracht, C. W., et al. 2006, ApJ, 638, L87
- Gordon, K. D., Meixner, M., Meade, M. R., et al. 2011, AJ, 142, 102
- Graciá-Carpio, J., Sturm, E., Hailey-Dunsheath, S., et al. 2011, ApJ, 728, L7
- Graf, U. U., Simon, R., Stutzki, J., et al. 2012, A&A, 542, L16
- Griffin, M. J., Abergel, A., Abreu, A., et al. 2010, A&A, 518, L3
- Groves, B., Krause, O., Sandstrom, K., et al. 2012, MNRAS, 426, 892
- Groves, B. A., & Allen, M. G. 2010, 15, 614
- Habing, H. J. 1968, bain, 19, 421
- Helou, G., Khan, I. R., Malek, L., & Boehmer, L. 1988, ApJS, 68, 151
- Helou, G., Malhotra, S., Hollenbach, D. J., Dale, D. A., & Contursi, A. 2001, ApJ, 548, L73
- Herrera-Camus, R., Bolatto, A. D., Wolfire, M. G., et al. 2015, ApJ, 800, 1
- Hewett, P. C., Warren, S. J., Leggett, S. K., & Hodgkin, S. T. 2006, MNRAS, 367, 454

- Hirata, C. M. 2006, *MNRAS*, 367, 259
- Hollenbach, D. J., & Tielens, A. G. G. M. 1999, *Reviews of Modern Physics*, 71, 173
- Horne, K. 1986, *PASP*, 98, 609
- Israel, F. P., & Maloney, P. R. 2011, *A&A*, 531, A19
- Israel, F. P., Maloney, P. R., Geis, N., et al. 1996, *ApJ*, 465, 738
- Jacob, J. C., Katz, D. S., Berriman, G. B., et al. 2010, *Montage: An Astronomical Image Mosaicking Toolkit*, *astrophysics Source Code Library*
- Jenkins, E. B. 2009, *ApJ*, 700, 1299
- Johnson, L. C., Seth, A. C., Dalcanton, J. J., et al. 2012, *ApJ*, 752, 95
— 2015, *ApJ*, 802, 127
- Jonsson, P., Groves, B. A., & Cox, T. J. 2010, *MNRAS*, 403, 17
- Kapala, M. J., Sandstrom, K., Groves, B., et al. 2015, *ApJ*, 798, 24
- Karim, A., Schinnerer, E., Martínez-Sansigre, A., et al. 2011, *ApJ*, 730, 61
- Kaufman, M. J., Wolfire, M. G., Hollenbach, D. J., & Luhman, M. L. 1999, *ApJ*, 527, 795
- Kelz, A., Verheijen, M. A. W., Roth, M. M., et al. 2006, *PASP*, 118, 129
- Kennicutt, R. C., & Evans, N. J. 2012, *ARA&A*, 50, 531
- Kennicutt, R. C., Calzetti, D., Aniano, G., et al. 2011, *PASP*, 123, 1347
- Kennicutt, Jr., R. C. 1984, *ApJ*, 287, 116
- Kennicutt, Jr., R. C., & Hodge, P. W. 1986, *ApJ*, 306, 130
- Kessler, M. F., Steinz, J. A., Anderegg, M. E., et al. 1996, *A&A*, 315, L27
- Kim, S., & Reach, W. T. 2002, *ApJ*, 571, 288
- Kimura, H., Mann, I., & Jessberger, E. K. 2003, *ApJ*, 582, 846
- Kramer, C., Buchbender, C., Xilouris, E. M., et al. 2010, *A&A*, 518, L67
- Kramer, C., Abreu-Vicente, J., García-Burillo, S., et al. 2013, *A&A*, 553, A114
- Kreckel, K., Groves, B., Schinnerer, E., et al. 2013, *ApJ*, 771, 62
- Kroupa, P. 2001, *MNRAS*, 322, 231
- Langer, W. D., Pineda, J. L., & Velusamy, T. 2014a, *A&A*, 564, A101
- Langer, W. D., Velusamy, T., Pineda, J. L., et al. 2010, *A&A*, 521, L17
- Langer, W. D., Velusamy, T., Pineda, J. L., Willacy, K., & Goldsmith, P. F. 2014b, *A&A*, 561, A122
- Lanz, T., & Hubeny, I. 2003, *ApJS*, 146, 417
— 2007, *ApJS*, 169, 83
- Lebouteiller, V., Cormier, D., Madden, S. C., et al. 2012, *A&A*, 548, A91
- Leitherer, C., Leão, J. R. S., Heckman, T. M., et al. 2001, *ApJ*, 550, 724
- Leitherer, C., Schaerer, D., Goldader, J. D., et al. 1999, *ApJS*, 123, 3
- Leroy, A. K., Bigiel, F., de Blok, W. J. G., et al. 2012, *AJ*, 144, 3
- Leroy, A. K., Walter, F., Sandstrom, K., et al. 2013, *AJ*, 146, 19
- Levesque, E. M., Kewley, L. J., & Larson, K. L. 2010, *AJ*, 139, 712
- Lewis, A. R., Dolphin, A. E., Dalcanton, J. J., et al. 2015, *ArXiv e-prints*
- Luhman, M. L., Satyapal, S., Fischer, J., et al. 2003, *ApJ*, 594, 758
— 1998, *ApJ*, 504, L11
- Makiuti, S., Shibai, H., Nakagawa, T., et al. 2002, *A&A*, 382, 600
- Malhotra, S., Hollenbach, D., Helou, G., et al. 2000, *ApJ*, 543, 634
- Malhotra, S., Kaufman, M. J., Hollenbach, D., et al. 2001, *ApJ*, 561, 766
- Marigo, P., Girardi, L., Bressan, A., et al. 2008, *A&A*, 482, 883
- Mathis, J. S., Mezger, P. G., & Panagia, N. 1983, *A&A*, 128, 212
- Mathis, J. S., Ruml, W., & Nordsieck, K. H. 1977, *ApJ*, 217, 425
- McKee, C. F., & Williams, J. P. 1997, *ApJ*, 476, 144
- Meijerink, R. 2011, in *IAU Symposium*, Vol. 280, *IAU Symposium*, ed. J. Cernicharo &

- R. Bachiller, 177–186
- Meijerink, R., & Spaans, M. 2005, *A&A*, 436, 397
- Meijerink, R., Spaans, M., & Israel, F. P. 2007, *A&A*, 461, 793
- Meijerink, R., Spaans, M., Loenen, A. F., & van der Werf, P. P. 2011, *A&A*, 525, A119
- Meixner, M., Gordon, K. D., Indebetouw, R., et al. 2006, *AJ*, 132, 2268
- Melchior, A.-L., Viallefond, F., Guélin, M., & Neininger, N. 2000, *MNRAS*, 312, L29
- Mochizuki, K. 2000, *A&A*, 363, 1123
- . 2004, *Journal of Korean Astronomical Society*, 37, 193
- Mochizuki, K., Nakagawa, T., Doi, Y., et al. 1994, *ApJ*, 430, L37
- Mutch, S. J., Croton, D. J., & Poole, G. B. 2011, *ApJ*, 736, 84
- Nakagawa, T., Yui, Y. Y., Doi, Y., et al. 1998, *ApJS*, 115, 259
- Ögelman, H., Asaker, N., Anilin, S., et al. 2011, in *American Institute of Physics Conference Series*, Vol. 1379, *American Institute of Physics Conference Series*, ed. E. Göğüş, T. Belloni, & Ü. Ertan, 82–86
- Olsen, K. A. G., Blum, R. D., Stephens, A. W., et al. 2006, *AJ*, 132, 271
- Ott, S. 2010, in *Astronomical Society of the Pacific Conference Series*, Vol. 434, *Astronomical Data Analysis Software and Systems XIX*, ed. Y. Mizumoto, K.-I. Morita, & M. Ohishi, 139
- Parkin, T. J., Wilson, C. D., Schirm, M. R. P., et al. 2013, *ArXiv e-prints*
- Parravano, A., Hollenbach, D. J., & McKee, C. F. 2003, *ApJ*, 584, 797
- Pety, J., Schinnerer, E., Leroy, A. K., et al. 2013, *ApJ*, 779, 43
- Phillips, N. 2008, *Photometric Systems*, accessed: 2015-04-14
- Pilbratt, G. L., Riedinger, J. R., Passvogel, T., et al. 2010, *A&A*, 518, L1
- Pineda, J. L., Langer, W. D., Velusamy, T., & Goldsmith, P. F. 2013, *A&A*, 554, A103
- Poglitsch, A., Waelkens, C., Geis, N., et al. 2010, *A&A*, 518, L2
- Rieke, G. H., Young, E. T., Engelbracht, C. W., et al. 2004, *ApJS*, 154, 25
- Rodriguez-Fernandez, N. J., Braine, J., Brouillet, N., & Combes, F. 2006, *A&A*, 453, 77
- Rosenfield, P., Johnson, L. C., Girardi, L., et al. 2012, *ApJ*, 755, 131
- Roth, M. M., Kelz, A., Fechner, T., et al. 2005, *PASP*, 117, 620
- Roussel, H. 2012, in *SF2A-2012: Proceedings of the Annual meeting of the French Society of Astronomy and Astrophysics*, ed. S. Boissier, P. de Laverny, N. Nardetto, R. Samadi, D. Valls-Gabaud, & H. Wozniak, 559–563
- Rubin, D., Hony, S., Madden, S. C., et al. 2009, *A&A*, 494, 647
- Saglia, R. P., Fabricius, M., Bender, R., et al. 2010, *A&A*, 509, A61
- Salpeter, E. E. 1955, *ApJ*, 121, 161
- Sandin, C., Becker, T., Roth, M. M., et al. 2010, *A&A*, 515, A35
- Sandstrom, K. M., Bolatto, A. D., Draine, B. T., Bot, C., & Stanimirović, S. 2010, *ApJ*, 715, 701
- Sarzi, M., Falcón-Barroso, J., Davies, R. L., et al. 2006, *MNRAS*, 366, 1151
- Scalo, J. 1998, in *Astronomical Society of the Pacific Conference Series*, Vol. 142, *The Stellar Initial Mass Function (38th Herstonceux Conference)*, ed. G. Gilmore & D. Howell, 201
- Schultz, G. V., & Wiemer, W. 1975, *A&A*, 43, 133
- Simones, J. E., Weisz, D. R., Skillman, E. D., et al. 2014, *ApJ*, 788, 12
- Smith, J. D., K. in prep.
- Smith, R. J., Glover, S. C. O., Clark, P. C., Klessen, R. S., & Springel, V. 2014, *MNRAS*, 441, 1628
- Stacey, G. J., Geis, N., Genzel, R., et al. 1991, *ApJ*, 373, 423
- Stacey, G. J., Hailey-Dunsheath, S., Ferkinhoff, C., et al. 2010, *ApJ*, 724, 957
- Stanek, K. Z., & Garnavich, P. M. 1998, *ApJ*, 503, L131
- Telesco, C. 1999, in *Internet Resources for Professional Astronomy*, ed. M. R. Kidger, I. Perez-Fournon, & F. Sanchez, 131–160

- Tempel, E., Tamm, A., & Tenjes, P. 2010, *A&A*, 509, A91
- Tempel, E., Tuvikene, T., Tamm, A., & Tenjes, P. 2011, *A&A*, 526, A155
- Thilker, D. A., Hoopes, C. G., Bianchi, L., et al. 2005, *ApJ*, 619, L67
- Tielens, A. G. G. M. 2005, *The Physics and Chemistry of the Interstellar Medium*
- , 2008, *ARA&A*, 46, 289
- Tielens, A. G. G. M., & Hollenbach, D. 1985, *ApJ*, 291, 722
- Tremonti, C. A., Heckman, T. M., Kauffmann, G., et al. 2004, *ApJ*, 613, 898
- van Dokkum, P. G. 2001, *PASP*, 113, 1420
- Walter, F., Weiß, A., Riechers, D. A., et al. 2009, *ApJ*, 691, L1
- Walterbos, R. A. M., & Braun, R. 1994, *ApJ*, 431, 156
- Walterbos, R. A. M., & Kennicutt, Jr., R. C. 1987, *A&AS*, 69, 311
- Weisz, A. R., Rix, H.-W., & PHAT Team. in prep.
- Werner, M. W., Roellig, T. L., Low, F. J., et al. 2004, *ApJS*, 154, 1
- Williams, B. F., Lang, D., Dalcanton, J. J., et al. 2014, *ApJS*, 215, 9
- Wolfire, M. G., Hollenbach, D., & McKee, C. F. 2010, *ApJ*, 716, 1191
- Wolfire, M. G., Hollenbach, D., McKee, C. F., Tielens, A. G. G. M., & Bakes, E. L. O. 1995, *ApJ*, 443, 152
- Wolfire, M. G., McKee, C. F., Hollenbach, D., & Tielens, A. G. G. M. 2003, *ApJ*, 587, 278
- Worrall, D. M., Puschell, J. J., Jones, B., et al. 1982, *ApJ*, 261, 403
- Wright, E. L., Mather, J. C., Bennett, C. L., et al. 1991, *ApJ*, 381, 200
- Yan, R., & Blanton, M. R. 2013, in *IAU Symposium*, Vol. 295, *IAU Symposium*, ed. D. Thomas, A. Pasquali, & I. Ferreras, 328–331
- York, D. G., Adelman, J., Anderson, Jr., J. E., et al. 2000, *AJ*, 120, 1579
- Ysard, N., Juvela, M., Demyk, K., et al. 2012, *A&A*, 542, A21
- Zurita, A., & Bresolin, F. 2012, *MNRAS*, 427, 1463

